**ISTANBUL TECHNICAL UNIVERSITY ★ GRADUATE SCHOOL**

# RATIONAL DESIGN OF HYDRO- AND ORGANO-CRYOGELS

**Ph.D. THESIS**

**Berkant YETİŞKİN**

**Department of Chemistry**

**Chemistry Programme**

**OCTOBER 2021**

**ISTANBUL TECHNICAL UNIVERSITY ★ GRADUATE SCHOOL**

# RATIONAL DESIGN OF HYDRO- AND ORGANO-CRYOGELS

**Ph.D. THESIS**

**Berkant YETİŞKİN**
**(509152009)**

**Department of Chemistry**

**Chemistry Programme**

**Thesis Advisor: Prof. Dr. Oğuz OKAY**

**OCTOBER 2021**

**İSTANBUL TEKNİK ÜNİVERSİTESİ ★ LİSANSÜSTÜ EĞİTİM ENSTİTÜSÜ**

# HİDRO- VE ORGANO-KRİYOJELLERİN RASYONEL TASARIMI

**DOKTORA TEZİ**

**Berkant YETİŞKİN**
**(509152009)**

**Kimya Anabilim Dalı**

**Kimya Programı**

**Tez Danışmanı: Prof. Dr. Oğuz OKAY**

**EKİM 2021**

Berkant YETİŞKİN, a Ph.D. student of ITU Graduate School student ID 509152009, successfully defended the thesis entitled "RATIONAL DESIGN OF HYDRO- AND ORGANO-CRYOGELS", which he prepared after fulfilling the requirements specified in the associated legislations, before the jury whose signatures are below.

| | | |
|---|---|---|
| **Thesis Advisor :** | **Prof. Dr. Oğuz OKAY**<br>Istanbul Technical University | ..... |
| **Jury Members :** | **Prof. Dr. Nermin ORAKDÖĞEN**<br>Istanbul Technical University | ..... |
| | **Prof. Dr. Orhan GÜNEY**<br>Istanbul Technical University | ..... |
| | **Prof. Dr. H. Yıldırım ERBİL**<br>Gebze Technical University | ..... |
| | **Assoc. Prof. Dr. Deniz C. TUNCABOYLU**<br>Bezmialem Vakif University | ..... |

**Date of Submission : 27 August 2021**
**Date of Defense : 5 October 2021**

***To my dear family and to whom dedicated their lives to science,***

## FOREWORD

First and foremost, I want to thank my advisor Prof. Dr. Oğuz OKAY, to whom I worked with nearly 10 years with full motivation and enthusiasm like the first day. I will be always very grateful to him due to his great leadership and supporting attitudes and it will always be an honor for me to doing research with him. I would like special thank to Prof. Dr. Oya OKAY, who also had a great impact on this thesis as I also worked with her research group during my studies.

I would like to introduce my thanks to steering committee members, i.e. Prof. Dr. Nermin ORAKDÖĞEN and Prof. Dr. H. Yıldırım ERBİL, for their tolerance, helpful suggestions and assessments.

From my first day to my last, I met great people and researchers at ITU Polymeric Gels Research Laboratory (PGRL), who became not only my lab partners but also solid friends. Therefore, I want to thank to all PGRL researchers from past to present, but mostly to Dr. Ümit GÜLYÜZ, Dr. Aslıhan ARGUN, Dr. Burak TAVŞANLI, Özge AKÇA and Esra SU. Especially, I am very thankful to Çiğdem Buse ORAL, because of her great friendship, cheerfulness and cooperation that always motivates me. In addition, I also want to thank Dr. Atilla YILMAZ and Oktay Eren TÜREYEN, the members of ITU Ecotoxicology Laboratory, for their great collaborations.

Beyond any doubt, I am really grateful to my father Serhat Murat YETİŞKİN and my mother Nagihan YETİŞKİN for their endless love, caring, encouragement and support in every aspect of life.

Finally, I would also like to thank Istanbul Technical University Research Fund (ITU BAP) (Project No. TDK-2019-42484 and 39957) and The Scientific and Technological Research Council of Turkey (TUBITAK) (Project No. 114Z312, 117Y099 and 218M502) for financial and material support.

August 2021

Berkant YETİŞKİN
(M.Sc. Chemist)

**TABLE OF CONTENTS**

**Page**

## ABBREVIATIONS

**μ-CT** : Micro-computed tomography
**2D** : Two-dimensional
**3D** : Three-dimensional
**ATR-FTIR** : Attenuated total reflectance-Fourier transform infrared
**BDDE** : 1,4-butanediol diglycidyl ether
**DMSO** : Dimethyl sulfoxide
**DN** : Double network
**DSC** : Differantial scanning calorimetry
**ECM** : Extracellular matrix
**Fluo** : Fluoranthene
**IIR** : Butyl rubber
**MWCO** : Molecular weight cut-off
**Naph** : Naphthalene
**PAHs** : Polycyclic aromatic hydrocarbons
**PEG** : Poly(ethylene glycol)
**PDMS** : Polydimethylsiloxane
**Phen** : Phenanthrene
**PP** : Polypropylene
**PTFE** : Polytetrafluoroethylene
**PVA** : Poly(vinyl alcohol)
**Pyr** : Pyrene
**SEM** : Scanning electron microscope
**SF** : Silk fibroin
**SN** : Single network
**SPMD** : Semipermeable membrane device
**TEMED** : *N*,*N*,*N'*,*N'*-tetramethylethylenediamine
**TGA** : Thermal gravimetric analysis
**TN** : Triple network

## SYMBOLS

| | |
|---|---|
| $a$ & $b$ | : Second-order kinetic constants |
| $C_1$ | : Concentration of the first network |
| $C_2$ | : Concentration of the second network |
| $C_3$ | : Concentration of the third network |
| $C_0$ | : Concentration at time zero |
| $C_t$ | : Concentration at time *t* |
| $C_{eq}$ | : Concentration at equilibrium |
| $C_{SF}$ | : Silk fibroin concentration |
| $C_{IIR}$ | : Butyl rubber concentration |
| $D$ | : Pore diameter |
| $d_M$ | : Density of methanol |
| $d_1$ | : Density of toluene |
| $d_2$ | : Density of butyl rubber |
| $D_{dry}$ | : Diameter of dry gel |
| $D_{swl}$ | : Diameter of swollen gel |
| $E$ | : Young's Modulus |
| $E_{\parallel}$ | : Young's Modulus measured in parallel direction |
| $E_{\perp}$ | : Young's Modulus measured in perpendicular direction |
| $E_i$ | : Instantaneous Young's Modulus |
| $F$ | : Frictional force |
| $G'$ | : Elastic modulus |
| $G''$ | : Viscous modulus |
| $K$ | : Multiplying factor |
| $k$ | : Rate constant in first-order kinetic |
| $k'$ | : Rate constant in second-order kinetic |
| $l$ | : Layer spacing |
| $l_x$ | : Length of the gel in x-axis after swelling |
| $l_{x,0}$ | : Length of the gel in x-axis before swelling |
| $l_y$ | : Length of the gel in y-axis after swelling |
| $l_{y,0}$ | : Length of the gel in y-axis before swelling |
| $m_{swl}$ | : Weight of gels after equilibrium swelling in water |
| $m_{dry}$ | : Weight of gels in dry state |
| $m_o$ | : Weight of gels after preparation |
| $m_M$ | : Weight of gels swollen in methanol |
| $n$ | : Hill equation constant |
| $P$ | : Porosity |
| $R$ | : Immersion rate |
| $r$ | : Diameter of pipe |
| $s$ | : Solubility |
| $q_v$ | : Equilibrium volume swelling ratio |
| $q_{v,x}$ | : Equilibrium volume swelling ratio in x-axis |
| $q_{v,y}$ | : Equilibrium volume swelling ratio in y-axis |
| $\overline{q}_v$ | : Equilibrium volume swelling ratio in all directions |

$q_w$ : Equilibrium weight swelling ratio
$q_{w,1}$ : Equilibrium weight swelling ratio of single network gels
$q_{w,2}$ : Equilibrium weight swelling ratio of double network gels
$q_e$ : Absorbed PAH amount at equilibrium
$q_t$ : Absorbed PAH amount at time *t*
$t$ : time
$t_{1/2}$ : Half time
$\tan \delta$ : Loss factor
$U_{hys}$ : Hysteresis energy
$V_m$ : Molar volume
$V_p$ : Pore volume
$W$ : Frictional load
$w_{2/1}$ : Mass ratio of the second to the first network
$w_R$ : Mass ratio of the network components to the first single network
$W_g$ : Gel fraction
$\rho$ : Density of silk fibroin
$\delta$ : Solubility parameter
$\gamma_o$ : Strain amplitude
$\varepsilon$ : Strain
$\varepsilon_f$ : Fracture strain
$\lambda$ : Deformation ratio
$\varepsilon_{max}$ : Maximum strain
$\sigma_f$ : Fracture stress
$\sigma_{f,c}$ : Compressive fracture stress
$\sigma_{f,t}$ : Tensile fracture stress
$\sigma_p$ : Plateau stress
$\sigma_{nom}$ : Nominal stress
$\sigma_{comp}$ : Compressive stress
$\sigma_{true}$ : True stress
$\omega$ : Angular frequency

**LIST OF TABLES**

**Page**

**LIST OF FIGURES**

**Page**

## RATIONAL DESIGN OF HYDRO- AND ORGANO-CRYOGELS

## SUMMARY

Over billions of years of evolution, nature has selected soft materials, i.e. cells and tissues, as vital components for living beings. For instance, articular cartilage tissue in *Homo Sapiens* covers the bone ends and joints and it provides the actualization of basic movements such as bending of the arms and legs. This tissue can endure almost 1 million cycles per year, and it can be compressed up to a stress of 10 MPa without fraction. In addition, it possesses direction-dependent mechanical properties, i.e. anisotropy. However, these extraordinary mechanical properties of the tissues providing continuity in the lifespan of a living being can not be easily observed in man-made soft materials, i.e. hydrogels. In another word, hydrogels prepared by traditional methods are very brittle materials and some of them can not be endured to even one cycle, and break at Pa- or kPa-order stress values. Besides, their mechanical properties are not direction-dependent and they have isotropic mechanical properties.

After revealing nature's design principles in cells and tissues, i.e. when understand their chemical compositions and physical organizations, material scientists started to fabricate mechanically durable materials via mimicking nature. For instance, the mechanical stability of the articular cartilage arises from the extracellular matrix (ECM), which is composed of a structural protein called collagen creating a strong framework, and proteoglycans such as hyaluronan acting as energy dissipative fragments within ECM. Therefore, techniques developed for the preparation of high strength and toughness hydrogels have been mainly based on creating an efficient energy dissipation mechanism within the gel network. Cryogels, i.e. cryogenically synthesized macroporous polymer gel matrices, exhibit this energy dissipation mechanism via poroelasticity effect, due to their interconnected micron-sized pores. Moreover, cryogels possess extraordinary compressive strength up to MPa order as their gel walls originate from unfrozen liquid fractions where the concentrations of the reactants are much higher than that of their initial state. Another advantage of the cryogels is their convenience to orienting the pores as desired to create anisotropy.

Within the scope of this thesis, novel hydro- and organo-cryogels were prepared from aqueous and organic reaction solutions of specific polymers, respectively. Therefore, the thesis can be divided into two main parts associated with hydro- and organo-cryogels. The first part, i.e. hydro-cryogel part, is based on two publications, in which anisotropic silk fibroin (SF) cryogels possessing aligned pore morphologies were fabricated by using two different pathways. SF is a natural biopolymer derived from some spiders and silkworms. Due to its extraordinary properties such as biocompatibility, biodegradability and excellent mechanical toughness, it has become a very demanded biopolymer for biological applications. Therefore, SF was used in this thesis in order to fabricate hydro-cryogels. On the other hand, organic solutions of butyl rubber, i.e. synthetic isoprene-isobutylene rubber, were used to synthesize organo-cryogels as macroporous passive sampler sorbents.

In the first publication, anisotropic SF cryogels were obtained after directly immersing the reactors containing aqueous SF reaction solutions into liquid nitrogen at various immersion rates. The cryogel scaffolds exhibited a Young's modulus in the range of MPa and sustained up to 20 MPa compressive stresses. In addition to high mechanical strength, they also exhibited anisotropic microstructure and hence anisotropic mechanical properties, e.g., the Young's modulus ($E$) is 3.4 ± 0.5 MPa and 0.8 ± 0.3 MPa when measured along with the directions parallel and vertical to the freezing direction, respectively. In the second publication, we presented a different experimental set-up consisting of a copper bottom plate and a cylindrical polytetrafluoroethylene (PTFE) mold in order to fabricate anisotropic SF cryogels. The copper bottom plate was immersed in a cold bath at -30 or -196 °C, whereas the cylindrical PTFE mold locating outside of the cold bath was filled with aqueous solutions of SF of various concentrations. Unidirectionally frozen SF solutions were then subjected to cryogelation at -18 °C. Finally, we obtained mechanically strong SF scaffolds exhibiting microstructural, swelling and mechanical anisotropies. The scaffolds exhibited the highest modulus anisotropy of 21 ± 5 so far reported to our knowledge, i.e., Young's moduli $E$ = 2.3 ± 0.5 and 0.11 ± 0.03 MPa measured along parallel and perpendicular to the freezing direction, respectively. We also demonstrated that, independent on the fibroin concentration or direction of the measurements, 60% of the mechanical energy given to the cryogels are dissipated due to the friction between the fibroin pore walls, which is responsible for their squeezability and self-recoverability.

In the organo-cryogel part, butyl rubber (IIR) based organo-cryogels as a macroporous passive sampler were fabricated. After obtaining a primer IIR cryogel, i.e. single network (SN) cryogel, double (DN) and triple network (TN) cryogels were also prepared via successive cryogelations that were conducted within the pores of the previous cryogel. These multiple network based-cryogelation technique provided fabrication of IIR cryogels with tunable mechanical properties and pore distributions. For instance, they can be stretched up to 400%, and compressed at least 10-times without any significant mechanical deficiency as compared to the initial state. It was also shown that these IIR-based organo-cryogels can be used as an efficient passive sampler for polycyclic aromatic hydrocarbons (PAHs), whose sampling abilities mainly depend on their pore size distribution. For instance, SN rubber sorbent absorbed most rapidly PAHs which is attributed to its largest porosity and pore volume. On the other hand, TN sorbent had the highest sorption capacity because of its smaller pores and low porosity, preventing the escape of PAHs from the sorbent to the solution phase at longer time scales.

SF-based hydro-cryogels and IIR-based organo-cryogels fabricated within the scope of the thesis are both novel macroporous materials with extraordinary properties. Due to tissue-like MPa-order mechanical properties and anisotropic architecture, SF cryogels are suitable for several biological applications, especially for tissue engineering. On the other hand, fatigue-resistant and stretchable IIR-based organo-cryogels with adjustable pore morphology can be used as a passive sampler sorbent for organic pollutants in environmental applications.

## HİDRO- VE ORGANO-KRİYOJELLERİN RASYONEL TASARIMI

## ÖZET

Hücre ve dokular, canlıların hayati öneme sahip bileşenleri olup, fizik perspektifinde belli bir mekanik ve viskoelastik özelliği olan jel benzeri yumuşak malzemelerdir. Milyarlarca yıldır süregelen evrimsel süreçte doğa, canlıları değişen çevreye en uygun şekilde seçip işlemesi ile canlılardaki hücre ve doku gibi yumuşak malzemeleri de şekillendirmiştir. Muazzam fiziksel ve mekanik özelliklere haiz olan dokular, canlıların yaşam süreleri içerisinde belli bir devamlılığın sağlanmasında kilit rol oynamaktadır. Örneğin insanların kemik uçlarında ve eklemlerinde bulunan kıkırdak doku, kemikler arası sürtünmeyi azaltarak kol ve bacakların istenilen şekilde bükülmesini ve sonuç olarak insanın hareket etmesini sağlamaktadır. İnsan yaşamında her sene yaklaşık 1 milyon döngüye maruz kalan kıkırdak doku, ayrıca 10 MPa'lık bir sıkıştırma gerilimine kadar da parçalanmadan dayanabilmektedir. Diğer yandan bu doku yaklaşık 1000 $J.m^{-2}$ gibi bir parçalanma tokluğuna da sahiptir. Geleneksel yöntemlerle üretilmiş hidrojel gibi sentetik yumuşak malzemeler ise doğanınkilerden oldukça düşük mekanik özelliklere sahip olup; bazıları tek bir tam döngü bile tamamlanmadan çok düşük toklukla Pa ya da kPa mertebesindeki bir gerilim altında parçalanmaktadır. Doğanın biyolojik sistemlerdeki jeller için tasarım prensiplerinin anlaşılması ile, yani hücre ve dokuları oluşturan bileşenlerin kimyasal yapısı ve düzenlenmesinin ortaya koyulması ile, malzeme bilimciler doğayı taklit ederek üstün mekanik özelliklere sahip malzemeler geliştirmeye başlamışlardır.

Kıkırdak dokunun yukarıda bahsedilen mekanik özelliklerine sahip olması, ekstrasellüler matriks (ECM) adı verilen ve çeşitli biyopolimerlerin en uygun şekilde düzenlenmesi ile oluşan bir yapıdan ileri gelmektedir. ECM'de kollajen proteini lizil oksidaz enzimi ile çapraz bağlanarak ECM'nin rijit ve yüksek elastikiyete sahip ana iskeletini oluşturmaktadır. Diğer yandan hyaluronan gibi proteoglikanlar ise ECM'nin viskoz karakterini arttırarak yapıda bir enerji dağılım mekanizması yaratmaktadır. Ek olarak, ECM'nin gözenekli yapısı poroelastisite etkisi ile de enerjinin dağılımına katkı sağlamaktadır. Olağanüstü mekanik özelliklere sahip hidrojellerin sentezi için geliştirilen yöntemler de, dokularda olduğu gibi yapıda etkili bir enerji dağıtım mekanizması oluşturmayı esas almaktadır. Örneğin, yaklaşık 20 yıl önce literature giren çift ağyapı tekniği ile sentezlenen hidrojellerin mekanik özellikleri muazzam bir oranda iyileşmektedir. Bunun sebebi, jelin yapısını oluşturan ağyapılardan birisinin kuvvet altında kendisini feda ederek parçalanması; ancak diğer ağyapının bütünlüğü koruyarak tüm sistemin parçalanmasına engel olmasıdır. Diğer bir deyişle, mekanik enerjinin bir kısmı parçalanan ağyapı tarafından dağıtılarak tüm sistem toplamda daha yüksek tokluğa sahip olmakta ve daha fazla mekanik deformasyona dayanacak hale gelmektedir. Çift ağyapılı jellerin haricinde topolojik jeller ve nanokompozit jeller de benzer yaklaşımla sentezlenen, mekanik mukavemeti yüksek yumuşak malzemeler arasındadır.

Bu doktora tezinin ana konusunu oluşturan kriyojeller de mekanik dayanımı yüksek malzemelerin sentezi için geliştirilen bir yöntemdir ancak yukarıda bahsedilen jellerden önemli bir farklılığa sahiptir. Bu farklılık, kriyojellerin gözenekli bir yapıya sahip olmalarından ileri gelmektedir. Tamamı donmuş gibi gözüken ancak içerisinde donmamış bölgeler içeren sistemlerden sentezlenen kriyojellerde, donan fazın bir kalıp etkisi görmesi ile gözenekler oluşmakta; donmamış fazda gerçekleşen jelleşme reaksiyonları ile ise gözenek duvarları elde edilmektedir. Birbirleri ile bağlantılı makrogözenekli yapısı kriyojellerin dışarıdan gelen uyarılara da çok hızlı bir şekilde yanıt vermesine imkan tanımaktadır. Örneğin çift ağyapılı jeller her ne kadar mekanik olarak dayanıklı olsalar da, sentezlendikleri monomer veya polimerin özelliğine göre şişme dengesine ulaşmaları günler hatta haftalar sürmektedir. Diğer yandan kriyojellerin kütlece ve hacimce şişme dengesine ulaşması saniyeler içerisinde bile gerçekleşebilmektedir. Parçalanmadan tekrar tekrar sıkıştırılabilme ve uygun çözücülerde çok kısa süreler içinde şişebilme özelliği ile sünger-benzeri kriyojeller, birçok farklı uygulamada kullanıma uygundur.

Kriyojeller, sulu ya da organik çözeltilerden veya kolloidal dispersiyonlardan elde edilebilmektedir. Kriyojelleşme yöntemi ile bir kriyojel sentezlemek için ilk olarak uygun bir başlangıç sistemi seçilmeli, ardından bu sistem içerdiği çözücünün donma noktasının altında bir sıcaklığa soğutulmalıdır. Çözücü donarken içerisinde çözünmüş reaktifler dışlanarak yüksek konsantrasyonlu donmamış bölgeleri oluştururlar. Jelleşme reaksiyonları bu donmamış bölgelerde meydana gelirken; donan çözücü kristalleri de kalıp etkisi göstererek kriyojelleşme işlemi ile bir kriyojel sentezlenmiş olur. Jelleşme işleminin ardından oda sıcaklığına getirilen kriyojeller, bu durumda gözeneklerinin içerisinde sentez sırasında donmuş, ancak oda sıcaklığında tekrardan erimiş olan çözücüyü içermektedir. Çözücünün gözeneklerden dondurmalı-kurutucu gibi bir kurutma yöntemi ile uzaklaştırılması ile de kuru durumda bir kriyojel iskeleti elde edilir.

Bu tez kapsamında hem sulu hem de organik çözeltiler başlangıç sistemi olarak seçilerek bunlardan sırası ile hidro-kriyojeller ve organo-kriyojeller sentezlenmiştir. Dolayısı ile tez, hidro- ve organo-kriyojellerle ilişkili olacak şekilde 2 ana kısımda ele alınabilir. Saygın bilimsel dergilerde yayınlanmış 3 adet makaleden oluşturulmuş bu tezde ilk iki makale hidro-kriyojeller ile, son makale ise organo-kriyojeller ile ilgilidir. Hidro-kriyojeller, ipek fibroin proteininin sulu çözeltilerinden sentezlenmiştir. İpek fibroin, bazı örümcek türleri ve ipek böceğinden elde edilen doğal bir polimerdir. Fibroin, sahip olduğu biyouyumluluk, kolay işlenebilirlik ve yüksek mekanik mukavemet gibi özelliklerinden dolayı tez kapsamında çalışılan ana malzemelerden birisi olarak seçilmiştir. İpek fibroin kriyojellerinin sentezinden önce tek eksenli dondurma yöntemi ile çözücünün belli bir yönde donması sağlanarak gözenekler yönlendirilmiştir. Bu sistemin uygulanma amacı, dokularda gözlenen anizotropik özelliklerin tez kapsamında sentezlenen ipek fibroin kriyojellerinde de yaratılmasıdır. Böylece, biyolojik uygulamalarda kullanıma uygun, anizotropik mekanik özelliklere sahip ipek fibroin esaslı biyomalzemeler üretilmiştir. Organo-kriyojellerin sentezinde ise bütil kauçuğun benzen içerisindeki organik çözeltileri kullanılmıştır. İzopren ve izobütilen kopolimeri olan bütil kauçuk sentetik bir kauçuk türü olup, endüstride ve akademide oldukça fazla talep görmektedir. Bu tez kapsamında ise bütil kauçuk, çevresel uygulamalarda organik kirleticilerin örneklenmesinde kullanılmak üzere makrogözenekli organo-kriyojellerin üretiminde kullanılmıştır.

Birinci makalede anizotropik ipek fibroin kriyojelleri, reaksiyon çözeltisini içeren reaktörlerin (polipropilen şırıngalar) ilk olarak sıvı azota belli bir yönde ve hızda

daldırılması (tek eksenli dondurma), ardından -18 °C'de 24 saat bekletilmeleri (kriyojelleşme) ile üretilmiştir. Reaksiyon çözeltisi ipek fibroinin sulu çözeltisi olup, %4.2 ağ/hac konsantrasyonunda ipek fibroinin yanında kimyasal çapraz bağlayıcı olarak 1,4-bütandiol diglisidil eter (BDDE) ve pH ayarlayıcı olarak *N,N,N',N'*-tetrametiletilendiamin (TEMED) içermektedir. İlk aşamada çözeltiler 2.5 ile 35 $mm.dak^{-1}$ arasında değişen hızlarla sıcaklığı -196 °C olan sıvı azota daldırılmıştır. İkinci basamakta ise belli bir yönde donması sağlanan çözeltiler kriyojelleşme işlemi için -18 °C'ye ısıtılmış, sonuç olarak ipek fibroinin BDDE ile çapraz bağlanması ile makrogözenekli bir protein ağyapısı (kriyojel) elde edilmiştir. Yönlenmiş gözeneklerinden dolayı anizotropik mekanik özelliklere sahip kriyojellerin anizotropiklik oranları sıvı azota daldırma hızının 2.5'dan 20 $mm.dak^{-1}$ artması ile önce artmakta, daha yüksek daldırma hızlarında ise düşmeye başlamaktadır. Diğer bir deyişle, en yüksek anizotropiklik oranı sıvı azota 20 $mm.dak^{-1}$ hızla daldırılan ve ardından kriyojelleşmeye maruz bırakılarak elde edilen kriyojelde gözlenmiştir. Örneğin, bu kriyojelin kuru durumdaki Young's modül değerleri donma yönüne paralel ve dik yapılan sıkıştırma testlerinde sırası ile $3.4 \pm 0.5$ ve $0.8 \pm 0.3$ MPa olarak tespit edilmiştir. Yani kriyojeller, yapılan sıkıştırma testinin yönüne göre 4 kattan fazla değişen bir mekanik özelliğe sahiptir. Ek olarak kriyojeller her iki yönde de parçalanmadan tamamen ardışık olarak sıkıştırılabilmektedir.

İkinci makalede ise aynı reaksiyon çözeltisini daha etkili bir şekilde tek yönlü olarak dondurmak ve dolayısı ile anizotropiklik oranını arttırmak için farklı bir deney düzeneği tasarlanmış ve kullanılmıştır. Bu düzenek, sıvı azot ile temas eden bakır bir plaka ve bu plakaya sabitlenmiş reaksiyon çözeltisinin konulduğu silindirik politetrafloroetilen (Teflon) bir borudan oluşmaktadır. Bakır ile teflonun seçilmesinin nedeni, ısı iletkenlik katsayıları arasında yaklaşık 1600 kat fark olması ve dolayısı ile çözeltinin aşağıdan yukarıya doğru donarken radyal olarak donma ihtimalini minimuma indirerek anizotropiklik oranını arttırmaktır. Ayrıca, bir önceki çalışmadan farklı olarak bu makalede ipek fibroin konsantrasyonu %2.1 ile %16.7 ağ/hac arasında değiştirilerek ipek fibroin miktarının da kriyojeller üzerine etkisi incelenmiştir. Tüm kriyojeller yönlenmiş gözeneklerinden dolayı anizotropik mekanik ve şişme özelliklerine sahip olup, en yüksek modül anizotropiklik oranı en düşük ipek fibroin konsantrasyonunda (%2.1 ağ/hac) sentezlenen kriyojelde elde edilmiştir. Şöyle ki, kuru durumdaki kriyojel için donma yönüne paralel ve dik yapılan sıkıştırma testlerinde Young's modül değerleri sırası ile $2.30 \pm 0.50$ ve $0.11 \pm 0.03$ MPa olarak belirlenmiştir. Bu değerler 20 kattan fazla bir farka karşılık gelip, bu anizotropiklik oranı şimdiye kadar literatürde rapor edilen en yüksek oranlardan biridir. Diğer yandan tüm kriyojeller %85'in üzerinde bir gözenekliliğe sahiptir ve parçalanmadan %100'e kadar tekrar tekrar sıkıştırılabilmektedir. Yapılan döngüsel testler ile fibroin konsantrasyonundan ve test yönünden bağımsız olarak malzemeye verilen mekanik enerjinin de yaklaşık %60'ının dağıldığı hesaplanmıştır. Bu yüksek enerji dağıtım yeteneği kriyojellerin makrogözenekli mimarisi ile ilgilidir ve dokularda da enerji dağılım mekanizması olarak karşımıza çıkan poroelastisite adlı olgu ile açıklanabilir: Gözeneklerin içindeki su, sıkıştırılamazlığından ötürü kuvvet altında ezilen malzemeden dışarı çıkmaya başlar. Verilen enerjinin bir kımı da suyun gözeneklerden çıkması esnasında oluşan sıvı-katı (su-gözenek) ve katı-katı (gözenek-gözenek) sürtünmesinden dolayı dağılmaktadır. Ayrıca, yapılan reolojik ölçümler ile bir deformasyon altında malzemeden dışarı çıkan suyun malzemeyi kayma gerinimine karşı koruduğu da ortaya koyulmuştur. Diğer bir değişle, yaklaşık %10'luk bir kayma gerinimin üzerinde malzemenin *tan δ* değerinin 1'in üzerine çıktığı, yani sanki katı halden sıvı hale geçmiş gibi davrandığı görülmüştür. Bu bulgu, cihazın gözeneklerden

çıkan suyu ölçmesi, dolayısı ile kriyojelin sıvılaşmış gibi görülmesi ile ilişkilendirilmiştir. Devamında yapılan ölçümler, kayma geriniminin tekrardan düşürülmesi ile malzemenin gözeneklerinden çıkan suyu tekrardan emerek, ilk halini tamamen geri kazandığını göstermiştir. Sonuç olarak, gözeneklerden çıkan su, mekanik enerjinin dağılımına katkı sağlarken, malzemeyi yüksek kayma gerinimlerine karşı da korumaktadır.

Üçüncü makalede ise farklı nesil gözenek yapılarına sahip bütil kauçuk organo-kriyojelleri, su ortamından polisiklik aromatik hidrokarbon (PAH)'ların örneklenmesi amacıyla bir "pasif örnekleyici" olarak geliştirilmiştir. Pasif örnekleme, canlılar için çok ciddi zararlara sebep olabilen organik kirleticilerin su, hava gibi ortamlardan izlenmesi ve denetlenmesi için geliştirilmiş bir yöntem olup, diğer örnekleme tekniklerine göre üstün avantajlara sahiptir. Ancak, literatürde şimdiye kadar rapor edilen ve ticari olarak kullanılan pasif örnekleyiciler çok fazlı malzemelerdir. Yani, yapılarında örnekleme işlemini karmaşıklaştıran birden fazla bileşen bulunmaktadır. Diğer yandan bu örnekleyiciler gözenekli bir yapıya sahip olmadıkları için, organik kirleticileri absorplaması ve örneklemesi uzun zaman almaktadır. Bu sorunların üstesinden gelebilmek için, temel bileşen olarak yalnızca bütil kauçuk içeren tek fazlı ve makrogözenekli organo-kriyojeller tez kapsamında üretilmiştir. Kriyojellerin gözenek boyut ve dağılımlarının farklı sayıda aromatik halka içeren PAH'lar için uygun olabilmesi için, tek ağyapılı kriyojelin yanında çift ve üç ağyapılı kriyojeller de tasarlanmıştır. İlk olarak tek ağyapılı bütil kauçuk kriyojeli benzen çözeltilerinden, %5 ağ/hac kauçuk konsantrasyonunda ve sülfür monoklorür ($S_2Cl_2$) çapraz bağlayıcısı varlığında sentezlenmiştir. Elde edilen kriyojelin benzer kauçuk çözeltisine daldırılması ve ardından yapılan kriyojelleşme işlemi ile çift ağyapılı kriyojel sentezlenmiştir. Yani, ikinci kriyojelleşme tek ağyapılı kriyojelin gözenekleri içerisinden gerçekleştirilmiş, böylece yeni nesil gözenekler oluşturulmuştur. Üç ağyapılı kriyojel ise benzer şekilde çift ağyapılı kriyojelden üretilerek, kriyojel yapısında üçüncü nesil gözenekler yaratılmıştır. Tüm kriyojeller yüksek mekanik mukavemete sahip olup; yüksek sıkıştırılabilirlik özelliklerinin yanında %400'den fazla bir oranda da çekilebilmektedir. Naftalin, fenantren, floranten ve piren gibi PAH'lar ile yapılan örnekleme testlerinde ise tüm kriyojellerin ticari olarak kullanılan gözeneksiz örnekleyici PDMS'den daha iyi bir performans gösterdiği gözlenmiştir. Kriyojellerin kendi içindeki örnekleme performansları ise doğrudan gözenek yapıları ile ilişkilidir. Şöyle ki, en büyük gözenek boyutlarına ve hacmine sahip olan tek ağyapılı kriyojel, PAH'ları en hızlı şekilde absorbe ederken; en küçük gözenek boyut ve hacmine sahip üç ağyapılı kriyojel ise yavaş bir şekilde PAH'ları absorplamaktadır. Diğer yandan, tek ağyapılı kriyojel hızlı bir şekilde absorplama yapmasına ragmen, büyük gözeneklerinden dolayı PAH'ların bir kısmını tekrardan su fazına verdiği; ancak üç ağyapılı kriyojelin daha küçük gözenekleri sayesinde daha fazla PAH'ı yapısında biriktirebildiği ortaya konmuştur.

Sonuç olarak, bu doktora tezi kapsamında sulu ve organik çözeltilerden hidro- ve organo-kriyojeller üretilmiş ve başarılı bir şekilde karakterizasyonları yapılmıştır. Biyouyumlu hammaddelerden sentezlenen ipek fibroin hidro-kriyojellerinin sahip olduğu anizotropik üstün mekanik özellikleri ile doku mühendisliği uygulamalarında uygun olduğu düşünülmektedir. Diğer yandan, gözenek boyut ve dağılımlarının ayarlanabildiği, yüksek tokluk ile çekilebilme özelliğine sahip bütil kauçuk organo-kriyojellerinin ise PAH gibi organik bileşiklerin su fazından örneklenmesi için tek fazlı ve makrogözenekli bir pasif örnekleyici olarak kullanılabileceği gösterilmiştir.

# 1. INTRODUCTION

We know that the planet earth is more than 4- billion- years- old and the showing up the earliest life forms on our planet dates to 3.5 billion years ago. During these enormous time scales, the environment has inevitably changed and living beings have to adapt their surroundings via evolution to survive. Over billions of years of evolution, nature has thus crafted all living creatures into their most proper forms and we can meet with several millions of different species living today [1]. Even though these living species are obviously considered as a work item for biology, they can be also investigated from perspectives of chemistry and physics as they are actually a combination of soft and hard materials that hierarchically originated from well-arranged atoms and molecules.

Cells and tissues, for instance, are nature's life-sustaining jelly-like soft materials that withstand significant mechanical stresses during the lifespan of a living creature. Their mechanical resilience and stability are based upon two viscoelastic composite networks originated from interconnected biopolymers, namely the cytoskeleton and the extracellular matrix (ECM), located inside and outside of a cell, respectively [2]. For instance, in the cytoskeleton, actin filaments are crosslinked by unique proteins such as α-actinin and fascin to generate a skeletal framework within the cell [3,4]. In the ECM, collagen, which is a fibrous structural protein mainly found in connective tissues, is crosslinked through lysine residues via lysyl oxidase enzyme to form a highly stiff and elastic protein network, while glycosaminoglycans form a soft gel providing an energy dissipation within the collagen network [5,6]. These highly well-organized biological materials thus possess exclusive mechanical properties such as a high toughness, high stretchability and compressibility, and fatigue resistance. Moreover, most tissues have direction-dependent mechanical and viscoelastic properties, i.e. anisotropy, due to fine alignment of the fibers and filaments [7-10].

Hydrogels are man-made tissue-like soft materials composing of a hydrophilic polymer network diffused by a high amount of water [11]. Therefore, it is not a surprise that hydrogels have been commonly researched and utilized in several biological

applications such as drug delivery [12], wound dressing [13] and tissue engineering [14]. Although hydrogels were discovered almost a half-century ago, they have been still intensively and progressively studied by material scientists. Apart from their great potentials in numerous application areas, one of the main reasons for that intense research is to overcome their mechanic deficiencies. In another word, hydrogels prepared by traditional approaches suffer from mechanical weakness and brittleness due to their non-energy dissipative network [15]. As a consequence, material scientists have developed various techniques for years to enhance the mechanical properties of the hydrogels and to bring them the ability of mimicking nature's soft materials literally.

Gels with multiple networks (double network, triple network, etc.), interpenetrating gel systems, nanocomposite gels and topological (slide-ring) gels are amongst these techniques, which improve the mechanical stability of a traditional gel dramatically by using different approaches [16-20]. For instance, multiple network gels and interpenetrating gels contain at least two individual but interwoven polymer networks, in which one of them sacrifices itself and dissipate the mechanical energy [17]. This phenomenon thus prohibits the instantaneous disintegration of the complete gel under deformation and inevitably improves the toughness of the gel. On the other hand, a nanocomposite gel contains clay nanoparticles within the gel system, which serve as dynamic (physical and reversible) multifunctional crosslinking points enhancing the mechanical properties of traditional hydrogels and providing self-healing ability [19].

Cryogelation is also considered amongst these techniques as it unbelievably improves the mechanical durability of a gel, especially its compressibility. Cryogelation is a liquid phase gelation method taking place in the unfrozen fractions of a macroscopically frozen system. In order to obtain a gel via cryogelation, solutions or colloidal dispersions of appropriate precursors are first cooled down to a subzero temperature, i.e. below the crystallization point of the solvent. During freezing, reactant-enriched unfrozen liquid microphase which is surrounded by the solvent crystals is formed, that is, "cryoconcentration" takes place. Gelation reactions can only occur in these unfrozen microparts of the system. After thawing, a cryostructured macroporous gel called "cryogel" is formed due to the in-situ template effect of the frozen solvent [21].

The main difference of the cryogelation from the aforementioned toughening techniques is that, it does not only improve the mechanical performance of gels, it also creates a macroporous architecture. This kind of interconnected porous morphology not only provides a high toughness via poroelasticity effect, but it also accelerates stimuli responsivities of the material [22]. For instance, a cryogel can easily reach the weight and volume swelling equilibrium in a good solvent within seconds.

While water-based cryogels (hydro-cryogels) are very popular and demanded in several biological applications, organic solvent-based cryogels (organo-cryogels) can also be prepared and used in other applications [21,22]. In the scope of this thesis, mechanically durable hydro- and organo-cryogels were prepared by using silk fibroin (SF) and butyl rubber (IIR), which are considered suitable materials for tissue engineering and environmental applications, respectively.

### 1.1 Purpose of The Thesis

The aim of this thesis is to fabricate SF-based hydro-cryogels and IIR-based organo-cryogels that are suitable for different application areas. The thesis based on three publications consists of two main parts associated with the hydro- and organo-cryogels. The first two publications are related to SF hydro-cryogels and the last one is on the preparation of IIR organo-cryogels.

Hydro-cryogel part of the thesis composes of two publications as mentioned above, in which anisotropic SF cryogels possessing aligned pore morphology were reported. Creating anisotropic mechanical properties in synthetic materials as observed in tissues has been a real challenge for scientists. In contrast to non-porous materials, it is more feasible to create anisotropy in porous materials via manipulation of their pores to align throughout one specific direction by using uniaxial freezing. Consequently, we prepared anisotropic SF based cryogels within the scope of the thesis. SF is a natural biopolymer produced by some spiders and silkworms [23]. Due to its extraordinary properties such as biocompatibility, easy processability and excellent mechanical properties, SF has become one of the most demanded biopolymers in biological applications [23].

On the other hand, organo-cryogel part of the thesis is based on IIR cryogels, as revealed in the third publication. IIR is an isobutylene-isoprene copolymer and it has

become an important raw material intensely utilized in both industry and academia [22]. Within the scope of the thesis, organic solutions of IIR were exploited to fabricate hydrophobic organo-cryogels as single-phase macroporous passive samplers, which can easily compete with commercial passive samplers.

In the first publication, anisotropic SF cryogels were obtained after immersing the reactors containing aqueous SF reaction solutions into liquid nitrogen directly at various immersion rates. Obtained cryogel scaffolds exhibited a Young's modulus in the range of MPa and sustained up to 20 MPa compressive stresses. In addition to their high mechanical strength, they also had anisotropic microstructure and hence anisotropic mechanical properties, e.g., the Young's modulus ($E$) is $3.4 \pm 0.5$ MPa and $0.8 \pm 0.3$ MPa when measured along the directions parallel and vertical to the freezing direction, respectively.

In the second publication, we presented a different experimental set-up consisting of a copper bottom plate and a cylindrical polytetrafluoroethylene (PTFE) mold in order to fabricate new series of anisotropic SF cryogels. The copper bottom plate was immersed in a cold bath at -30 or -196 °C, whereas the cylindrical PTFE mold locating outside of the cold bath was filled with aqueous solutions of SF of various concentrations. Unidirectionally frozen SF solutions were then subjected to cryogelation at -18 °C. Finally, we obtained mechanically strong SF scaffolds exhibiting microstructural, swelling and mechanical anisotropies. The scaffolds exhibited the highest modulus anisotropy so far reported to our knowledge, $21 \pm 5$, with moduli $E = 2.3 \pm 0.5$ and $0.11 \pm 0.03$ MPa measured along parallel and perpendicular to the freezing direction, respectively. We also demonstrated that, independent on the fibroin concentration or direction of the measurements, 60% of the mechanical energy given to the cryogels are dissipated due to the friction between the fibroin pore walls (i.e. poroelasticity), which is responsible for their squeezability and self-recoverability.

In the third publication, i.e. the organo-cryogel part of the thesis, cryogelation technique was applied on organic solutions of butyl rubber (IIR) to obtain macroporous IIR cryogels for passive sampling applications. Passive sampling is an efficient technique for monitoring the dissolved concentration of polycyclic aromatic hydrocarbons (PAHs) in aquatic systems. Here, a series of novel macroporous rubber cryogels, i.e. sorbents, with single (SN), double (DN) and triple (TN) network

structures, as passive samplers with tunable pore morphologies, extraordinary mechanical properties, and high sorption rates and capacities for PAHs were presented. Sorbent materials based on SN, DN, and TN butyl rubber were prepared via cryogelation technique from butyl rubber solutions in benzene as the solvent at -18 °C using sulfur monochloride ($S_2Cl_2$) as a cross-linker. To obtain rubber sorbents with DN and TN structures, cryogelation reactions were conducted within the pores of dry SN and DN rubber cryogel networks, respectively. It was shown that the SN rubber cryogel absorbs most rapidly PAHs which are attributed to its largest porosity and pore volume. Moreover, the TN cryogel had the highest sorption capacity because of its smaller pores and low porosity, preventing the escape of PAHs from the cryogel to the solution phase. Besides, all rubber-based organo-cryogels possessed high mechanical properties, such as stretchability above 400%, compressibility up to 40 MPa stress and fatigue resistance.

## 2. HIGH-STRENGTH SILK FIBROIN SCAFFOLDS WITH ANISOTROPIC MECHANICAL PROPERTIES[1]

Hydrogels are chemically or physically cross-linked polymers absorbing large quantities of water without dissolving [24]. Softness, smartness, high water sorption capacity, and similarity to biological tissues make hydrogels unique soft materials. However, there is still a clear distinction between synthetic hydrogels and biological tissues with regard to the microstructure and structure-related mechanical properties. In contrast to the isotropic morphologies of synthetic hydrogels, many tissues including muscles [25], tendon [26], cartilage [27], intervertebral disc [28], and cornea [29] possess anisotropic hierarchical morphologies leading to extraordinary mechanical properties that cannot be mimicked by synthetic materials. Biocompatible anisotropic hydrogels with a good mechanical performance have a broad range of potential applications in tissue engineering, bioseparation, microfluidics, and organic electronics [30].

To prepare gels with anisotropic properties, several strategies have been presented in the past years including directional freezing [30,31], strain-induced reorientation [32-37], self-assembly [38-40], dielectrophoresis [41], micropatterning [42], and 3D printing [43]. Directional freezing is a simple and promising approach to the preparation of aligned porous materials [30,31]. By this technique, the growth of solvent crystals during freezing of a polymer solution is controlled in one direction, e.g., by immersing the reactor containing the solution into a cold bath at a controlled rate. Uniaxial freezing of the solutions of synthetic and natural polymers such as polyvinyl alcohol (PVA) [44], agar [45], agarose [46], chitosan [47], alginate [48,49], collagen [50], gelatin [51], soy proteins [52], silk fibroin [53,54], or colloidal solutions of polymers and nanoparticles [31], such as PVA and silica in a cold bath followed by removing oriented solvent crystals via freeze-drying produce aligned porous materials

[1] This chapter is based on the paper "Yetiskin, B., & Okay, O. (2017). High-strength silk fibroin scaffolds with anisotropic mechanical properties. *Polymer*, *112*, 61-70."

with various microstructures. However, such materials generally dissolve in good solvents and exhibit poor mechanical properties due to the absence of chemical cross-links interconnecting the polymer chains or the particles, limiting their application areas. For instance, anisotropic scaffolds based on chitosan/alginate produced by directional freezing exhibit a Young's modulus of around 5 kPa [49], while gelatin scaffolds rupture under 0.23 MPa compressive stresses [51]. However, anisotropic scaffolds suitable for tissue engineering applications should sustain high stresses in the order of MPa to protect their integrity.

An alternative strategy is to combine the directional freezing with the cryogelation technique to prepare mechanically strong anisotropic gels. Cryogelation is a simple route to produce 3D highly porous polymer networks of high toughness and superfast responsivity [55,56]. Cryogelation reactions are conducted below the freezing point of the reaction solution, during which the solvent crystals are in equilibrium with the unfrozen liquid microchannels containing cryo-concentrated reactants [55]. Thus, the reactions only proceed in the unfrozen microchannels leading to the formation of macroporous gels with thick pore walls. The combined directional freezing - cryogelation approach was first reported by our group in 2008 to produce butyl rubber (IIR) organogels with an aligned porous structure [57]. IIR solution in cyclohexane was first directionally frozen below the melting point of the solution and then IIR chains are intermolecularly cross-linked in the frozen solution using sulfur monochloride as a cross-linker. The anisotropic IIR organogels are very tough and can be compressed up to about 99% strain without any crack development [57]. Several research groups have recently reported the combination of the directional freezing technique with redox-, gamma-, or UV-initiated crosslinking cryopolymerization to prepare hydrogels based on chemically cross-linked poly (meth)acrylates with anisotropic morphologies and mechanical properties [58-63]. For instance, poly (ethylene glycol) diacrylate scaffolds produced by directional freezing - cryopolymerization technique exhibit a Young's modulus of 8 kPa and 80 kPa during compressions along the directions perpendicular and parallel to the freezing direction, respectively [59].

Silk fibroin gels are important materials due to their attractive properties such as a high mechanical strength, biocompatibility, and controlled degradability [64-66]. Gelation

of silk fibroin in aqueous solutions mainly occurs by self-assembly of fibroin molecules via intermolecular β-sheet crystallites acting as physical cross-links. The formation of β-sheets and hence fibroin gelation can be induced by several triggers such as pH [67], temperature [68], fibroin concentration [69], cations [70], diepoxide crosslinkers [71], vortexing [72], and electrical field [73]. In tissue engineering applications, a high mechanical strength and an interconnected open pore structure with micrometer-sized pores are essential considerations in the development of silk fibroin gels and scaffolds. In addition, an anisotropic microstructure and anisotropic mechanical properties are also required in fibroin scaffolds to mimic the biological tissues. To our knowledge, there is only one report on the preparation of silk fibroin scaffolds with anisotropic mechanical properties [53]. These scaffolds were prepared by uniaxial freezing of aqueous fibroin solutions followed by freeze drying to fix the anisotropic microstructure formed due to the ice template. Because the scaffolds are soluble in aqueous environment, they were finally treated with methanol to induce the formation of β-sheets [53]. The scaffolds thus produced exhibit a low mechanical strength, e.g., their Young's modulus is below 4 kPa [53]. This is expected due to the fact that the cross-linking occurs after forming the pore walls of the scaffold leading to the formation of weak intermolecular bonds.

The aim of this study was to prepare high-strength biocompatible scaffolds with anisotropic mechanical properties. Here, we describe preparation of anisotropic silk fibroin cryogels and scaffolds exhibiting a Young's modulus in the range of MPa that sustain up to 20 MPa compressive stresses. The cryogels were prepared by a combined directional freezing - cryogelation process starting from an aqueous 4.2 wt% fibroin solution containing butanediol diglycidyl ether (BDDE) cross-linker and *N,N,N',N'*-tetramethylethylenediamine (TEMED). In the first step, the reactor containing the aqueous solution of fibroin, cross-linker, and TEMED was immersed into liquid nitrogen at a controlled rate to create a directionally frozen ice template. In the second step, the cryogelation reactions were conducted in this frozen solution at -18 °C whereby the cryoconcentrated fibroin in the unfrozen microzones of the reaction system forms a 3D fibroin network. The scaffolds exhibit anisotropic microstructure and hence anisotropic mechanical properties, e.g., the Young's modulus is 3.4 ± 0.5 MPa and 0.8 ± 0.3 MPa when measured along the directions parallel and vertical to the freezing direction, respectively. As will be seen below, all the cryogels could

completely be compressed due to squeezing out of water from their pores. Upon removal of the load, the compressed cryogels immediately recover their original dimensions and mechanical properties by absorbing the released water into their pores.

## 2.1 Experimental Section

### 2.1.1 Materials

The cross-linker butanediol diglycidyl ether (BDDE, Sigma Aldrich), *N,N,N',N'*-tetramethylethylenediamine (TEMED, Sigma Aldrich), $Na_2CO_3$ (Merck), and LiBr (Merck) were used as received. *Bombyx mori* cocoons were purchased from Bursa Association of Agricultural Sales Cooperatives for Silk Cocoons (Kozabirlik, Turkey). Silk fibroin was separated from cocoons by boiling them for 1 h in aqueous solution of 0.02 M $Na_2CO_3$ to remove the sericin proteins followed by washing the remaining fibroin three times with distilled water at 70 °C, for 20 min each [67]. Silk fibroin was dissolved in aqueous 9.3 M LiBr at 60 °C for ~2 h and then dialyzed using dialysis tubing (10000 MWCO, Snake Skin, Pierce) for 3 days against water that was changed three times a day [67]. After centrifugation, the final concentration of silk fibroin in aqueous solution was about 5 w/w%, which was determined by weighing the remaining solid after drying.

### 2.1.2 Preparation of fibroin cryogels

Anisotropic fibroin cryogels were prepared by directional freezing of aqueous 4.2 wt% fibroin solution containing BDDE crosslinker and TEMED (0.25 v/v%) in liquid nitrogen followed by conducting the cryogelation reactions at -18 °C for 24 h. BDDE concentration in the fibroin solution was set to 20 mmol epoxy per gram of fibroin [71]. Typically, 5 mL of 5 wt% fibroin solution were mixed with BDDE (0.50 mL), TEMED (15 mL), and water to make the final volume 6 mL. The homogeneous fibroin solution was then transferred into several 1 mL plastic syringes of 4 mm internal diameter. Each plastic syringe containing the gelation solution was then connected to the upper clamp of the Zwick-Roell test machine, which was moved downward at a constant rate *R* into a cold bath containing liquid nitrogen. Experimental apparatus for directional freezing of aqueous 4.2 wt% fibroin containing BDDE and TEMED is shown in Figure 2.1a. The immersion rate *R* of the syringes into liquid nitrogen controlled by the software of the test machine was varied between 2.5 and 35 $mm.min^{-1}$. The syringes were then placed in a cryostat at -18 °C to conduct the cryogelation

reactions for 1 day. Control experiments were also carried out as described above, except that the directional freezing step was not applied to the fibroin solutions.

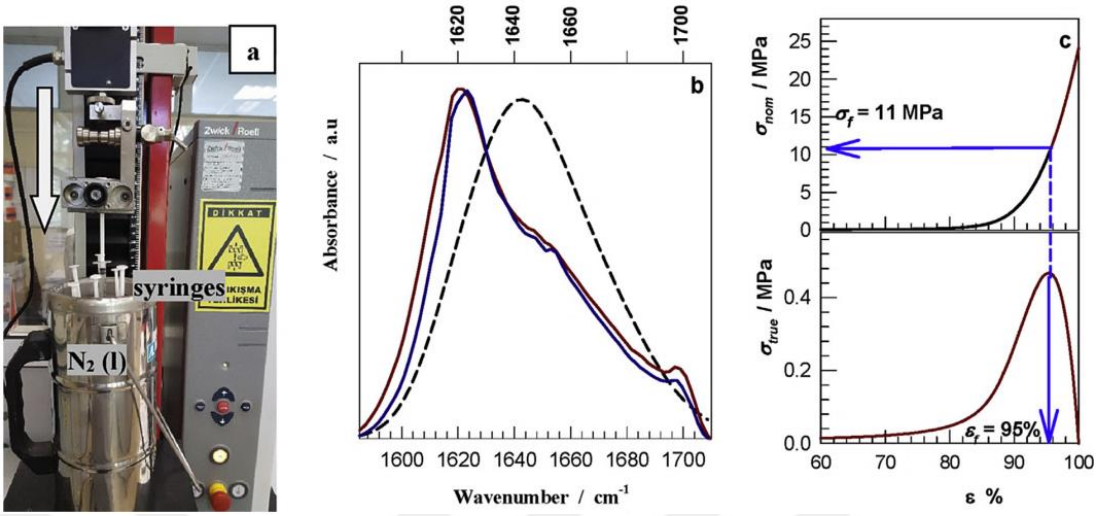


**Figure 2.1 :** (a): Experimental apparatus for the directional freezing of aqueous fibroin solutions. The syringes containing aqueous solution of fibroin, BDDE and TEMED are immersed in liquid nitrogen at a controlled rate *R* before conducting the cryogelation reactions at -18 °C. (b): Amide I region of ATR-FTIR spectra of freeze-dried silk fibroin before (dashed curve), and after directional freezing - cryogelation (solid curves) at *R*=2.5 (dark red) and 35 $mm.min^{-1}$ (dark blue). (c): Typical stress-strain curves of cryogel samples up to around 99% compressions where the nominal stress $\sigma_{nom}$ and true stress $\sigma_{true}$ are plotted against the compressive strain $\varepsilon$. *R*=20 $mm.min^{-1}$. The samples were compressed parallel to the freezing direction. The blue arrows indicate calculations of the fracture nominal stress $\sigma_f$ and fracture strain $\varepsilon_f$ from the maximum in $\sigma_{true}$ - $\lambda$ plot.

### 2.1.3 Swelling and gel fraction measurements

The frozen cryogel samples after preparation were first thawed at room temperature for 30 min and then immersed in a large excess of water for at least 3 days by replacing water several times to extract any soluble species. The swelling equilibrium was tested by weighing the gel samples as well as by measuring the diameter of the gel samples using a calibrated digital compass (Mitutoyo Digimatic Caliper, Series 500, resolution: 0.01 mm). The equilibrium swollen gel samples were taken out of water and immediately frozen at -25 °C for 1 day. The samples were freeze-dried at -40 °C under 0.12 mbar vacuum for 1 day and at -60 °C under 0.011 mbar for an additional 1 day. The freeze-drying system consisted of a freeze-dryer (Christ Alpha 2-4 LD plus) connected to a vacuum pump (Vacuubrand RZ 6). The pressure during freeze-drying was adjusted using a valve controller and monitored by an active digital controller. All cryogel samples were freeze-dried under the same conditions. The equilibrium weight

$q_w$ and volume swelling ratios $q_v$ were calculated as $q_w = m_{swl}/m_{dry}$ and $q_v=(D_{swl}/D_{dry})^3$, respectively, where $m_{swl}$ and $D_{swl}$ are the mass and the diameter of the equilibrium swollen gel sample, respectively, and $m_{dry}$ and $D_{dry}$ are the same quantities for the freeze-dried sample. The gel fraction $W_g$, that is, the conversion of fibroin to the 3D fibroin network (mass of water-insoluble fibroin/initial mass of the fibroin in the feed) was calculated from the masses of dry fibroin network and from the fibroin in the feed.

### 2.1.4 ATR-FTIR measurements

Fourier-transform infrared (FTIR) spectra of the freeze-dried samples were obtained using a single bounce diamond attenuated total refractance (ATR) module on a FTIR spectrometer (Nicolet Nexus 6700) equipped with a liquid nitrogen cooled mercurycadmium-telluride (MCT) detector.

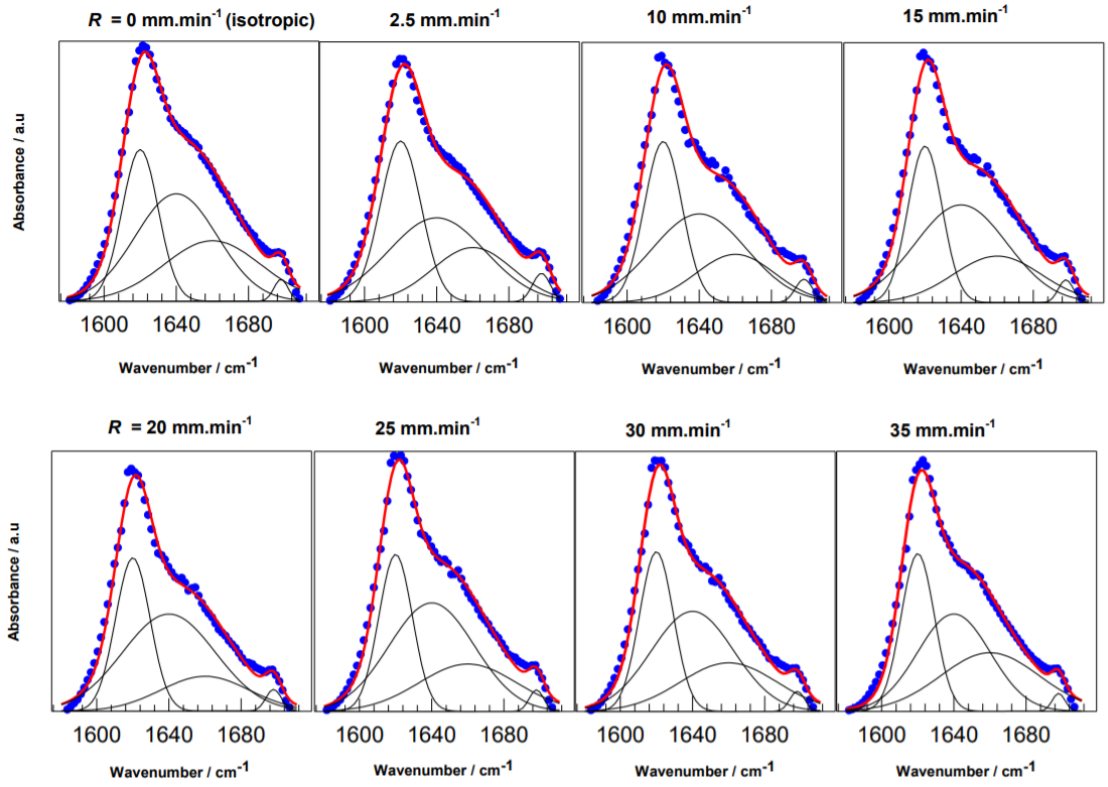


**Figure 2.2 :** Typical ATR-FTIR spectra of freeze-dried silk fibroin cryogel samples formed at various immersion rates *R* indicated. The original data are shown by the filled blue circles while solid curves are the results of curve fitting for the original spectra (thick red curves) and hidden peaks (thin black curves).

The resolution of each spectrum was 4 $cm^{-1}$, and 64 interferograms were coadded in the range of 500-4000 $cm^{-1}$. The dashed and solid curves in Figure 2.1b present the Amide I band region (1580-1720 $cm^{-1}$) of FTIR spectra of freeze-dried fibroin before

and after directional freezing - cryogelation, respectively. The peak at 1640 $cm^{-1}$ corresponding to the random coil conformation disappears after cryogelation and a new peak at 1620 $cm^{-1}$ appears which was assigned to β-sheet conformation [74,75]. In addition to this peak, shoulders at 1660 and 1698 $cm^{-1}$ are seen after cryogelation, which were assigned to the α-helix and β-turn conformations, respectively. To estimate the conformation of fibroin, FTIR spectra of the samples were analyzed using PeakFit software (Version 4.12, SeaSolve Software Inc.). Linear baseline correction was applied to the Amide I region before the band was deconvolved by Gauss Amplitude function [71]. For the curve fitting procedure, the initial band positions at 1620, 1640, 1660, and 1698 $cm^{-1}$, representing β-sheet, random coil, α-helix, and β-turn conformations, respectively, were fixed, allowing their widths and heights to vary (Figure 2.2).

### 2.1.5 Mechanical tests

Uniaxial compression measurements were conducted on cryogel samples both in equilibrium swollen and dried states. The samples were cut from the directions parallel and vertical to the freezing direction to obtain a rectangular shape of dimensions 33 ± 6 mm x 32 ± 4 mm x 2.2 ± 0.4 mm. The compression tests were performed at 23 ± 2 °C on a Zwick Roell test machine using a 500 N load cell [76]. An initial compressive contact to 0.05 N was applied to ensure a complete contact between the sample and the surface. Load and displacement data were collected during the experiments at a constant crosshead speed of 0.3 $mm.min^{-1}$. Compressive stress was presented by its nominal $\sigma_{nom}$ and true values $\sigma_{true}$, which are the force per cross-sectional area of the undeformed and deformed specimen, respectively. Assuming the sample volume remains constant during deformation, the true stress $\sigma_{true}$ was calculated as $\sigma_{true}=\lambda\ \sigma_{nom}$ where $\lambda$ is the deformation ratio (deformed length/original length). The compressive strain is given by the compression ratio $\varepsilon$ which is the change in the sample length relative to its initial length, i.e., $\varepsilon=1-\lambda$. Figure 2.1c shows typical stress-strain curves of fibroin cryogels, where the nominal $\sigma_{nom}$ and true stresses $\sigma_{true}$ are plotted against the strain $\varepsilon$. It is seen that although $\sigma_{nom}$ increases continuously with increasing strain up to about 99% compression, the corresponding $\sigma_{true}$ - $\lambda$ plot passes through a maximum revealing the onset of a failure in the cryogel specimen [76]. Therefore, the fracture nominal stress $\sigma_f$ and the fracture strain $\varepsilon_f$ were calculated from the maxima in $\sigma_{true}$ - $\lambda$ plots, as indicated by the blue arrows in the figure. The compression modulus

*E* was calculated from the slope of stress-strain curves between 2 and 4% compressions while the stress at 3% compression was reported as the compressive stress $\sigma_{comp}$. For reproducibility, at least six samples were measured for each sample and the results were averaged.

### 2.1.6 Texture determination

Cross-sectional scanning electron microscopy (SEM) studies were performed on freeze-dried cryogel samples at various magnifications between 20 and 1000 times in a field emission scanning electron microscope (JEOL JSM-6510LV). All samples were coated with gold for 3 min using a Sputter coater (S150 B Edwards) prior to the measurements. Texture determination of the freeze-dried and swollen cryogel samples was also carried out using an image analyzing system consisting of a microscope (XSZ single Zoom microscope), a CDD digital camera (TK 1381EG) and a PC with the data analyzing system Image-Pro Plus. For this purpose, cylindrical gel samples of 3.7 mm in diameter were cut into thin slices of about 1 mm in thickness. The measurements were conducted at magnifications between 10 and 100 times.

## 2.2 Results and Discussion

Anisotropic silk fibroin scaffolds were prepared by lowering the reactor containing an aqueous solution of fibroin, BDDE crosslinker, and TEMED into liquid nitrogen at a controlled rate followed by conducting the cryogelation reactions at -18 °C for 24 h (Figure 2.1a). The immersion rate *R* of the gelation solution into liquid nitrogen was varied between 2.5 and 35 mm.min$^{-1}$. In control experiments, cryogelation reactions were conducted without the immersion period, i.e., by cooling the solution from 23 ± 2 to -18 °C and keeping at this temperature for 24 h to obtain isotropic cryogels.

Figure 2.3a shows the equilibrium weight $q_w$ and volume swelling ratios $q_v$ of the cryogels and the gel fraction $W_g$ plotted against the immersion rate *R*. The data for isotropic cryogels are shown at *R*=0, as indicated by an arrow. The gel fraction $W_g$ representing the conversion of water-soluble fibroin to a 3D fibroin network is 1.3 ± 0.2 indicating a complete conversion, and the presence of bound water that cannot be separated by freeze-drying [77]. As detailed before [71,78], BDDE reacts with the amino groups on fibroin to form intermolecular cross-links, whereby the mobility of fibroin molecules significantly reduces triggering the conformational transition in

fibroin from random coil to β-sheet structure. The insolubility of fibroin after the directional freezing - cryogelation process also suggests formation of β-sheet crystallites acting as interstrand cross-links.

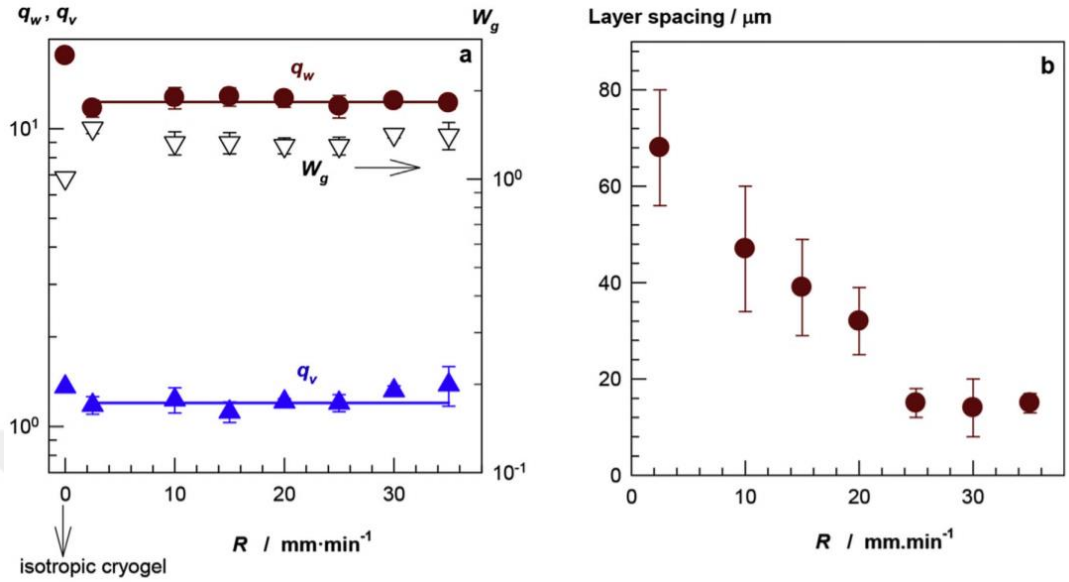


**Figure 2.3 :** (a) The gel fraction $W_g$ (open symbols), equilibrium weight $q_w$ (filled circles) and volume swelling ratios $q_v$ of the cryogels (filled triangles) shown as a function of the immersion rate $R$. The data at zero immersion rate are for isotropic cryogels. (b) Spacing between fibroin layers, i.e., channel width in anisotropic cryogel scaffolds shown as a function of $R$.

Indeed, the results of β-sheet contents estimated from the analysis of the Amide I band region of FTIR spectra show that fibroin chains before gelation have 12 ± 2% β-sheet structures, while their contribution increases to 28 ± 1 and 31 ± 2% in isotropic and anisotropic cryogels, respectively (Figure 2.4). The higher β-sheet content of anisotropic cryogels as compared to the isotropic ones indicates that freezing in liquid nitrogen before cryogelation promotes β-sheet crystallization. Figure 2.3a also reveals that both the weight $q_w$ and volume swelling ratio $q_v$ of anisotropic cryogels are independent on $R$ and they equal to 12.3 ± 0.4 and 1.2 ± 0.1, respectively. Isotropic cryogels exhibit a slightly higher degree of swelling and a gel fraction $W_g$ of 1.1 ± 0.1 indicating that the immersion period increases the amount of bound water in the cryogels.

The fact that the mass of the cryogels 12-fold increases upon swelling in water while their volume remains almost constant suggests that the swelling process of the cryogels is mainly governed by filling of their pores with water [79]. Assuming the pore volume remains constant during swelling, the total porosity $P$ can be estimated from the weight

and volume swelling ratios using the equation [79]: $P = 1 - q_v[1+(q_w-1)\rho]$ where $\rho$ is the fibroin density (1.35 g.mL$^{-1}$) [80]. Calculations show that the porosity $P$ of both isotropic and anisotropic cryogels is 93 ± 1% indicating their highly porous structure.

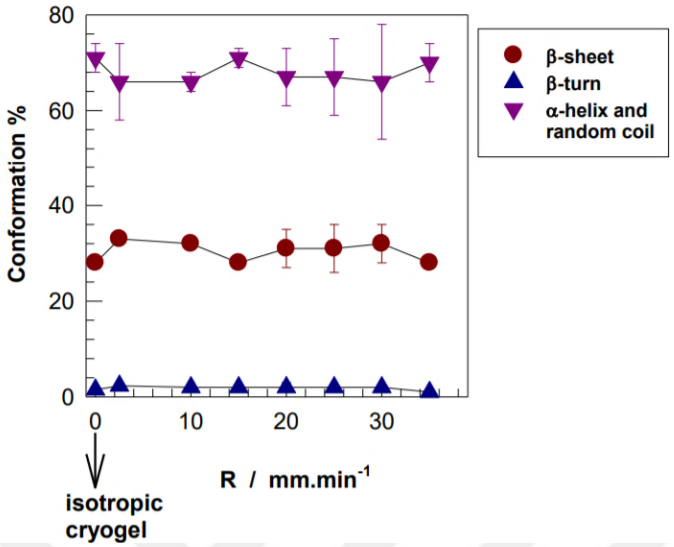


**Figure 2.4 :** Contents of β-sheets, β-turns, α-helix and random coil conformations of silk fibroin network strands in freeze-dried cryogels plotted against the immersion rate *R*.

Indeed, cross-sectional optical images of isotropic and anisotropic cryogel samples shown in Figure 2.5a and 2.5b-d, respectively, reveal existence of micrometer-sized pores. The isotropic cryogel has a disordered pore structure within an interconnected 3D fibroin network while all cryogels prepared after directional freezing e cryogelation process possess long aligned fibroin layers interconnected with fibroin branches forming a 3D network containing macropores.

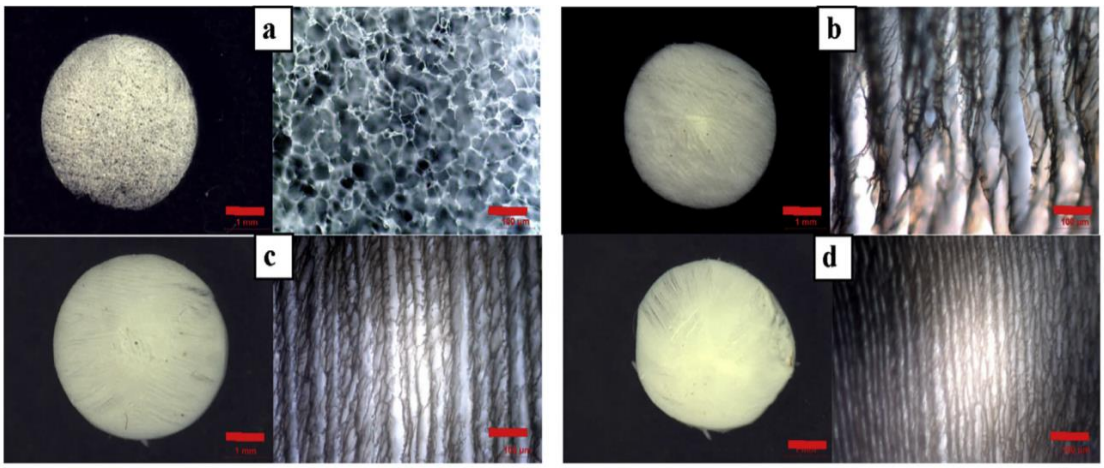


**Figure 2.5 :** Optical images of isotropic (a) and anisotropic fibroin cryogels (b-d). *R*=10 (b), 25 (c), and 35 (d) mm.min$^{-1}$. Scaling bars in 2.5a-d are 1 mm (left) and 100 μm (right).

The images in Figure 2.5b-d also show that increasing immersion rate *R* of the reaction solution into liquid nitrogen prior cryogelation decreases the spacing between the fibroin layers, i.e., the width of microchannels.

Figure 2.6a and b shows typical scanning electron micrographs of cross-sections of isotropic (a) and anisotropic cryogel scaffolds formed at $R$=30 mm.min$^{-1}$ (b).

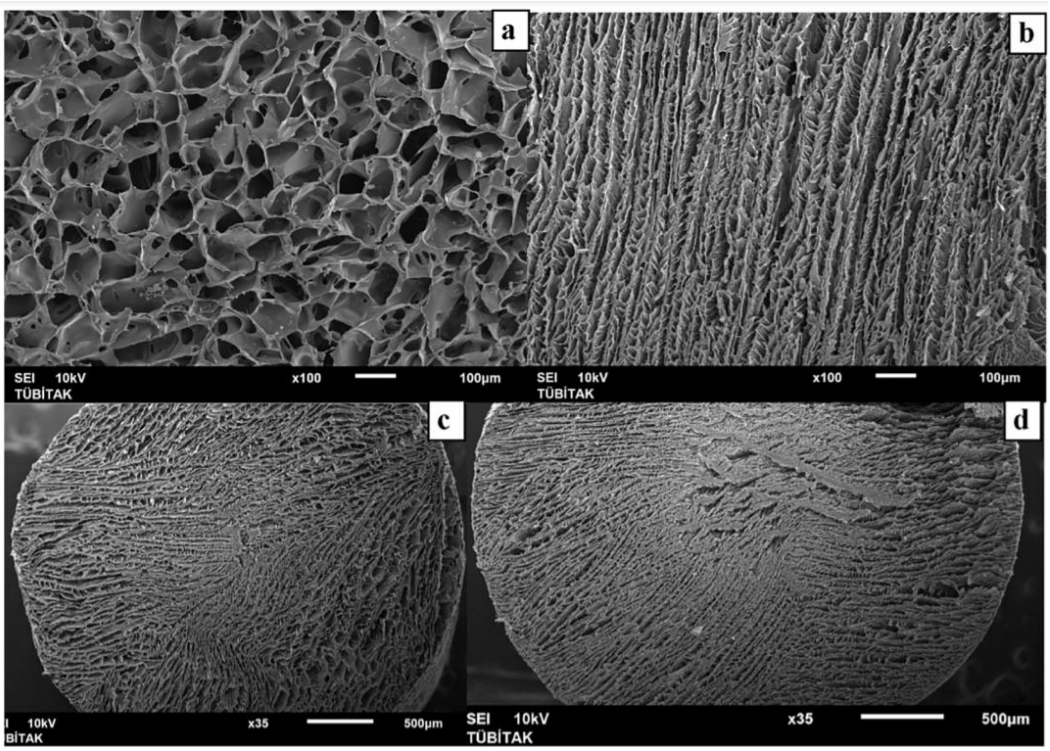


**Figure 2.6 :** SEM images of isotropic (a) and anisotropic cryogel scaffolds (b-d). Scaling bars are 100 µm (a,b) and 500 µm (c,d). $R$ = 20 (c), 25 (d), and 30 mm.min$^{-1}$ (b).

Isotropic cryogel sample consists of randomly oriented spherical and ovaloid pores of 30 ± 11 µm in diameter while the anisotropic sample possesses several hundred micrometers long, aligned fibroin layers producing a channel-like porous structure. The fibroin layers are interconnected by perpendicularly oriented branches to form a "fishbone" morphology. We have to mention that all the SEM and optical images presented here are cross-sectional views of the scaffolds and therefore, the aligned layers and channels are perpendicularly oriented to the immersion direction. For instance, Figure 2.6c and d showing SEM images of the cryogels formed at $R$ = 20 and 25 mm.min$^{-1}$, respectively, at a low magnification reveals radially oriented pore structure of the scaffolds. These results suggest that the growth of ice crystals occurs from the surface of the syringes which is in conduct with the cooling liquid at -196 °C

to its interior rather than in the direction in which the syringe is lowered into liquid nitrogen. A similar observation was recently reported by Arrua and Hilder in the preparation of cross-linked polyacrylates by directional freezing and photoinitiated cryocopolymerization [62]. We attribute the directional freezing in radial direction to the higher effective thermal conductivity in radial direction as compared to the longitudinal (immersion) direction because the heat flux must travel a shorter path in the former direction.

Figure 2.7 shows a scheme representing the unidirectional growth of ice crystals and formation of fibroin layers interconnected by branches. The temperature gradient in the fibroin solution induced by the contact with liquid nitrogen results in growing of ice from the surface of the cylindrical reactor toward the center. As water freezes, fibroin molecules together with BDDE cross-linker and TEMED are expelled from the formed ice crystals and accumulate around the growing crystals to form unfrozen domains of the reaction system. Thus, in addition of the temperature gradient, a concentration gradient is established across the moving freezing front due to the cryo-concentration of the reactants. This causes Mullins-Sekerka instability leading to the collapse of the moving freezing front leaving behind pockets of unfrozen concentrated fibroin solution [30,31,81].

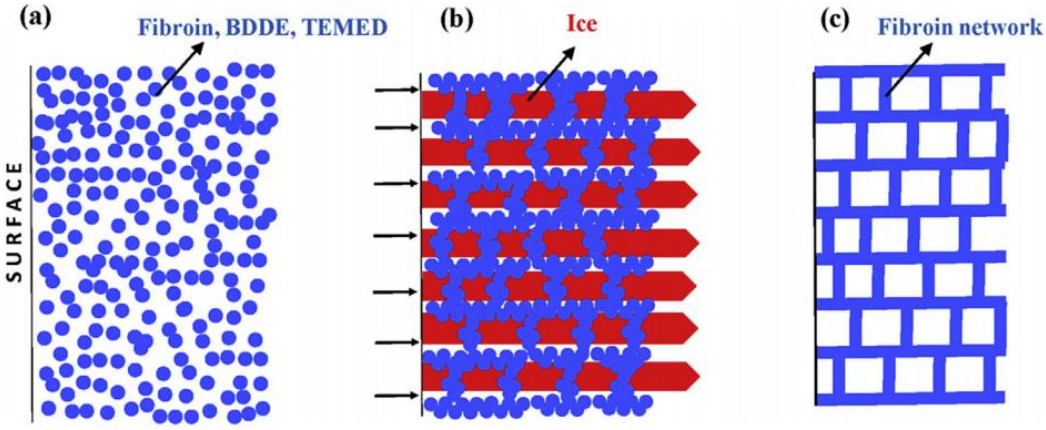


**Figure 2.7 :** Cartoon representing formation of aligned porous structure in fibroin cryogels under directional freezing. Fibroin solution before (a) and after directional freezing (b), and after cryogelation (c) is presented.

After the cryogelation reactions at -18 °C, the cryo-concentrated unfrozen fibroin solution between the aligned ice crystals turns to a dense gel making the fibroin layers and branches while ice act as template to form pores after thawing and freeze-drying. The primary periodicity of the aligned porous structures is defined by the Mulling-

Sekerka instability wavelength [81]. This wavelength is determined by competition between the destabilizing solute interfacial concentration gradient and the stabilizing effects acting to preserve the planarity of the interface, e.g., the imposed temperature gradient and surface energy of the solid/liquid interface [81]. The layer spacing, i.e., the channel diameter of 14 ± 7 μm in Figure 2.6b well compares with the instability wavelength of 15 μm for aqueous PVA solutions [31].

The results also show that the spacing between the fibroin layers strongly depends on the immersion rate *R*. Figure 2.8 showing SEM images of fibroin scaffolds formed at various *R* between 2.5 and 35 mm.min$^{-1}$ indicate that the layer spacing is inversely proportional to the immersion rate.

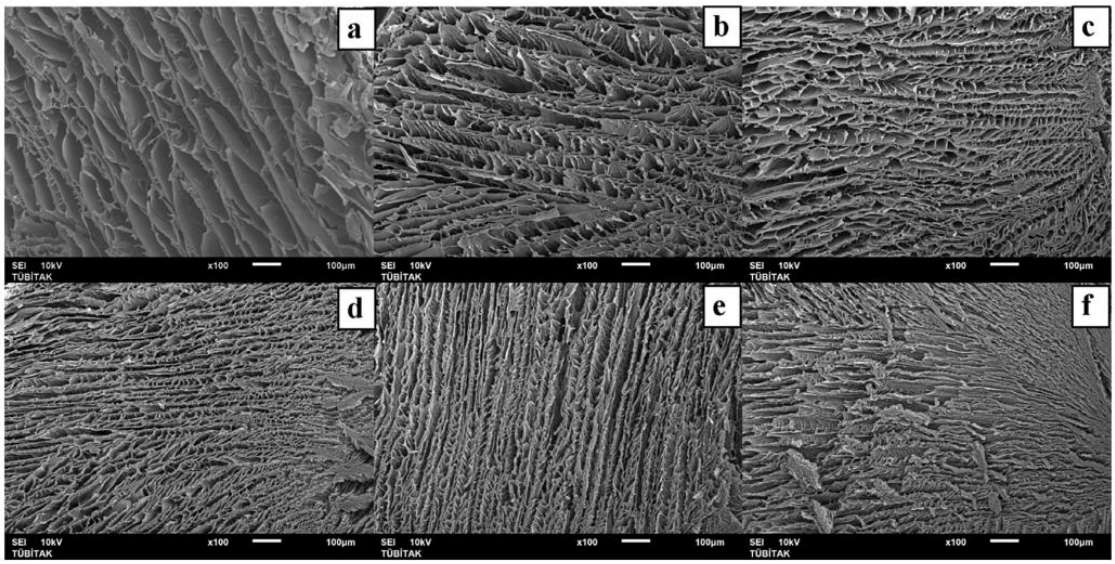


**Figure 2.8 :** SEM images of anisotropic cryogel scaffolds. *R* = 2.5 (a), 10 (b), 20 (c), 25 (d), 30 (e), and 35 mm.min$^{-1}$ (f). Scaling bars = 100 μm (Magnification = x100).

The average spacing between the layers were calculated by analyzing SEM images at various magnifications. The results are collected in Figure 2.3b where the layer spacing is plotted against *R*. At low immersion rates *R*, the layer spacing approaches to 70 μm with a broad length distribution while at $R > 20$ mm.min$^{-1}$, it is rather uniform and around 15 μm. Decreasing layer spacing with increasing immersion rate is due to the simultaneous increase of the freezing rate leading to the formation of a larger number of growing ice crystals [55]. Some internal microcracks were also observed in the cryogel samples formed at high immersion rates (≥25 mm.min$^{-1}$) which we attribute to rapid cooling of the fibroin solution (Figure 2.9).

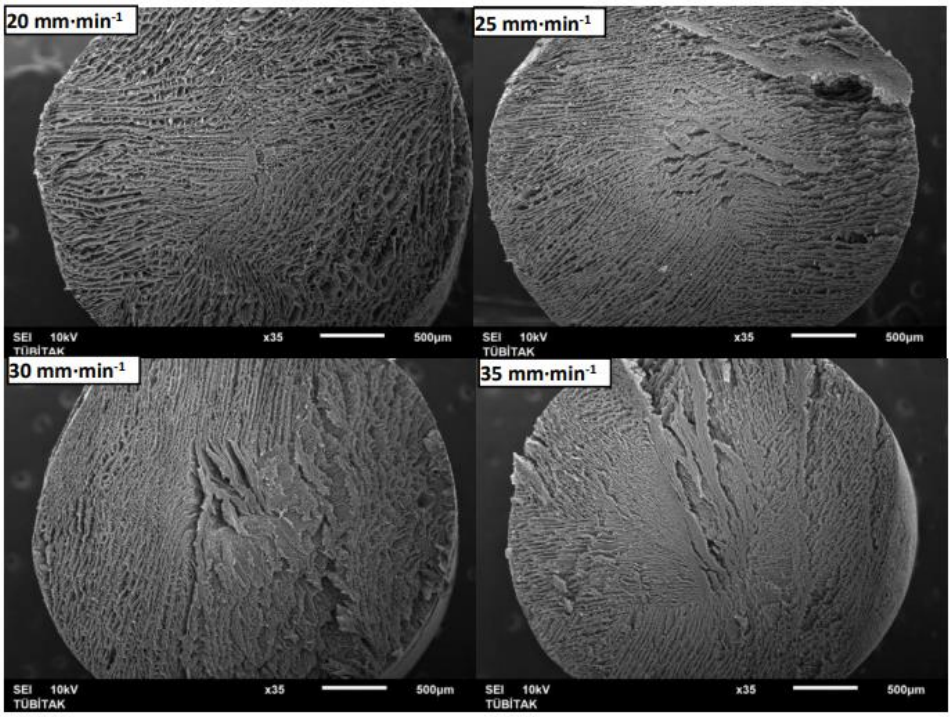


**Figure 2.9 :** SEM images of anisotropic cryogel scaffolds formed at various *R* indicated. Scaling bars are 500 μm.

Anisotropic microstructure of the cryogels resulted in anisotropic mechanical properties, as demonstrated by uniaxial compression tests. The tests were performed by cutting dry and swollen cryogel specimens from the directions parallel and vertical to the freezing direction and compressing them at a constant speed up to complete compression. Figure 2.10 shows stress-strain curves of the cryogel scaffolds formed at various *R* where the nominal stress $\sigma_{nom}$ is plotted against the deformation $\varepsilon$. Note that the curves were corrected by considering the onset of microcracks in true stress $\sigma_{true}$ - $\varepsilon$ plots as detailed in the experimental section and in Figure 2.1c. Solid and dashed curves represent the results of the measurements along the directions parallel and vertical to the freezing direction, respectively. The insets show the portion of the curves below $\sigma_{nom}$ = 0.6 MPa. The cryogels sustain up to ~90% compression at ~20 MPa compressive stresses. This extraordinary mechanical strength is due to the cryo-concentration of fibroin producing dense pore walls of high fibroin concentration [55,56]. For instance, freezing of an aqueous 6 wt% fibroin at -18 °C results in a frozen system composed of 88% ice and the rest being a concentrated unfrozen solution containing 37 wt% fibroin, which is about 6-fold larger than the nominal fibroin concentration [78]. Figure 2.10 also shows that, at below $R$ = 30 mm.min$^{-1}$, the initial slope of stress-strain curves corresponding to the Young's modulus $E$ is higher in

parallel direction as compared to the vertical direction. Another point is the appearance of a near-plateau regime at around 5% compression in parallel direction during which the scaffolds easily deform under force. As reported before [78], the appearance of a plateau regime indicates that the porous structure is mechanically stable up to the onset of the plateau while it starts to collapse with the onset of the plateau. The results reveal higher mechanical stability of 3D porous structure during compression in parallel direction as compared vertical direction.

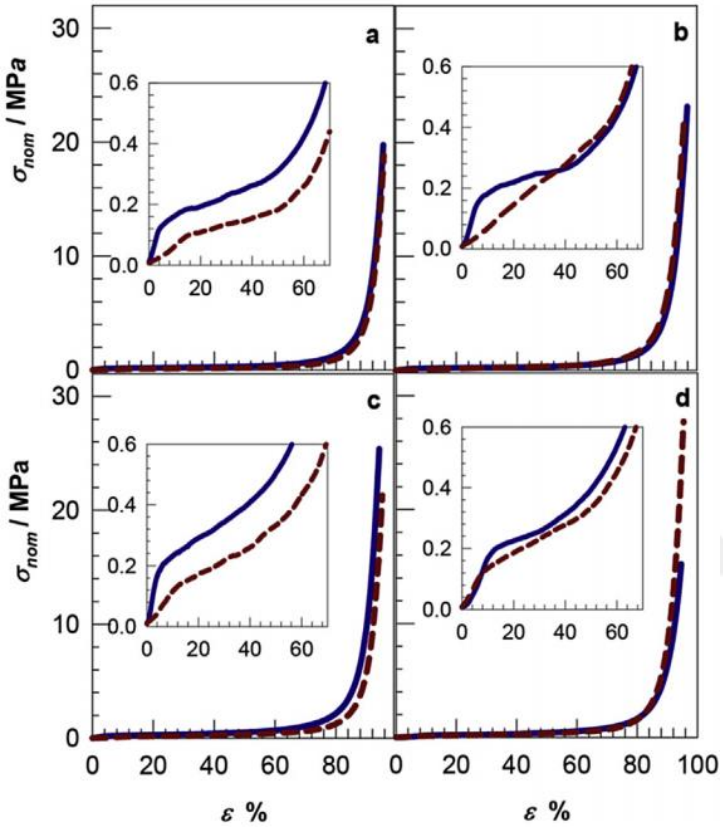


**Figure 2.10 :** Stress - strain curves of fibroin scaffolds as the dependence of the nominal stress $\sigma_{nom}$ on the compressive strain $\varepsilon$. The measurements were conducted parallel (solid curves) and vertical to the freezing direction (dashed curves). Immersion rate $R$ = 10 (a), 15 (b), 20 (c), and 30 mm.min$^{-1}$ (d).

The mechanical properties of the cryogels are compiled in Figure 2.11 where the Young's modulus $E$, compressive $\sigma_{comp}$ and fracture stresses $\sigma_f$ of dry (left panel) and swollen cryogels (right panel) are plotted against the immersion rate $R$. The circles and triangles represent the data obtained from parallel and vertical directions, respectively. Moreover, the data of isotropic cryogels in both directions shown at $R$ = 0 are presented by the filled and open squares. For both dry and swollen cryogel samples, the extent of anisotropy first increases with increasing immersion rate $R$ up to 20 mm.min$^{-1}$ and

then decreases again with a further increase in $R$. The modulus $E$ of scaffolds in parallel direction attains a maximum value of 3.4 ± 0.5 MPa at $R$ = 20 mm.min$^{-1}$, which is about four-fold larger than that measured in perpendicular direction (0.8 ± 0.3 MPa). Considering the Young's modulus of human cornea is around 3 and 1 MPa in horizontal and vertical directions, respectively [29], the results show that the cryogel scaffolds formed at 20 mm.min$^{-1}$ possess a comparable modulus.

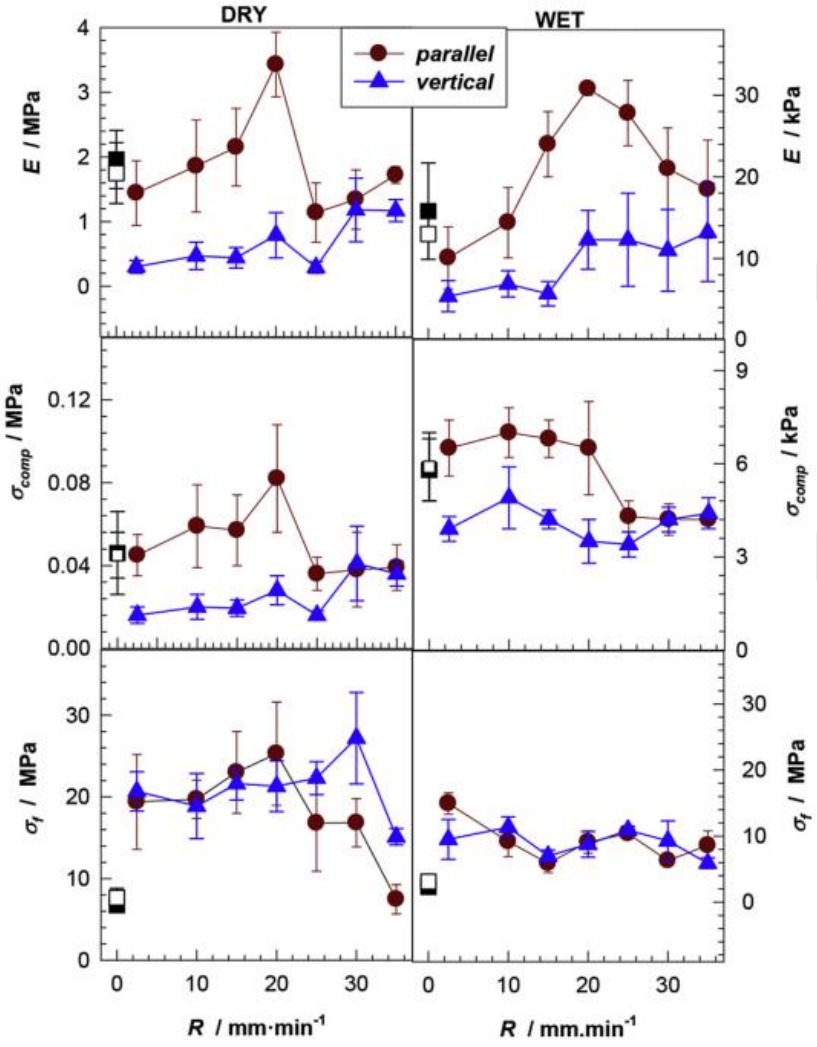


**Figure 2.11 :** The compressive modulus $E$, compressive $\sigma_{comp}$ and fracture stresses $\sigma_f$ of dry (left panel) and swollen cryogels (right panel) plotted against the immersion rate. The circles and triangles represent the data obtained from parallel and perpendicular directions, respectively, while the data of isotropic cryogels in both directions are shown by the filled and open squares.

The results also show that the anisotropic pore structure of the scaffolds mainly affect the initial part of the stress-strain curves represented by the modulus $E$ and the compressive stress $\sigma_{comp}$ at 3% compression while the ultimate properties such as the fracture stress $\sigma_f$ and fracture strain remain unaffected. This could be explained by

considering the microstructure of anisotropic cryogels (Figures 2.5, 2.6 and 2.8): Compressing in parallel to the freezing direction means vertically compressing several hundred nanometers long, radially oriented fibroin layers while, in vertical direction, the branches between the layers are compressed, which are only tens of nanometers. Thus, a much larger stress is initially required to compress the fibroin layers as compared to their branches. As the strain is increased, the porous structure starts to collapse resulting in a decrease of the channel width so that the stress required to deform the cryogel becomes independent of direction. The results also show that all anisotropic scaffolds formed at $R$ = 20 mm.min$^{-1}$ sustain at least 20 MPa compressive stresses as compared to 8 ± 1 MPa for the isotropic scaffold (Figure 2.11). The results of swollen cryogels shown in the right panel of Figure 2.11 reveals that the modulus, compressive and fracture stresses of the cryogels decrease by one order of magnitude after swelling in water.

The key advantage of the present directional freezing - cryogelation process is the shape and mechanical property recoverability of anisotropic cryogels subjected to complete compressions. This is presented in Figure 2.12a and b showing successive compression test results conducted up to about 99% compression. Here, the solid curves show stress-strain curves of cryogel samples prepared at $R$ = 20 mm.min$^{-1}$ as the dependences of the nominal $\sigma_{nom}$ and true stresses $\sigma_{true}$ on the compressive strain $\varepsilon$, respectively. The cryogel samples were compressed parallel (left panel) and vertical to the freezing direction (right panel). It is seen that, although the cryogel sample could completely be compressed, a maximum in $\sigma_{true}$ vs $\varepsilon$ plot appears at 95% compression suggesting the formation of microcracks in the sample. After this compression test, the cryogel sample remained in a compressed state due to squeezing out of water from its pores, as seen in the images in Figure 2.12c (c1/c3). After release of the piston, the compressed sample absorbs the released water (c3/c5) while adding water completely recovers its original dimension by sucking up water in its pores (c6), so that it can be subjected to the next compression test. Dashed and dash-dot curves in Figure 2.12a and b represent 2nd to 4th compression test results, each conducted after adding water to the gel sample. The insets to the figures reveal a good superposition of the successive stress-strain curves demonstrating that the damage in the cryogel is self-healed upon removing the stress. The average compression at break and fracture stress of four successive tests are 94 ± 1% and 8.4 ± 1.4 MPa, respectively. Similar results

were also obtained for isotropic and anisotropic cryogels formed at various immersion rates. Thus, all fibroin cryogels can be compressed up to about 99% strain without any permanent failure.

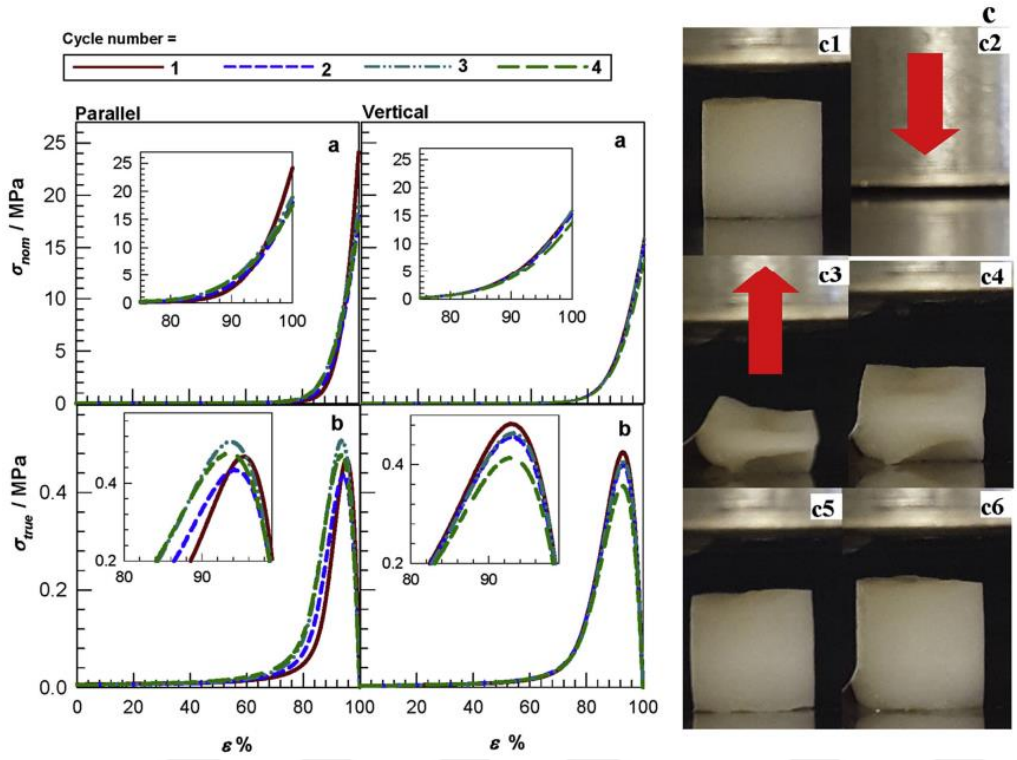


**Figure 2.12 :** (a, b) Four successive compression test results conducted on anisotropic cryogel samples up to around 99% compression where $\sigma_{nom}$ (a) and $\sigma_{true}$ (b) are plotted against the strain $\varepsilon$. The gel samples were prepared parallel (left) and perpendicular to the freezing direction (right). $R$ = 20 mm.min$^{-1}$. (c) Images showing the initial dimension of the cryogel sample (c1), its compressed state (c2), and the recovery of the initial dimension after release of the piston (c2/c5), and after adding water (c6).

## 2.3 Conclusion

Silk fibroin cryogels and scaffolds with anisotropic microstructures and anisotropic mechanical properties could be obtained by a combined directional freezing - cryogelation technique starting from aqueous 4.2 wt% fibroin solutions containing BDDE crosslinker and TEMED. In the first step, the reactor containing the aqueous solution of fibroin, cross-linker, and TEMED was immersed into liquid nitrogen at a controlled rate to create a directionally frozen ice template. In the second step, the cryogelation reactions were conducted in this frozen solution at -18 °C whereby the cryoconcentrated fibroin in the unfrozen microzones of the reaction system forms a 3D fibroin network. The scaffolds exhibit a Young's modulus in the range of MPa and

sustain up to 20 MPa compressive stresses. In addition to high mechanical strength, they also exhibit anisotropic microstructure and hence anisotropic mechanical properties, e.g., the Young's modulus is 3.4 ± 0.5 MPa and 0.8 ± 0.3 MPa when measured along the directions parallel and vertical to the freezing direction, respectively. All the cryogels could completely be compressed due to squeezing out of water from their pores. Upon removal of the load, the compressed cryogels immediately recover their original dimensions and mechanical properties by absorbing the released water into their pores. Because many biological tissues possess anisotropic hierarchical morphologies, high-strength anisotropic fibroin cryogels and scaffolds presented here have a broad range of potential applications in tissue engineering, bioseparation, microfluidics, and organic electronics.

## 3. HIGH-STRENGTH AND SELF-RECOVERABLE SILK FIBROIN CRYOGELS WITH ANISOTROPIC SWELLING AND MECHANICAL PROPERTIES[2]

Hydrogels as soft and smart materials have important functions in a variety of biological and biomedical applications [82]. Significant progress has been made in the past decade in the development of mechanically strong and tough hydrogels with mechanical performances approaching those of biological systems [15]. The next important challenge to be addressed in the gel science is to create anisotropic microstructures and mechanical properties in high-strength hydrogels as observed in many tissues such as skin, muscle, and articular cartilage [83]. To evaluate the degree of mechanical anisotropy in natural and synthetic materials, one may measure a mechanical parameter such as the Young's modulus $E$ in the directions parallel (∥) and perpendicular (⊥) to the orientation direction of the materials, and the ratio $E_{\parallel}/E_{\perp}$ is referred to as the "modulus anisotropy" [83]. For instance, tendon, the connective tissue joining muscle to bone has a compressive $E_{\parallel}/E_{\perp}$ ratio of around 20 [26], whereas human annulus fibrosus of intervertebral disk exhibits tensile circumferential moduli of 17.4 and 5.6 MPa at outer and inner sites, respectively, corresponding to $E_{\parallel}/E_{\perp}$ = 3.1 [84].

To create hydrogels with anisotropic microstructure and mechanical properties, several techniques have been developed such as stress induced orientation, directional freezing, and self-assembly [30-40,59,83,85-87]. Hydrogels containing oriented clay nanotubes or fibrils exhibit modulus anisotropy $E_{\parallel}/E_{\perp}$ of 3.0 and 7.0, respectively [86,87]. Modulus anisotropies between 2 and 4 were also reported in polyvinyl alcohol and double network hydrogels [32,38]. To our knowledge, the highest modulus anisotropy reported so far is 10.4, which was observed in polyacrylic acid hydrogels prepared by directional ice-crystal growing and subsequent polymerization [59]. These

[2] This chapter is based on the paper "Yetiskin, B., & Okay, O. (2019). High-strength and self-recoverable silk fibroin cryogels with anisotropic swelling and mechanical properties. *Int. J. Biol. Macromol.*, *122*, 1279-1289."

hydrogels are however mechanically weak, i.e., their moduli $E_{\parallel}$ and $E_{\perp}$ are 80.5 and 7.7 kPa, respectively. The utilization of anisotropic scaffolds as a biomaterial in tissue engineering applications should exhibit a modulus in the order of MPa to protect their integrity.

Silk fibroin is a promising and popular biomaterial due to its impressive biocompatibility, tunable biodegradability, outstanding thermomechanical stability, ease of processability, and remarkable mechanical properties [23,64-66]. Preparation of fibroin scaffolds with anisotropic mechanical properties is important in tissue engineering and bioseparation [60,88]. Anisotropic fibroin scaffolds were fabricated by directional freezing of aqueous fibroin solutions followed by freeze-drying to fix the oriented microstructure [53,54,89]. To render the scaffolds water-insoluble, they were then treated with methanol to induce the β-sheet formation. Although such scaffolds exhibit a high modulus anisotropy (up to 14), their Young's moduli are below kPa level, i.e., $E_{\parallel}$ = 0.28 kPa, and $E_{\perp}$ = 0.02 kPa [53].

We recently reported an alternative strategy to create anisotropic fibroin scaffolds by combining directional freezing and cryogelation of aqueous fibroin solutions [90]. Cryogelation is a simple technique that provides formation of macroporous gels below the freezing point of the gelation solution [55,56]. We have to mention that cryogelation and freezing/thawing are different techniques with respect to the formation mechanism and mechanical properties of polymeric scaffolds [55,56]. During cryogelation, the reactions occur in the unfrozen domains of the apparently frozen system occupying about 5% of the whole volume. Thus, the reactants such as fibroin are cryo-concentrated in these unfrozen domains where the gelation reactions proceed. The pore wall produced by cryogelation is a dense polymeric gel because of the cryoconcentrated fibroin solution around the ice crystals. In contrast, the pore wall formed after freezing/thawing of a conventional gel is a loosely crosslinked gel due to the absence of cryoconcentration. As a consequence, the porous structures produced during cryogelation are much stronger than those formed during freezing/thawing. For instance, Young's moduli of fibroin scaffolds formed via cryogelation and freezing/thawing of 4.2 wt% fibroin solutions are 8 ± 1 and 1.0 ± 0.3 MPa, respectively, highlighting the effect of cryoconcentration on the scaffold properties [78]. Moreover, cryogels can be squeezed almost completely without any crack

propagation making them one of the toughest materials so far reported. We recently fabricated anisotropic silk fibroin scaffolds by immersing the reactor containing fibroin solution into a cold bath at a controlled rate followed by the cryogelation reactions [90]. By adjusting the immersion rate of the reactor into the cold bath, we were able to create anisotropic silk fibroin scaffolds with Young's moduli *E* in the range of MPa. However, their modulus anisotropy was below 4.3 due to the heat transfer to the reactor walls both in axial and radial directions [90].

Herein we report the preparation of silk fibroin scaffolds with a high degree of mechanical anisotropy similar to that of tendon together with a high mechanical strength and rapid self-recoverability. To prepare such hydrogels we designed a reactor consisting of a copper bottom plate and a cylindrical polytetrafluoroethylene (PTFE) mold exhibiting a thermal conductivity ratio of 1600 (Figure 3.1a). Copper bottom plate was immersed in a cold bath at -30 or -196 °C, whereas the cylindrical PTFE mold locating outside of the cold bath was filled with aqueous solutions of silk fibroin of various concentrations together with butanediol diglycidyl ether (BDDE) and *N,N,N′,N′*-tetramethylethylenediamine (TEMED) as a crosslinker and pH regulator, respectively [71,78,91]. Unidirectional frozen fibroin solution was then subjected to cryogelation at -18 °C to induce a conformational transition in fibroin from random coil to β-sheet structures and hence water stability [71]. As will be seen below, we were able to create mechanically strong silk fibroin scaffolds exhibiting microstructural, swelling and mechanical anisotropies. The scaffolds exhibit the highest modulus anisotropy so far reported, 21 ± 5, with moduli $E = 2.3 \pm 0.5$ and 0.11 ± 0.03 MPa measured along parallel and perpendicular to the freezing direction, respectively. We also demonstrate that, independent on the fibroin concentration or direction of the measurements, 60% of the mechanical energy given to the cryogels are dissipated due to the friction between the fibroin pore walls, which is responsible for their squeezability and self-recoverability.

## 3.1 Experimental

### 3.1.1 Materials

Butanediol diglycidyl ether (BDDE, Sigma Aldrich), *N,N,N′,N′*-tetramethylethylenediamine (TEMED, Sigma Aldrich), LiBr (Merck), and $Na_2CO_3$

(Merck) were used without further purification. Silk fibroin (SF) was isolated from *Bombyx mori* cocoons (Kozabirlik, Turkey) as described before [67]. Briefly, cocoons were first boiled in aqueous solution of 0.02 M $Na_2CO_3$ for 1 h to remove sericin followed by rinsing the remaining SF with water at 70 °C. After dissolving SF in aqueous solution of 9.3 M LiBr at 60 °C for 2 h, the solution was dialyzed using a 10000 MWCO dialysis tubing (Snake Skin, Pierce) for 3 days against water that was changed three times a day. After centrifugation, the final SF concentration was ~5 wt%, which was determined by weighing the remaining solid after drying. Aqueous solutions with a higher SF concentration were prepared by concentrating 5 wt% SF solution via dialysis against aqueous solutions of 10 and 15 w/v% poly(ethylene glycol) (PEG, Sigma-Aldrich, molecular weight: ~10000 $g.mol^{-1}$) using 3500 MWCO dialysis tubing (Snake Skin, Pierce). All SF solutions were stored at 4 °C and used within 2 weeks.

### 3.1.2 Preparation of anisotropic fibroin cryogels

Fibroin cryogels were prepared from aqueous solutions of fibroin at various concentrations $C_{SF}$ in the presence of BDDE (20 mmol epoxide groups per gram of fibroin) and TEMED (0.25 v/v%). At $C_{SF}$ = 16.7 wt%, BDDE concentration was decreased to 10 $mmol.g^{-1}$ to prevent early gelation. As detailed before [71,78], BDDE acts as a cross linker to induce conformational transition in fibroin while TEMED is a pH regulator accelerating this transition. We have to note that gelation of aqueous fibroin solutions was studied before at various pH's between 6 and 11, which was adjusted by the addition of TEMED as a pH regulator [71]. The reactions between the amino groups on silk fibroin and the diepoxide crosslinker was found to be very fast and the resulting gels were mechanically strong in the presence of 0.25 v/v% TEMED producing a pH in the reaction solution of 10.2. We fixed this pH value together with the type of the pH-regulator throughout this study.

Typically, to obtain cryogels at $C_{SF}$ = 4.2 wt%, BDDE (0.50 mL) and TEMED (15 μL) were added to 5 mL of 5 wt% SF solution followed by adjusting the final volume to 6 mL with water. The homogeneous solution was then pipetted into a cylindrical polytetrafluoroethylene (PTFE) mold of 12 mm in internal diameter fitted with a copper bottom plate, as schematically shown in Figure 3.1a. Preliminary experiments showed that the diameter of PTFE mold is also critical because thinner molds resulted

in the formation of randomly distributed pores (Figure 3.2). To further reduce the heat transfer in radial direction, a polypropylene (PP) pipe was placed around the PTFE mold and the copper part of the system was then immersed in a cold bath until the reaction system completely freezes which required around 30-45 min.

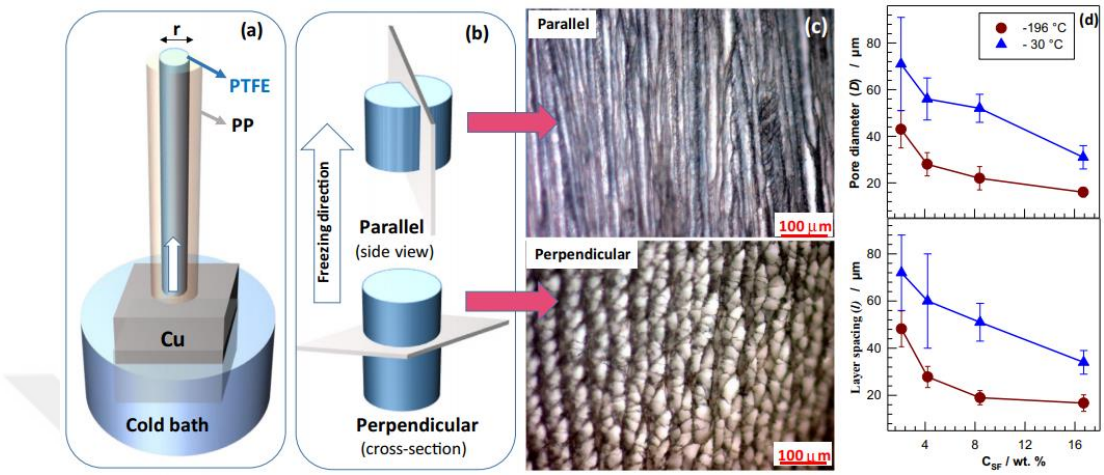


**Figure 3.1 :** (a): Experimental setup for the preparation of anisotropic fibroin cryogels. (b): Directions parallel and perpendicular to the freezing direction indicated by the white arrow. (c) Optical microscopy images of fibroin cryogels taken parallel and perpendicular to the freezing direction. $C_{SF}$ = 4.2 wt%. (d) Average pore diameter $D$ and layer spacing $l$ for cryogels prepared by freezing at -196 °C (circles) and -30 °C (triangles) plotted against the fibroin concentration $C_{SF}$.

Liquid nitrogen (-196 °C) and ethylene glycol/water mixture at equal volume ratio (-30 °C) were used as the cold bath in our experiments. Because the thermal conductivity of copper is 1600-fold larger than that of PTFE, freezing of the solution occurs in bottom-up direction. The reactor was then removed from the cold bath and placed in a cryostat at -18 °C to carry out the cryogelation reactions for 1 day. The gel specimens after preparation were thawed at 24 °C for 30 min and then immersed in excess of water for one week by refreshing water several times to extract any soluble species. The equilibrium swollen gel samples were taken out of water and freeze-dried to constant weight.

### 3.1.3 Characterization of fibroin cryogels

Swelling and gel fraction measurements as well as the conformational analysis of fibroin in the cryogels were carried out as reported before [91]. In short, the frozen cryogel specimens after preparation were first thawed at 24 °C for 30 min and then immersed in a large excess of water for one week by replacing water several times to extract any soluble species. The swelling equilibrium was tested by weighing the gel

samples as well as by measuring the lengths of the gel samples in directions parallel and perpendicular to the freezing direction using a calibrated digital compass (Mitutoyo Digimatic Caliper, Series 500, resolution: 0.01 mm). The equilibrium swollen gel samples were taken out of water and immediately frozen at -25 °C for 1 day before being freeze-dried at -40 °C/0.12 mbar for 1 day and -60 °C/0.011 mbar for an additional 1 day. The freeze-drying system consisted of a freeze-dryer (Christ Alpha 2-4 LD plus) connected to a vacuum pump (Vacuubrand RZ 6). The pressure during freeze-drying was adjusted using a valve controller and monitored by an active digital controller. All cryogel samples were freeze-dried under the same conditions. The equilibrium weight swelling ratio $q_w$ was calculated as $q_w = m_{swl}/m_{dry}$, where $m_{swl}$ and $m_{dry}$ are the masses of the equilibrium swollen and dried gel samples, respectively. The volume swelling ratio of the samples was calculated as described in the text. The gel fraction $W_g$, that is, the conversion of fibroin to the 3D fibroin network (mass of water-insoluble fibroin / initial mass of the fibroin in the feed) was calculated from the masses of dry fibroin network and from the fibroin in the feed.

Differential scanning calorimetry (DSC) measurements were conducted on a Perkin Elmer Diamond DSC under a nitrogen atmosphere. The cryogel samples equilibrium swollen in water were cut into specimens of about 10 mg wet weight and sealed in aluminum pans. They were then scanned between -50 and 250 °C with heating/cooling rates of 5 and 10 °C.min$^{-1}$. Thermal gravimetric analysis was conducted on a Labsys evo SETARAM system under nitrogen by heating from 20 to 500 °C at a rate of 10°C. min$^{-1}$.

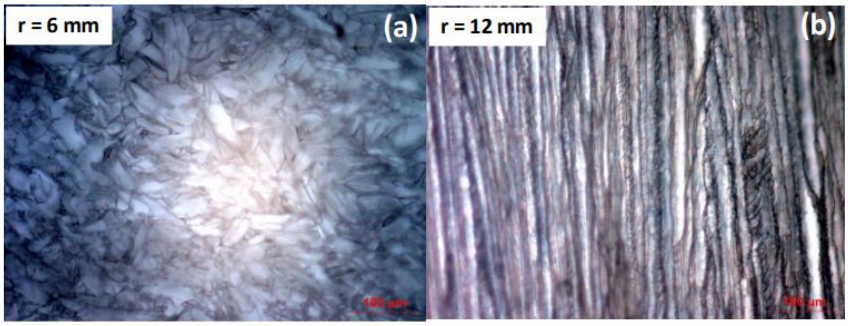


**Figure 3.2 :** Optical images of fibroin cryogels taken parallel to the freezing direction. The cryogels were synthesized in the reactor shown schematically in Figure 3.1a using PTFE pipe with an internal diameter *r* of 6 (a) and 12 mm (b). $C_{SF}$ = 4.2 wt. %. At *r* = 12 mm, aligned pore channels in freezing direction form while decreasing *r* to 6 mm results in the formation of randomly distributed pores. Scaling bar = 100 μm.

Rheological measurements were conducted on a Bohlin Gemini 150 rheometer system (Malvern Instruments, UK) equipped with a Peltier device for temperature control. The gel specimens equilibrium swollen in water were placed between the parallel plates (diameter, 20 mm) of the instrument. During all of the rheological tests, a solvent trap was used and the outside of the upper plate was covered with a thin layer of low-viscosity silicone oil to prevent evaporation of water. To investigate the microstructural anisotropy, cylindrical cryogel specimens after freeze-drying were cut in directions parallel and perpendicular to the freezing direction, as schematically illustrated in Figure 3.1b. The cut surfaces were then investigated using scanning electron microscopy (SEM) at various magnifications in a field emission scanning electron microscope (JEOL JSM-6510LV) after coating with gold for 3 min using a Sputter coater. The cut surfaces were also studied using an image analyzing system consisting of a microscope (XSZ single Zoom microscope), a CDD digital camera (TK 1381EG) and a PC with the data analyzing system Image-Pro Plus.

For the uniaxial compression tests, the cryogel specimens were cut into rectangular shapes (3.1 ± 0.4 × 2.9 ± 0.3 × 2.8 ± 0.4 mm) and compressed parallel and perpendicular to the freezing direction at a constant crosshead speed of 0.3 $mm.min^{-1}$. The tests were performed at 24 ± 2 °C on a Zwick Roell test machine using a 500 N load cell. Before the test, an initial compressive contact to 0.01 ± 0.002 N was applied to ensure a complete contact between the gel and the plates. Compressive stress was presented by its nominal $\sigma_{nom}$ and true values $\sigma_{true}$ ($=\lambda\sigma_{nom}$) which are the forces per cross-sectional area of the undeformed and deformed gel specimen, respectively, and $\lambda$ is the deformation ratio (deformed length/original length). The compressive strain $\varepsilon$ is defined as the change in the length of the gel specimen relative to its initial length, i.e., $\varepsilon = 1 - \lambda$. The Young's modulus $E$ was calculated from the slope of stress-strain curves between 2 and 4% compressions. The fracture nominal stress $\sigma_f$ and fracture strain $\varepsilon_f$ were calculated from the maxima in $\sigma_{true}$ - $\varepsilon$ plots, as detailed previously [90]. Cyclic mechanical tests were carried out with a compression step performed at a constant crosshead speed of 0.3 $mm.min^{-1}$ to maximum strain $\varepsilon_{max}$ (varied between 20 and 80%), followed by immediate retraction to zero displacement and a waiting time of 5 min, until the next cycle of compression. Note that uniaxial tensile tests could not be conducted on the cryogel specimens because they were too slippery.

Fourier-transform infrared (FTIR) spectra of the freeze-dried specimens were obtained using a single bounce diamond attenuated total refractance (ATR) module on a FTIR spectrometer (Nicolet Nexus 6700) equipped with a liquid nitrogen cooled mercury-cadmium-telluride (MCT) detector. The resolution of each spectrum was 4 $cm^{-1}$, and 64 interferograms were coadded in the range of 500 - 4000 $cm^{-1}$. The conformation of fibroin chains was estimated by analyzing the spectra using PeakFit software (Version 4.12, SeaSolve Software Inc.). Linear baseline correction was applied to the Amide I region (1580 - 1720 $cm^{-1}$) before the band was deconvolved by Gauss Amplitude function. For the curve fitting procedure, the initial band positions at 1620, 1640, 1660, and 1698 $cm^{-1}$ representing β-sheet, random coil, α-helix, and β-turn conformations, respectively, were fixed, allowing their widths and heights to vary [71,78,91].

### 3.2 Results and Discussion

#### 3.2.1 Microstructure of fibroin cryogels

The experimental setup shown schematically in Figure 3.1a provided formation of highly anisotropic silk fibroin (SF) cryogels. This could be achieved by use of the copper bottom plate of high conductivity preventing ice growth in the radial direction. Unidirectional freezing of the reaction system in liquid nitrogen (-196 °C) or ethylene glycol/ water mixture (-30 °C) followed by cryogelation at -18 °C resulted in SF cryogels containing pore channels aligned to the freezing direction. Figure 3.1c shows typical optical images of cryogel specimens prepared at a fibroin concentration $C_{SF}$ of 4.2 wt% using liquid nitrogen as the cold bath. The images were taken parallel and perpendicular to the freezing direction corresponding to the vertical section along the aligned fibroin channels and the cross-section of the channels, respectively. The parallel view shows long fibroin layers aligned to the freezing direction while the top view of the channels visualizes the micrometer-sized pores. The average pore diameter $D$ and spacing $l$ between fibroin layers were calculated from the optical images of cryogels formed at various fibroin concentrations $C_{SF}$ (Figure 3.3). Figure 3.1d shows the variations of $D$ and $l$ of cryogels prepared via pre-freezing at -30 and -196 °C plotted against fibroin concentration $C_{SF}$. Both the diameter of the pores and the spacing between fibroin layers corresponding to the width of pore channels decrease as $C_{SF}$ is increased. For instance, $D$ and $l$ of cryogels prepared using liquid nitrogen as a cold bath decrease from 43 ± 8 to 16 ± 2 μm and from 48 ± 8 to 17 ± 3 μm,

respectively, as $C_{SF}$ is increased from 2.1 to 16.7 wt%. Moreover, at low $C_{SF}$, cryogels have polydisperse pores as reflected in Figure 3.1d by large error bars whereas the pores become rather uniform as $C_{SF}$ is increased. The inverse relation between the pore diameter and $C_{SF}$ is likely due to the variation of the water content in the reaction solution. Increasing $C_{SF}$ decreases the amount of water developing the ice template in the solution leading to the formation of smaller pores and thinner pore channels. Figure 3.1d also shows that $D$ and $l$ increase by increasing the cold bath temperature from -196 to -30 °C.

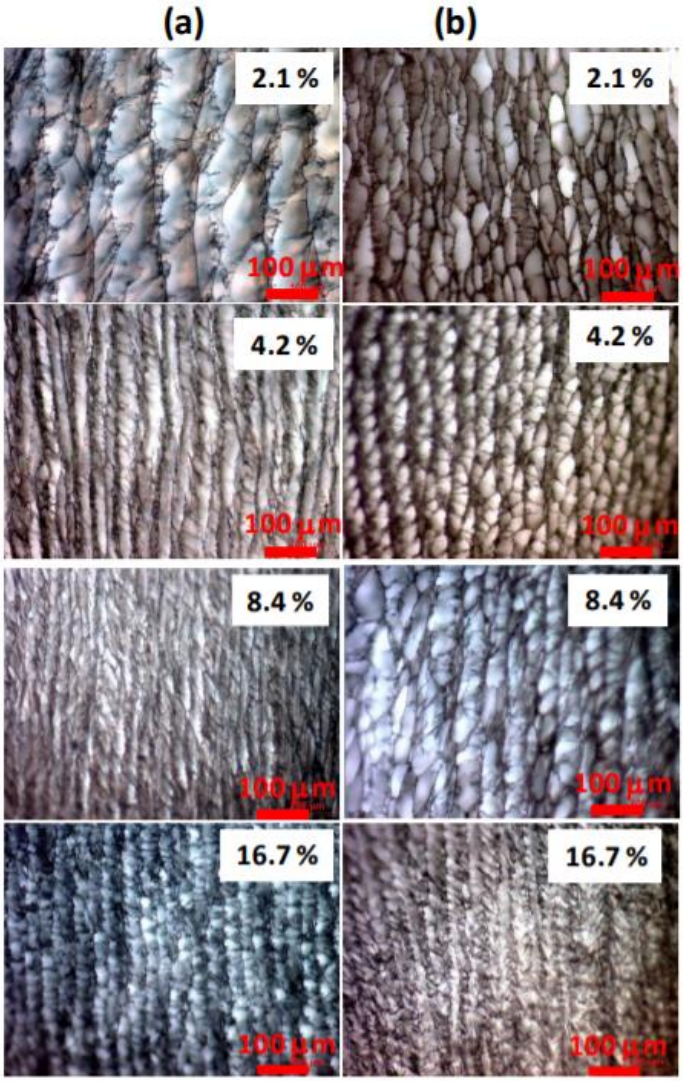


**Figure 3.3 :** Optical images of anisotropic cryogel samples taken parallel (a) and perpendicular to the freezing direction (b). Fibroin concentrations $C_{SF}$ (in wt %) are indicated. Scaling bars = 100 µm.

Figure 3.4a and b show typical scanning electron micrographs (SEMs) of cryogel scaffolds formed at various $C_{SF}$ between 2.1 and 16.7 wt% taken parallel and perpendicular to the freezing direction, respectively. At the lowest concentration of

fibroin used (2.1 wt%, left panel), the pores are not stable so that they sandwiched between the fibroin layers whereas at higher concentrations the cryogels possess several hundred micrometers long, aligned fibroin layers interconnected by vertically oriented branches producing a channel-like porous structure.

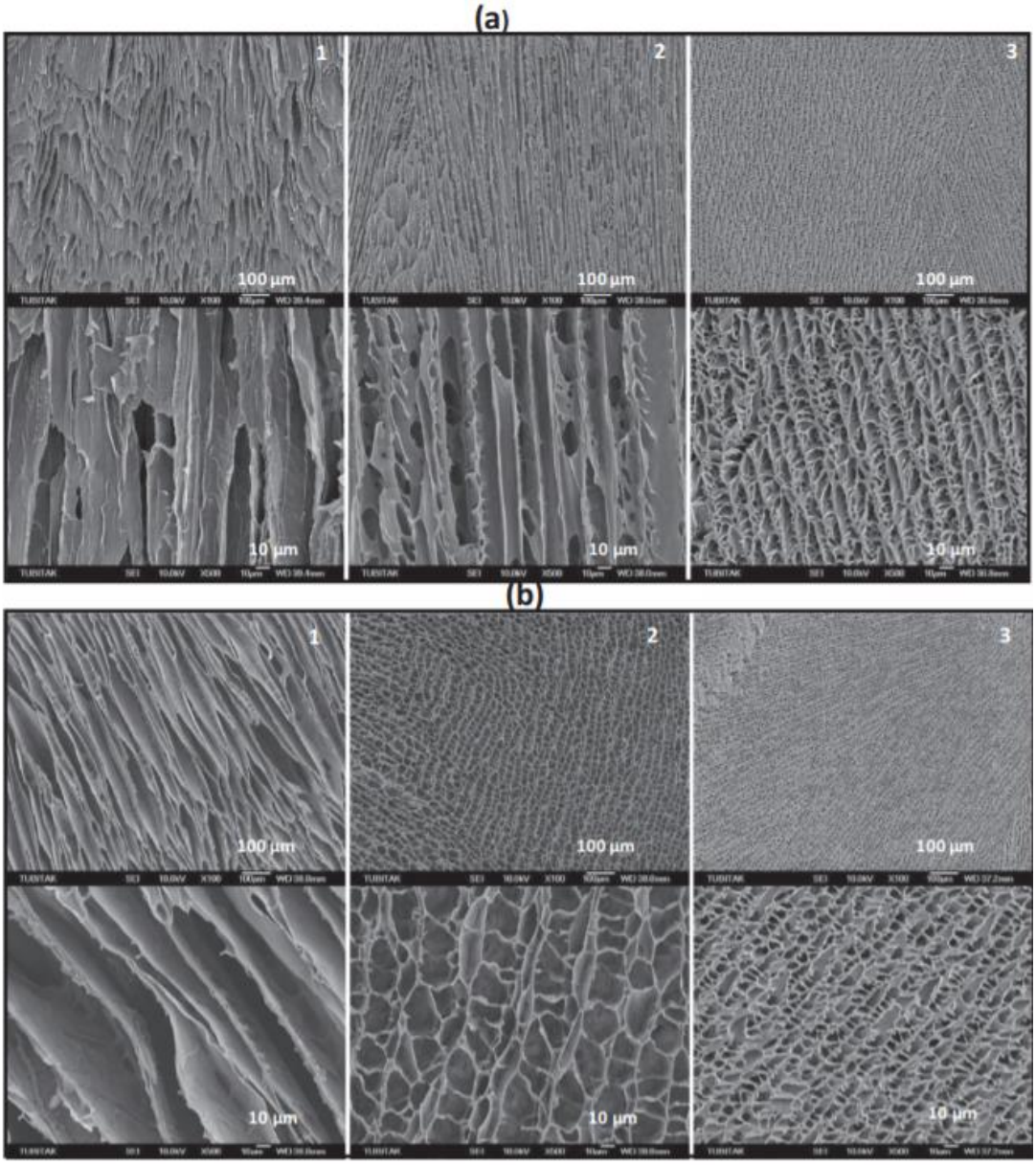


**Figure 3.4 :** SEM images of cryogel scaffolds formed at $C_{SF}$ = 2.1 (1), 4.2 (2), and 16.7 wt% (3). The images were taken parallel (a) and perpendicular to the freezing direction (b). Scaling bars are100 µm (upper panel) and 10 µm (bottom panel).

In accord with Figure 3.1d, increasing the fibroin concentration $C_{SF}$ decreases the size of the pores as well as the spacing between the fibroin layers. Figure 3.5a, b show SEM images of cryogel scaffolds formed at $C_{SF}$ = 8.4 wt% via freezing at -196 (a) and -30 °C (b). The images were taken perpendicular to the freezing direction. It is seen that

the freezing temperature has an important effect on the pore size. In line with the results obtained from the optical images (Figure 3.1d), both the pore diameter and layer spacing increase with increasing temperature of the cold bath. Because the rate of freezing of the reaction solution decreases with increasing cold bath temperature, fewer but larger ice crystals will grow during freezing at a high temperature leading to larger pores [55]. As will be discussed later, cryogels formed via freezing at -30 °C exhibit poor mechanical properties as compared to those at -196 °C. Therefore, in the following, we will mainly discuss the properties of cryogels prepared via prefreezing at -196 °C.

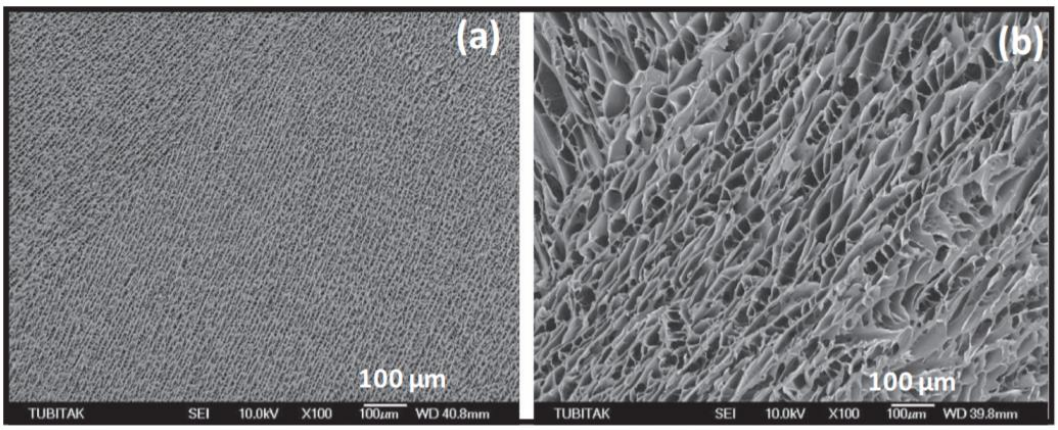


**Figure 3.5 :** SEM images of cryogel scaffolds formed via freezing at -196 (a) and -30 °C (b). $C_{SF}$ = 8.4 wt%. The images were taken perpendicular to the freezing direction.

### 3.2.2 Water stability of cryogels and possible cryogelation mechanism

All the cryogels were insoluble in water with a gel fraction close to unity revealing that fibroin molecules are completely incorporated into 3D fibroin network. Thermogravimetric analysis (TGA) of freeze-dried gel specimens revealed a weight loss of 5 to 7% at around 95-100 °C due to evaporation of bound water and a peak at 315 °C due to thermal degradation of SF (Figure 3.6). DSC scans also show a broad endothermic peak below 100 °C that disappeared after annealing from -50 to 250 °C indicating the existence of bound water in freeze-dried cryogel specimens (Figure 3.7).

Water-insolubility of the cryogels suggests formation of β-sheets acting as crosslinks by connecting the fibroin chains to a 3D network. FTIR measurements were conducted on freeze-dried fibroin scaffolds to estimate the conformation of SF in the cryogels. Figure 3.8a shows amide I region of FTIR spectra of SF before (dashed curve) and after cryogelation (blue symbols). A peak at 1640 $cm^{-1}$ appears before gelation which

is typical for random-coil conformation. This peak shifts to 1620 $cm^{-1}$ and two additional minor peaks at 1660 and 1698 $cm^{-1}$ appear after cryogelation which are attributed to β-sheet, α-helix and β-turn conformations [74,75].

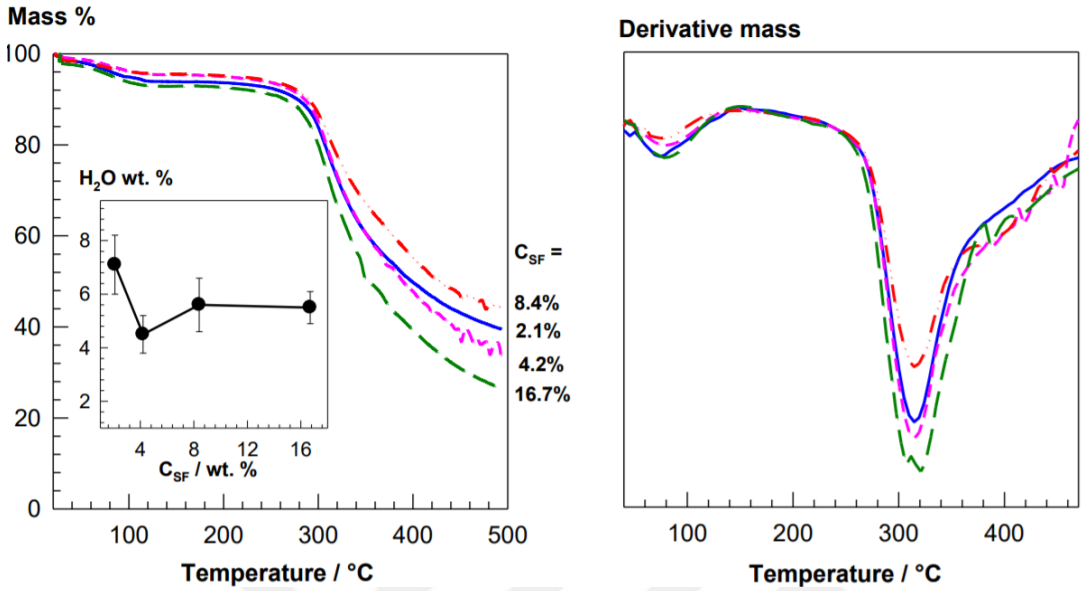


**Figure 3.6 :** Thermogravimetric analysis (TGA) curves of anisotropic cryogel samples. The inset shows the water content of the cryogels plotted against the fibroin concentration $C_{SF}$.

Fibroin conformation in the cryogels was estimated via peak separation of amide I band by selecting a Gaussian model for curve fitting [71,78]. The hidden peaks after peak separation shown in Figure 3.8a by thin gray curves with peak positions at 1620, 1640, 1660, and 1698 $cm^{-1}$, corresponding to β-sheet, random-coil, α-helix, and β-turn conformations, respectively, were used to estimate the conformation of fibroin network chains. Figure 3.8b shows conformations of fibroin in cryogels plotted against fibroin concentration $C_{SF}$, where the data at $C_{SF}$ = 0% correspond to fibroin before gelation. It is seen that the content of α-helix decreases in favor of the random coil and β-sheet contents and the fraction of β-sheets increases from 14 ± 3 to 32 ± 1% after cryogelation which is, within the limits of experimental error, independent of fibroin concentration.

Formation of water-insoluble fibroin scaffolds with an aligned porous structure can be explained using the following scenario: Upon immersion of the bottom part of the reactor into cold bath, ice crystals start to grow in down-to-up direction during which the solutes silk fibroin (SF), BDDE, and TEMED are expelled from the ice and they concentrate in the unfrozen domains of the reaction solution. This leads to the

formation of a highly concentrated solution of SF, BDDE, and TEMED surrounding the directionally growing ice crystals.

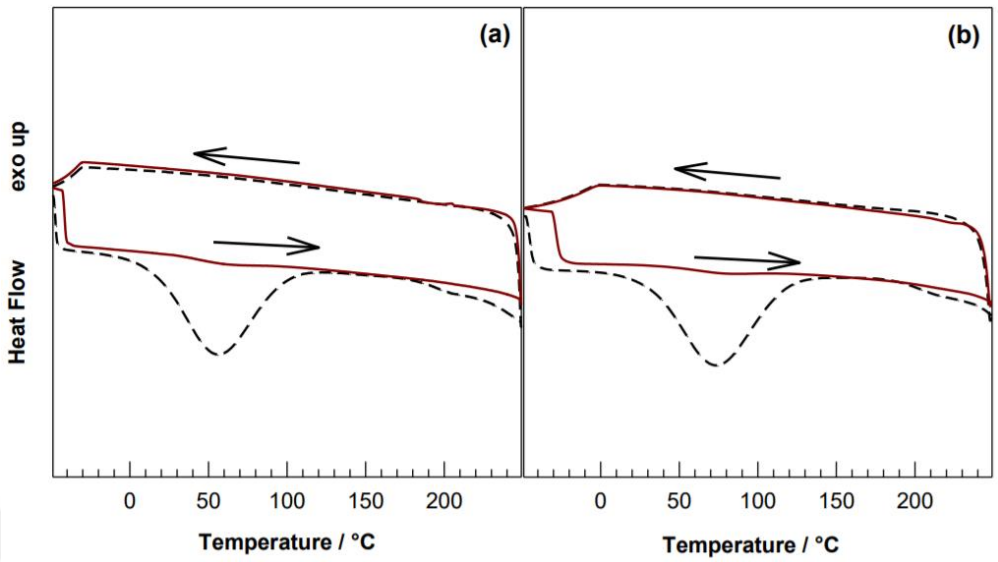


**Figure 3.7 :** DSC scans of anisotropic cryogel samples formed at $C_{SF}$ = 16.7 wt. % at a heating/cooling rate of 5 (a) and 10 °C.min$^{-1}$ (b). The 1st and 2nd runs are shown by dashed and solid curves, respectively.

After thermal equilibrium of the reaction system with the cold bath at -196 °C, the completely frozen system consists of two phases, namely frozen solution phase containing all the reactants, and pure ice crystal phase aligned to the freezing direction. Upon heating to -18 °C to conduct the cryogelation reactions, frozen solution phase containing all solutes will partially melt to attain thermal equilibrium with the cryostat temperature of -18 °C. It was reported that when an aqueous solution containing 6 wt% SF is cooled to -18 °C, at thermal equilibrium it consists of 88 wt% ice and the rest being an unfrozen solution containing 37 wt% fibroin [78]. This process, called cryoconcentration is due to the high solute concentration preventing the freezing of the whole system [55]. Thus, during the incubation period at -18 °C, cryogelation in unfrozen fibroin channels containing BDDE and TEMED leads to the formation of a 3D fibroin network filled with ice template forming pores after melting at room temperature. Previous work shows that the amine groups on fibroin molecules are responsible for the crosslinking reactions of fibroin with diepoxide crosslinkers such as BDDE [71]. Introduction of BDDE crosslinks between fibroin molecules decreases the mobility of the chains, which triggers the conformational transition from randomcoil to β-sheet structure and hence fibroin gelation [71,78]. The occurrence of gelation reactions at such a low temperature is due to the cryoconcentration

phenomenon producing a high concentration of reactants. Thus, decreasing the reaction rate due to low temperature is compensated by the increasing concentration of the reactants.

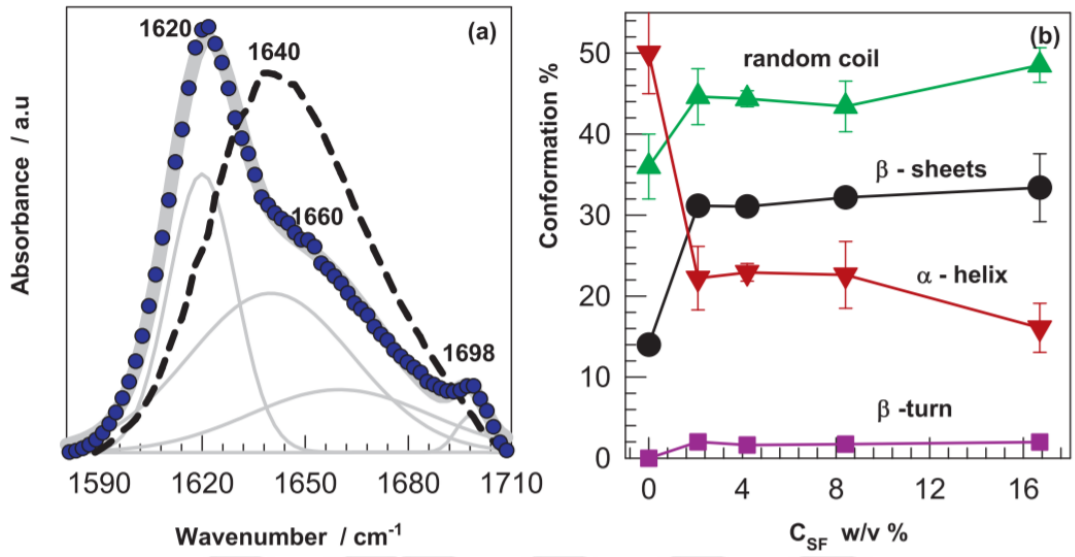


**Figure 3.8 :** Typical ATR-FTIR spectra of freeze-dried silk fibroin sample before (dashed curve) and after cryogelation at $C_{SF}$ = 8.4 wt% (filled blue circles). The result of curve fitting for the original spectrum after cryogelation is shown by the thick gray curve. The thin gray curves represent the hidden peaks after peak separation with peak positions at 1620, 1640, 1660, and 1698 $cm^{-1}$. (b): Fractions of random coil, β-sheet, α-helix and β-turn conformations in cryogels plotted against $C_{SF}$.

### 3.2.3 Swelling anisotropy and swollen state porosity of cryogels

To highlight the effect of the microstructural anisotropy on the swelling behavior of the cryogels, we conducted swelling measurements both parallel and perpendicular to the freezing direction. The degree of volume swelling was determined by measuring the lengths of the gel specimens in directions parallel $l_x$ and perpendicular to the freezing direction $l_y$. (Figure 3.9a). Volume swelling ratios in these directions denoted by $q_{v,x}$ and $q_{v,y}$, respectively, were calculated as $q_{v,x} = (l_x / l_{x,0})^3$ and $q_{v,y} = (l_y / l_{y,0})^3$ , where the subindex 0 denotes the initial sample length in dry state. Figure 3.9b compares $q_{v,x}$ and $q_{v,y}$ ratios of cryogels formed at various fibroin concentrations $C_{SF}$. All cryogels exhibit a larger degree of swelling in the x-direction, that is, parallel to the freezing direction, as compared to the y-direction. This could be related to the pore channels in the cryogels aligned to the freezing (x-) direction so that the expansion of the sample in water occurs in the same direction rather than the radial direction. Moreover, the swelling anisotropy calculated as $q_{v,x} / q_{v,y}$ decreases as fibroin

concentration is increased, and the largest swelling anisotropy of 1.17 ± 0.02 was observed at $C_{SF}$ = 4.2 wt%. In Figure 3.9c, the average of the volume swelling ratios in both direction $\bar{q}_v$ together with the weight swelling ratio $q_w$ of the cryogels are plotted against the fibroin concentration $C_{SF}$.

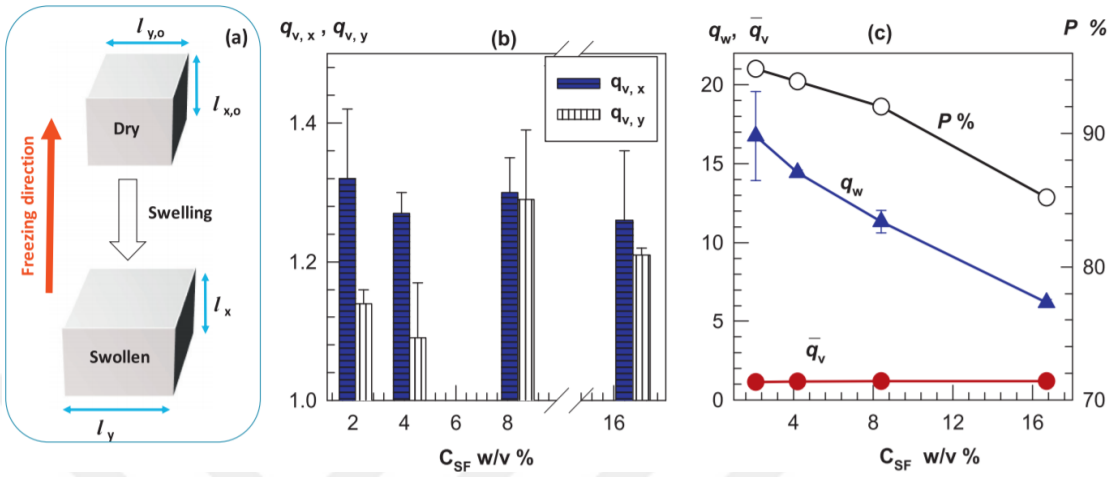


**Figure 3.9 :** (a): Cartoon showing swelling of gel specimen along parallel and perpendicular to the freezing direction. (b): The volume swelling ratio of cryogels measured parallel $q_{v,x}$ and perpendicular to the freezing direction $q_{v,y}$ plotted against $C_{SF}$. (c): The weight $q_w$ and volume swelling ratios $\bar{q}_v$ of cryogels and their swollen state porosities $P$ plotted against $C_{SF}$.

The average volume swelling ratio $\bar{q}_v$ of all cryogels is 1.2 ± 0.1, whereas the weight swelling ratio $q_w$ is between 14 and 21, and it increases as $C_{SF}$ is decreased. Because the volume expansion of gels is related to their crosslink density, the low degree of volume swelling indicates highly crosslinked structure of fibroin network, i.e., pore walls, restricting its expansion due to the favorable mixing entropy effect. A much larger weight swelling as compared to the volume swelling is due to the interconnected open pores that are filling and emptying during swelling and drying, respectively, without changing much the gel volume. Swollen state porosity can be calculated from the swelling ratios as $P = 1 - \bar{q}_v\,[1+(q_w-1)\rho]$ where $\rho$ is the fibroin density (1.35 g/mL) [79]. Open symbols in Figure 3.9c showing porosities reveal that all cryogels are highly porous and the porosity decreases from 96 to 85% with increasing fibroin concentration.

### 3.2.4 Viscoelasticity of cryogels

Viscoelastic properties of the cryogels were investigated by oscillatory deformation tests at a strain amplitude $\gamma_o$ of 1%, which is in the linear regime of the cryogels (Figure 3.10).

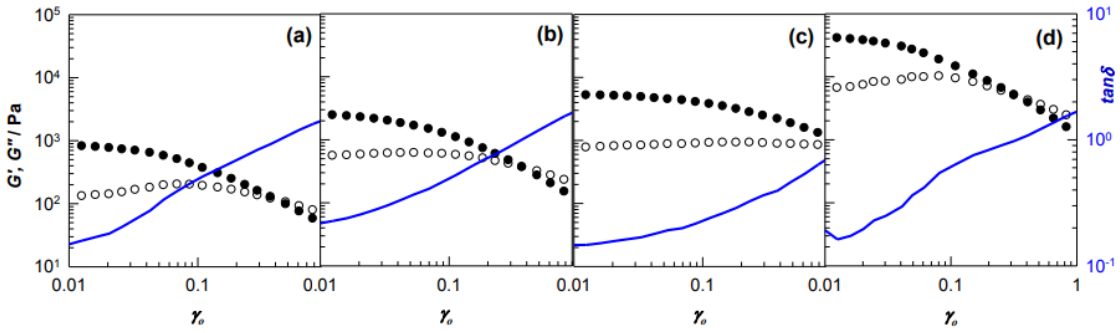


**Figure 3.10 :** Storage modulus *G'* (filled circles), loss modulus *G''* (open symbols), and loss factor *tan δ* (curves) of cryogels plotted against the strain amplitude $\gamma_o$. $\omega$ = 6.28 rad.s$^{-1}$. $C_{SF}$ = 2.1 (a), 4.2 (b), 8.4 (c), and 16.7 wt. % (d).

Figures 3.11a, b show the storage modulus *G'* and loss factor *tan δ* of the cryogels formed at various $C_{SF}$ plotted against the frequency $\omega$. Both *G'* and *tan δ* exhibit weak frequency dependencies reflecting the elastic nature of the cryogels. The modulus *G'* increases from ~1 to ~50 kPa with increasing $C_{SF}$ due to the simultaneous increase of the β-sheet amount in unit volume of cryogel. Moreover, the loss factor *tan δ* is above 0.1 for all cryogels, which is around one order of magnitude larger than that of nonporous fibroin hydrogels [71]. Because *tan δ* is a measure of energy dissipation, this suggests a larger extent of energy dissipation in cryogels as compared to hydrogels. This behavior is likely due to the squeezability of fibroin cryogels which is comparable to squeezing out a sponge. The images in Figure 3.11c demonstrate a macroscopic visualization of this behavior for a cryogel specimen formed at $C_{SF}$ = 16.7 wt%. The specimen could be compressed by a strain $\varepsilon$ of 80% and, upon unloading, it recovers its original shape immediately by soaking up the released water back into its pores. Similar to this macroscopic view, within each cycle of the oscillatory deformation tests, pore walls of fibroin cryogel approach each other and move away again, during which the pore water is squeezed out and soaked up back. This creates viscous stresses and energy dissipation as reflected by increased loss modulus and hence loss factor as compared to nonporous fibroin gels having the same storage modulus [71].

To further demonstrate the energy dissipation, cyclic strain-sweep tests between strain amplitudes $\gamma_o$ 1% and 1000% were conducted at a fixed frequency of 6.28 rad.s$^{-1}$. The results are shown in Figure 3.11d where $G'$ (filled symbols) and the loss modulus $G''$ (open symbols) are plotted against strain $\gamma_o$. Results of up and down strain sweep tests are shown by circles and triangles, respectively.

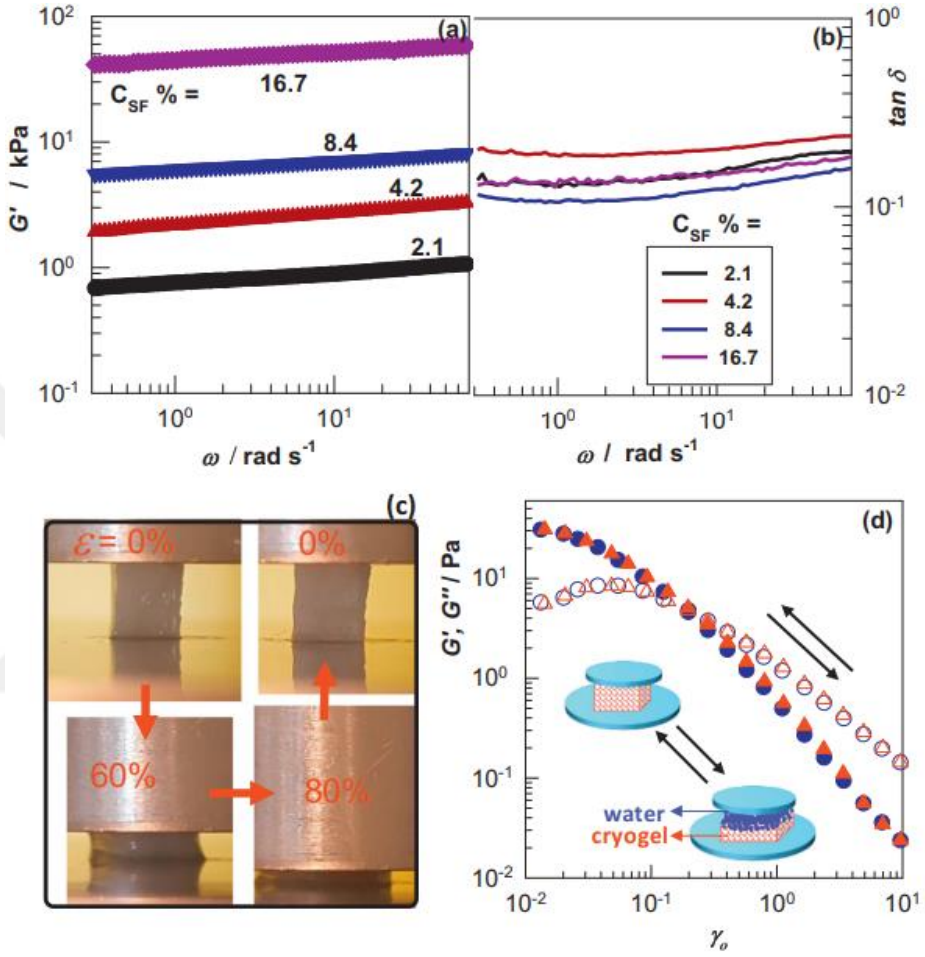


**Figure 3.11 :** (a, b): Storage modulus $G'$ (a) and loss factor $tan\ \delta$ (b) of the cryogels plotted against frequency $\omega$. Strain amplitude $\gamma_o$ = 1%. Fibroin concentrations $C_{SF}$ (in wt%) are indicated. (c): Images of a cryogel specimen during uniaxial compression up to a strain $\varepsilon$ of 80% followed by unloading to zero strain during which the sample soak up the squeezed water back into its pores. (d): $G'$ (filled symbols) and loss modulus $G''$ (open symbols) of the cryogels formed at $C_{SF}$ = 16.7 wt% plotted as a function of strain $\gamma_o$ at $\omega$ = 6.28 rad.s$^{-1}$. Results of up and down strain sweep tests are shown by circles and triangles, respectively. Temperature = 25 °C. The cartoon in the inset shows formation of a water layer between the gel phase and the upper plate of the rheometer at high strains.

An apparent gel-to-sol transition occurs at around 10% strain and the cryogel behaves like a liquid with a loss factor of around 6 at 1000% strain. This transition is reversible, that is, if the strain is reduced back to 1%, the cryogel recovers its initial viscoelastic

properties. We can explain this unusual behavior with the squeezability of the cryogels. As depicted in the inset to Figure 3.11d, as the strain is increased at a fixed frequency, pore water is gradually squeezing out of the cryogel forming a water layer between the gel phase and the upper plate of the rheometer. Thus, the released water instead of the densified cryogel is measured at high strains while reducing the strain results soaking up water back into the gel sample so that the initial properties are recovered.

### 3.2.5 Mechanical anisotropy of cryogels

Figures 3.12a, b show representative stress-strain curves of cryogels formed at $C_{SF}$ = 8.4 and 16.7 wt%, respectively, in dry (left panel) and swollen states (right panel). As illustrated in the inset images, the measurements were performed along parallel (solid curves) and perpendicular to the freezing direction (dotted curves). Comparing the results in both directions, the cryogels exhibit a higher stiffness in the parallel direction at a small strain, whereas the difference observed between parallel and perpendicular directions vanishes at large strains. Moreover, stress-strain curves of both dry and swollen cryogels can be divided into three zones: (i) Elastic region up to a strain of about 10% during which stress linearly increases with strain, (ii) Plateau region between 10 and 60% strains during which the cryogel easily deforms, and (iii) Densification region above 60% strain.

The elastic region is expected for any porous or nonporous elastic material at small strains and indicates that the pore walls of the cryogel remain stable. In the following, this regime was characterized by Young's modulus $E$ calculated from the slope of the curves between 2 and 4% compressions, and the compressive stress $\sigma_{comp}$ which is the stress at 3% strain. In the second region, the fibroin channels building the porous structure of cryogels start to collapse by elastic buckling and continues until the majority of them have done so. As a consequence, the cryogel easily deforms in the plateau region due to squeezing out air or pore water for dry and swollen cryogels, respectively. This region was characterized by the plateau stress $\sigma_p$, which is a measure of the mechanical stability of the porous structure. Figure 3.12c showing the dependence of the plateau stress $\sigma_p$ of dried cryogels on the fibroin concentration $C_{SF}$ in directions parallel (circles) and perpendicular (triangles) to the freezing direction reveals that $\sigma_p$ is larger in parallel direction and it increases from $10^{-2}$ - $10^{-1}$ to $10^{0}$ MPa with increasing $C_{SF}$ from 2.1 to 16.7 wt% reflecting increasing mechanical stability of

the porous structure at high fibroin concentration. However, swelling of cryogels decreases the plateau stress $\sigma_p$ and the plateau becomes less visible due to the glassy-to-rubbery state transition in fibroin network. In the final densification regime, most of the air or pore water in the cryogel is squeezed out so that a nearly nonporous fibroin network is compressed, as manifested by an upward growth of stress (strain-hardening). Because of the disappearance of the pores in this regime, stress-strain curves recorded parallel and perpendicular to the freezing direction approach each other and similar ultimate properties were obtained. This is also illustrated in Figure 3.12d showing the fracture stress $\sigma_f$ of dry and swollen cryogels measured at two directions plotted against $C_{SF}$. $\sigma_f$ slightly increases with $C_{SF}$ and no directional dependence is observable over the whole range of fibroin concentration.

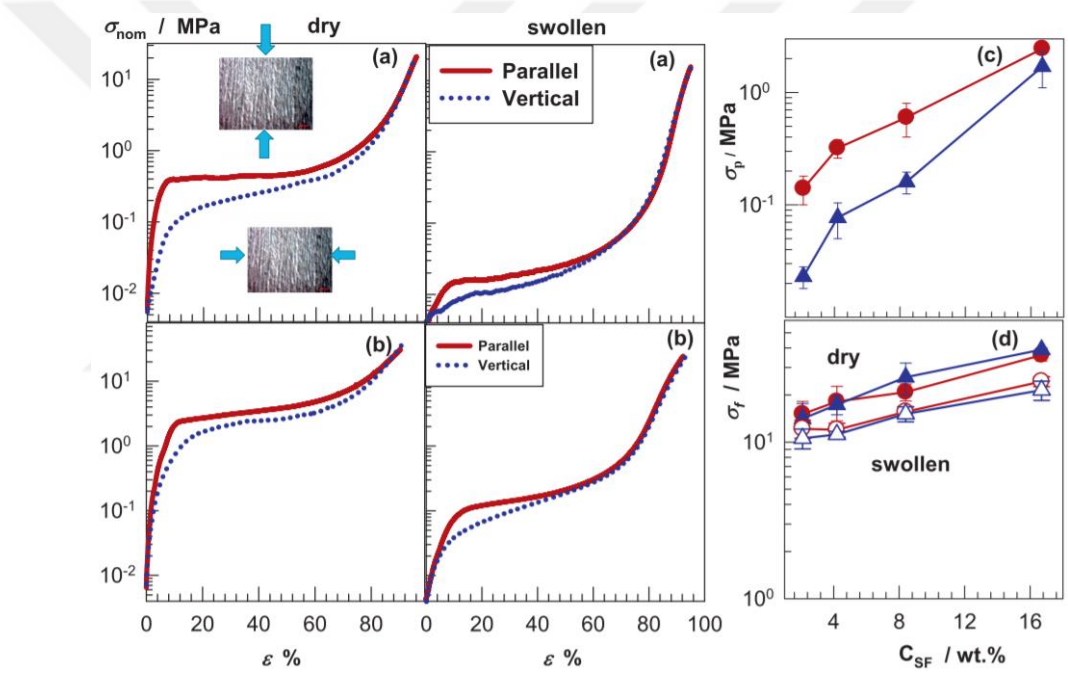


**Figure 3.12 :** (a, b): Compressive stress-strain curves of cryogels formed at $C_{SF}$ = 8.4 (a) and 16.7 wt% (b) in dry (left panel) and swollen states (right panel). Uniaxial compression tests were performed parallel (solid curves) and perpendicular to the freezing direction (dotted curves). (c, d): Plateau stress $\sigma_p$ (c) and fracture stress $\sigma_f$ (d) of cryogels measured in parallel (circles) and perpendicular to the freezing direction (triangles) plotted against the fibroin concentration $C_{SF}$. The $\sigma_p$ data are from dried cryogel samples while $\sigma_f$ data are from dried (filled symbols) and swollen cryogels (open symbols).

Figure 3.13a, b show $C_{SF}$ dependences of Young's modulus $E$ (upper panel) and compressive stress $\sigma_{comp}$ (bottom panel) of dry and swollen cryogels, respectively, measured along parallel (circles) and perpendicular to the freezing direction (triangles). In both directions, increasing fibroin concentration $C_{SF}$ improves the

mechanical performance of cryogels both in their dry and swollen states. The modulus $E$ and compressive stress $\sigma_{comp}$ in the parallel direction are much higher than those in the perpendicular direction. For instance, at $C_{SF}$ = 16.7 wt% the moduli $E_{\parallel}$ and $E_{\perp}$ are 18 ± 3 and 5.8 ± 0.3 MPa, respectively. Moreover, the difference in the modulus becomes larger with increasing $C_{SF}$. Figure 3.13c, d show the anisotropies in modulus, compressive stress $\sigma_{comp}$, and fracture stress $\sigma_f$ of dry and swollen cryogels, respectively, plotted against $C_{SF}$. The anisotropy in the fracture stress is close to unity revealing the isotropic behavior of cryogels at large strains whereas both the modulus and compressive stress show directional dependences. In dry state, the maximum degree of anisotropy in the modulus $E_{\parallel}/E_{\perp}$ is 21 ± 5 which was observed at the lowest fibroin concentration (2.1 wt%), i.e., $E_{\parallel}$ = 2.3 ± 0.5 MPa and $E_{\perp}$ = 0.11 ± 0.03 MPa. This value is the highest modulus anisotropy reported so far in the literature. The anisotropy in the compressive stress also attains a maximum value of 7 ± 2 at 2.1 wt% fibroin. In swollen state, the maximum modulus and compressive stress anisotropies are 8 ± 2 and 1.9 ± 0.5, respectively, observed at 4.2 wt% $C_{SF}$.

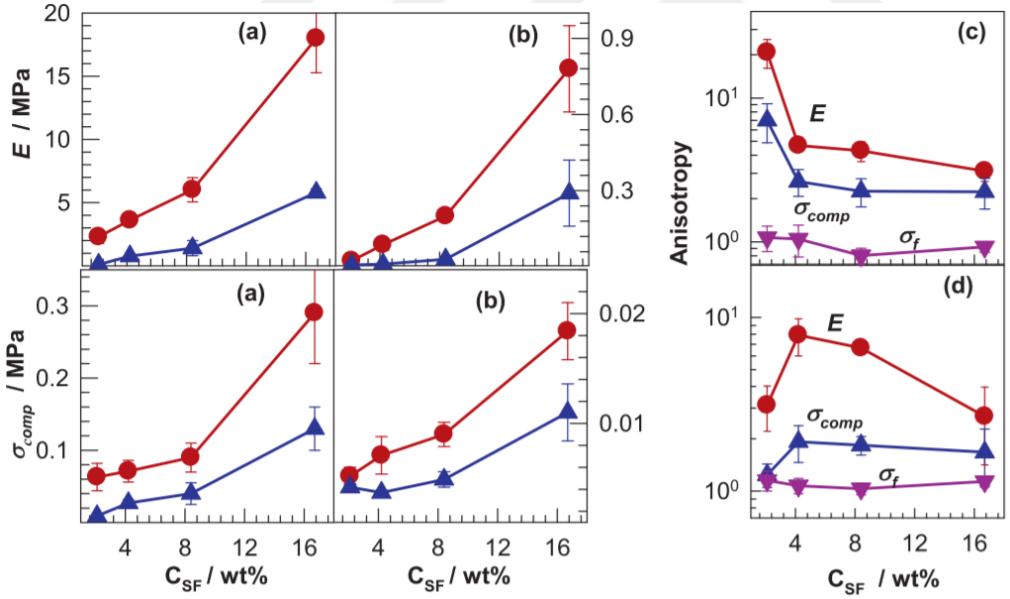


**Figure 3.13 :** (a, b): Young's modulus $E$ (upper panel) and compressive stress $\sigma_{comp}$ (bottom panel) of dried (a) and swollen cryogels (b) measured in parallel (circles) and perpendicular to the freezing direction (triangles) plotted against fibroin concentration $C_{SF}$. (c, d): Anisotropies in modulus $E$, compressive stress $\sigma_{comp}$, and fracture stress $\sigma_f$ of dry (c) and swollen cryogels (d) plotted against fibroin concentration $C_{SF}$.

As mentioned in the experimental part, Young's modulus $E$ of the cryogels was calculated from the slope of the stress-strain curves between 2 and 4% strains. Detailed

calculations revealed that the slope of the curves continuously varies even in the elastic region. For instance, Figure 3.14a shows stress-strain curves of fibroin cryogels formed at various SF concentrations up to a strain of 10%. The measurements were conducted along parallel (solid curves) and perpendicular to the freezing direction (dashed curves). From these curves the instantaneous moduli $E_i$ was calculated as the slope between two consecutive data points and plotted against the strain $\varepsilon$ in Figure 3.14b.

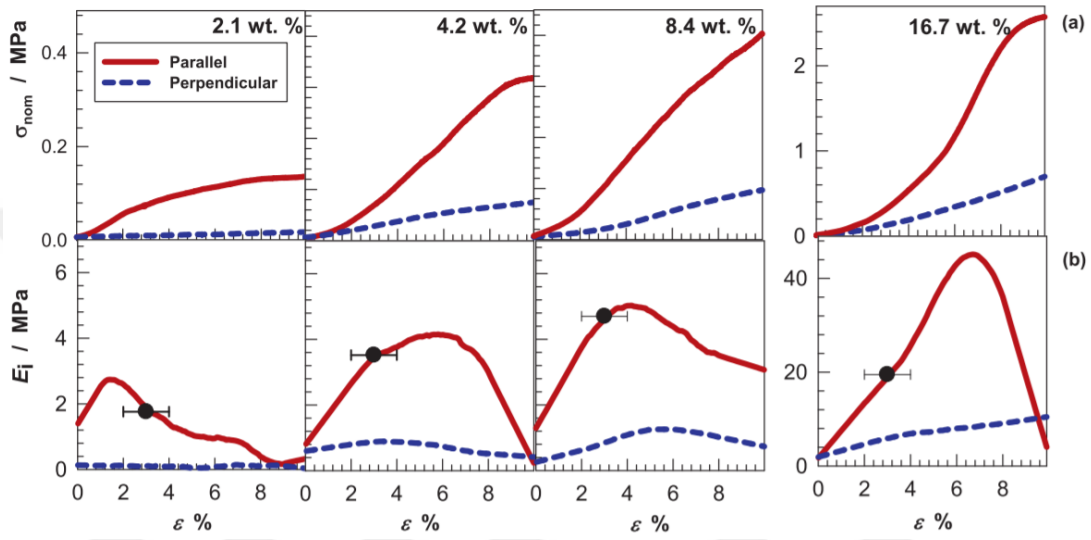


**Figure 3.14 :** Stress-strain curves up to a strain of 10% (a) and instantaneous modulus $E_i$ of the cryogels (b) plotted against the strain $\varepsilon$. Solid and dashed curves are the results obtained from parallel and perpendicular to the freezing direction, respectively. The symbols represent the Young's modulus of the cryogels and the vertical bars indicate the range between 2 and 4% strain where the modulus was calculated.

To eliminate noise in the data series, they were smoothed using the negative exponential procedure with a sampling proportion of 0.4, i.e., 10 data points for 4 smoothed values (Figure 3.15) [92]. The solid circles in Figure 3.14b show Young's moduli $E$ of the cryogels. It is seen that, similar to the cancellous bone [93], all fibroin scaffolds exhibit peak moduli at a critical strain which are larger than their Young's moduli $E$. For instance, $E_i$ of the cryogel formed at $C_{SF}$ = 16.7 wt% is 45 MPa which is about 2.5-fold larger than its Young's modulus. Moreover, the modulus anisotropy at the peak position, i.e., the $E_{i,\parallel}/E_{i,\perp}$ ratio is also larger than that calculated from Young's modulus as $E_\parallel/E_\perp$. For instance, $E_{i,\parallel}/E_{i,\perp}$ and $E_\parallel/E_\perp$ ratios are 3.1 ± 0.5 and 5.4 ± 0.3, respectively, for the cryogels formed at $C_{SF}$ = 16.7 wt%.

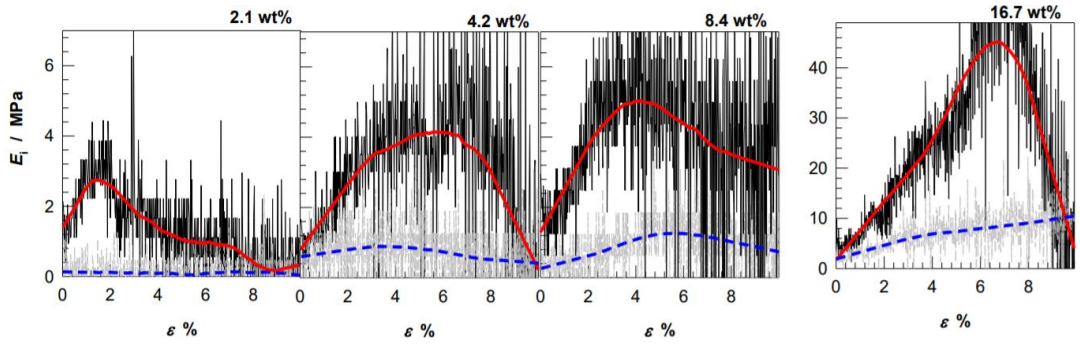


**Figure 3.15 :** Instantaneous modulus $E_i$ of the cryogels plotted against the strain $\varepsilon$. Solid red and dashed blue curves are the results obtained from parallel and perpendicular to the freezing direction, respectively. They were obtained after smoothing the raw data shown by black and gray scattering data using negative exponential procedure with a sampling proportion of 0.4.

### 3.2.6 Mechanism of energy dissipation

Cyclic mechanical tests are a mean to investigate the anisotropy in viscous energy dissipation of the cryogels. We conducted uniaxial compression tests at a strain rate of 0.3 mm.min$^{-1}$ up to a maximum strain $\varepsilon_{max}$ followed by unloading at the same rate to zero strain. This loading/ unloading cycle was successively repeated with a waiting time of 5 min between the cycles during which a few drops of water was added to the gel specimen to eliminate water loss by evaporation.

Figure 3.16a, b show typical stress-strain curves from four successive cyclic compression tests to a fixed maximum strain $\varepsilon_{max}$ of 80% (a) and with increasing $\varepsilon_{max}$ from 20 to 80% are shown (b). The tests were conducted parallel to the freezing direction on the cryogels formed at $C_{SF}$ = 4.2 wt%. The loading and unloading curves are shown by the solid and dotted lines, respectively. The general trend is that the unloading curves follow a different path from the loading ones revealing energy dissipation during the mechanical cycles. Moreover, each loading curve follows previous loading indicating that the cycles are reversible, i.e., the original microstructure of the cryogel is recovered after the cycle. This is an indication of self-recoverability of fibroin cryogels, as also illustrated in Figure 3.11c showing a macroscopic visualization of this behavior. Indeed, for $\varepsilon_{max}$ = 80% the dissipated (hysteresis) energy $U_{hys}$ calculated from the area between loading and unloading curves is independent on the number of cycles and equals to 4 ± 1 kJ.m$^{-3}$.

Figure 3.16c shows the hysteresis energies $U_{hys}$ of the cryogels formed at various fibroin concentrations $C_{SF}$ plotted against the maximum strain $\varepsilon_{max}$. $U_{hys}$ data were

calculated from cyclic mechanical tests conducted parallel (filled symbols) and perpendicular to the freezing direction (open symbols). For the sake of clarity, the data were vertically shifted by a factor $K$. It is seen that at small maximum strains $\varepsilon_{max}$, $U_{hys}$ is about one order of magnitude larger in the parallel direction reflecting larger viscous energy dissipation as compared to the perpendicular direction. The directional dependence of $U_{hys}$ decreases with increasing strain and disappears at $\varepsilon_{max}$ = 80%. This finding is in accord with the mechanical test results given in Figure 3.12 showing that the ultimate properties of cryogels are almost independent of direction.

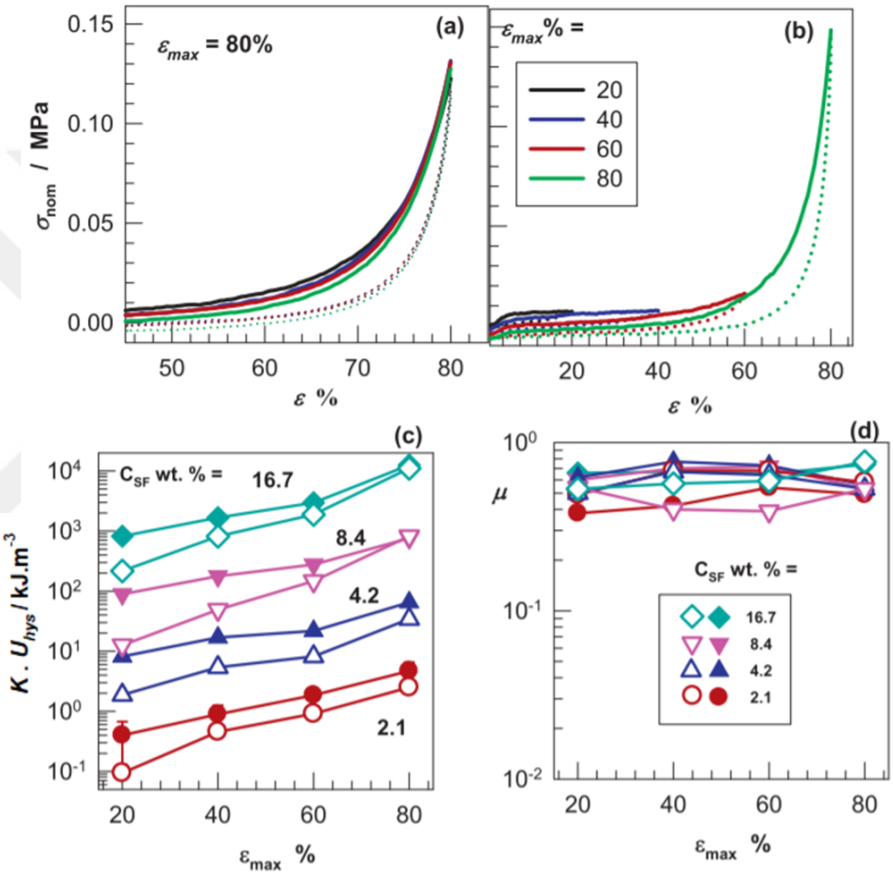


**Figure 3.16 :** (a, b): Nominal stress $\sigma_{nom}$ vs elongation ratio $\varepsilon$ curves from cyclic compression tests of swollen cryogels conducted parallel to the freezing direction. $C_{SF}$ = 4.2 wt%. Four successive cycles to a maximum strain $\varepsilon_{max}$ = 80% (a) and with increasing $\varepsilon_{max}$ from 20 to 80% are shown (b). Temperature = 24 ± 1 °C. (c): Hysteresis energies $U_{hys}$ calculated from the cyclic test results shown as a function of $\varepsilon_{max}$. The measurements were conducted parallel (filled symbols) and perpendicular to the freezing direction (open symbols). For the sake of clarity, the data were vertically shifted by a factor $K$, which is 1, 10, 70, and 60 for $C_{SF}$ = 2.1, 4.2, 8.4, and 16.7 wt%, respectively. (d): Dissipated energy $\mu$ per loading energy in parallel (filled symbols) and perpendicular directions (open symbols) plotted against $\varepsilon_{max}$.

We can explain the above results with the friction-induced energy dissipation in the cryogels. Because of the squeezability of the cryogels, high friction between fibroin

pore walls can be produced when water moves through the pores, as reported previously [94]. Thus, the friction seems to be a primary factor responsible for the energy dissipation. According to the Amonton's law, frictional force $F$ between two solids is related to the load $W$ forcing them together by $F = \mu W$ where $\mu$ is the frictional coefficient and is generally between 0.5 and 1.0 [95]. Although the frictional behavior of hydrogels deviates from the Amonton's law [96], swelling of fibroin cryogels mainly occurs by filling of the pores with water rather than volume swelling, and the pore walls absorb only 20% water to attain the equilibrium state (Figure 3.9c).

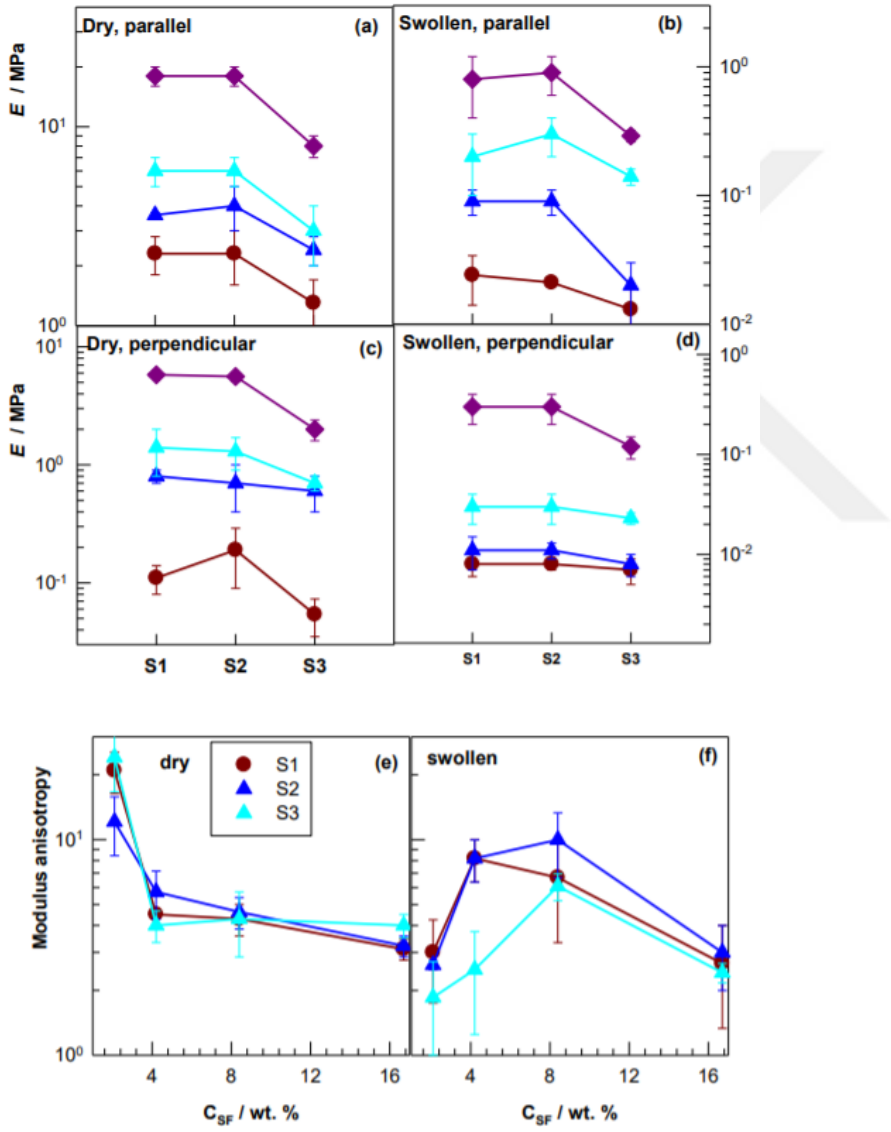


**Figure 3.17 :** (a-d): Young's modulus $E$ of dried (a, c) and swollen cryogels (b, d) measured in parallel (a, b) and perpendicular to the freezing direction (c, d) plotted against the type of cryogels. For the types S1, S2, and S3 cryogels, the freezing temperatures are -196, -196, and -30 °C while the cryogelation temperatures are -18, -6, and -18 °C, respectively. (e, f): Modulus anisotropies of dry (e) and swollen cryogels (f) plotted against fibroin concentration $C_{SF}$.

Thus, fibroin pore walls of cryogels are solid-like as compared to highly swollen hydrogels. Moreover, the ratio of dissipated energy to the loading energy, that is, the amount of energy dissipated per energy given can be regarded as the frictional coefficient $\mu$, which should be independent of $C_{SF}$, or the direction of the measurements. By dividing $U_{hys}$ to the area under the loading curve, we calculated $\mu$ for all hydrogels and plotted against $\varepsilon_{max}$ in Figure 3.16d. It is seen that the $\mu$ is indeed independent on the direction of the measurements, or fibroin concentration $C_{SF}$, and it equals to $0.6 \pm 0.1$. Thus, around 60% of the energy given to the cryogels are dissipated due to the friction between the pore walls. Because creating an effective energy dissipation mechanism is the main technique for toughness improvement in hydrogels [15], the large friction-induced energy dissipation in cryogels is responsible for their almost complete squeezability and self-recoverability.

The results summarized above were obtained by directional freezing of the gelation solution at -196 °C followed by cryogelation at -18 °C to obtain fibroin cryogels. Increasing the cryogelation temperature from -18 to -6 °C resulted in no change in the mechanical properties as well as in the degree of anisotropy in the cryogels (Figure 3.17). However, conducting the initial directional freezing process at -30 °C in ethylene glycol/water mixture instead of -196 °C slightly deteriorated the mechanical properties of the cryogels (Figure 3.17). This could be related to the formation of larger pores due to the slower rate of freezing of the solution at -30 °C as shown in Figures 3.1d and 3.5, leading to a decrease in the mechanical performance of the cryogels.

### 3.3 Conclusions

A novel directional freezing/cryogelation method was described for fabrication of high-strength and rapid self-recoverable silk fibroin scaffolds with anisotropic properties. Significant anisotropies in the microstructure, swelling, and mechanical properties were achieved that could be tuned by the silk fibroin concentration. By adjusting the synthesis parameters, we were able to create fibroin scaffolds exhibit the highest modulus anisotropy so far reported, $21 \pm 5$, with moduli $E = 2.3 \pm 0.5$ and $0.11 \pm 0.03$ MPa measured along parallel and perpendicular to the freezing direction, respectively. Although the cryogels exhibit solid-like behavior with a weak frequency dependent storage modulus, they undergo gel-to-sol transition at around 10% strain, which is attributed to their squeezability creating viscous stresses and energy

dissipation. Stress-strain curves of cryogels reveal the existence of two phases: The low-strain phase in which the fibroin micro-channels are mostly straight, i.e., pore walls are stable, and a high-strain phase in which the micro-channels are mostly buckled so that the pores are disappeared. The transition between the two phases occurs over the plateau regime during which water is squeezed out easily. Cyclic mechanical tests reveal that the friction between the fibroin pore walls is the primary factor responsible for the energy dissipation. Independent on the fibroin concentration or direction of the measurements, 60% of the mechanical energy given to the cryogels are dissipated due to the friction which is responsible for their almost complete squeezability and self-recoverability.

## 4. SINGLE-, DOUBLE-, AND TRIPLE-NETWORK MACROPOROUS RUBBERS AS A PASSIVE SAMPLER[3]

In the past decades, large quantities of organic compounds entering aquatic systems create acutely toxic effects and chronic abnormalities in aquatic organisms. Although the dissolved concentration of organic compounds in aquatic systems is low because of their very low water solubilities, they are easily uptaken by the organisms, and hence, these pollutants move through the food chain with increasing level of biomagnification. It is thus a challenging task to detect their levels with sufficient selectivity and sensitivity. Passive sampling is an effective technique to detect organic compounds such as polycyclic aromatic hydrocarbons (PAHs) at very low concentrations in water by accumulating them in their structure to a measurable concentration level [97-102]. When compared to biomonitoring carried out with organisms, passive samplers are not affected by biological activities such as metabolism and excretion, which may alter the sampled amounts of the compounds of interest. Besides, passive samplers provide time-weighted average concentrations, which are not affected by instantaneous pollutant inputs to the sampling site.

Biphasic passive samplers such as semipermeable membrane devices (SPMDs) consisting of polyethylene membranes filled with triolein have been widely used as a passive sampler to monitor organic chemicals [103]. Recent studies show that monophasic polymeric passive samplers such as polyoxymethylene, low-density polyethylene, and polydimethylsiloxane (PDMS) have several advantages over SPDMs as effective passive samplers in monitoring pollution level in aquatic systems [104]. To our knowledge, polymeric passive samplers developed so far have a nonporous structure, and hence, the diffusion of organic chemicals into the passive sampler determines the absorption process of organic chemicals. In contrast, for a

[3] This chapter is based on the paper "Yetiskin, B., Tureyen, O. E., Yilmaz, A., Yakan, S. D., Okay, O. S., & Okay, O. (2019). Single-, double-, and triple-network macroporous rubbers as a passive sampler. *ACS Appl. Mater. Inter.*, *11*(31), 28317-28326."

passive sampler with interconnected pore structure, organic chemicals are absorbed through its pores by convection which is faster than diffusion [79].

Although several strategies have been developed to produce macroporous polymers [105-108], cryogelation technique has several advantages because of the extraordinary properties of the resulting polymers such as high porosity, stable porous structure, sponge-like squeezability, and a high mechanical strength [55,56,109,110]. By this technique, the cross-linking reactions of linear polymers are conducted in aqueous or organic solutions below the freezing temperature, as schematically illustrated in Figure 4.1a,b. As the solvent freezes, polymers and cross-linkers separated from the solvent crystals accumulate in still unfrozen regions of the cryogelation system, leading to the formation of a concentrated polymer solution, called cryoconcentration (Figure 4.1b). After the thermal equilibrium is reached with the surroundings, the cryogelation system is composed of a highly concentrated solution phase and pure solvent crystals [55]. Generally, the effect of cryoconcentration is dominated over the reduction in cross-linking rates at low temperatures so that cross-linked polymers can be prepared even at very low concentrations of the polymer [55]. After completing the cryogelation reaction and melting the solvent crystals, a three-dimensional (3D) network structure with macropores is obtained (Figure 4.1c).

Cryogelation reactions are mainly conducted in aqueous solutions to prepare macroporous hydrogels. Lozinsky et al. were the first to investigate the cryogelation reactions of polystyrene and *N*-vinylpyrrolidone-maleic anhydride copolymers in organic solutions in the presence of chemical crosslinkers [111]. They showed that the reactions conducted in dimethyl sulfoxide (DMSO) and nitrobenzene at subzero temperatures display similar characteristics as that in aqueous solutions [111]. Recently, hydrophobic cryogels based on acrylic and methacrylic monomers and PDMS were prepared in organic solvents including dioxane, cyclohexane, and DMSO [60,62,112,113]. Wong et al. presented cryogelation of acrylate-based monomer mixtures in DMSO to synthesize shape memory polymer foams with tunable porous morphology and properties [113]. It was shown that the alignment of the pores and the porosity can be varied by changing the freezing rate and monomer concentration.

Butyl rubber (isobutylene-isoprene rubber, IIR) is a synthetic elastomer composed of isobutylene and 0.5-3 mol% isoprene units serving as sites for covalent cross-linking

of the rubber. Soft IIR can be converted into an elastic IIR by its cross-linking reactions, called vulcanization, usually conducted using sulfur or sulfur compounds as cross-linkers in the bulk phase [114].

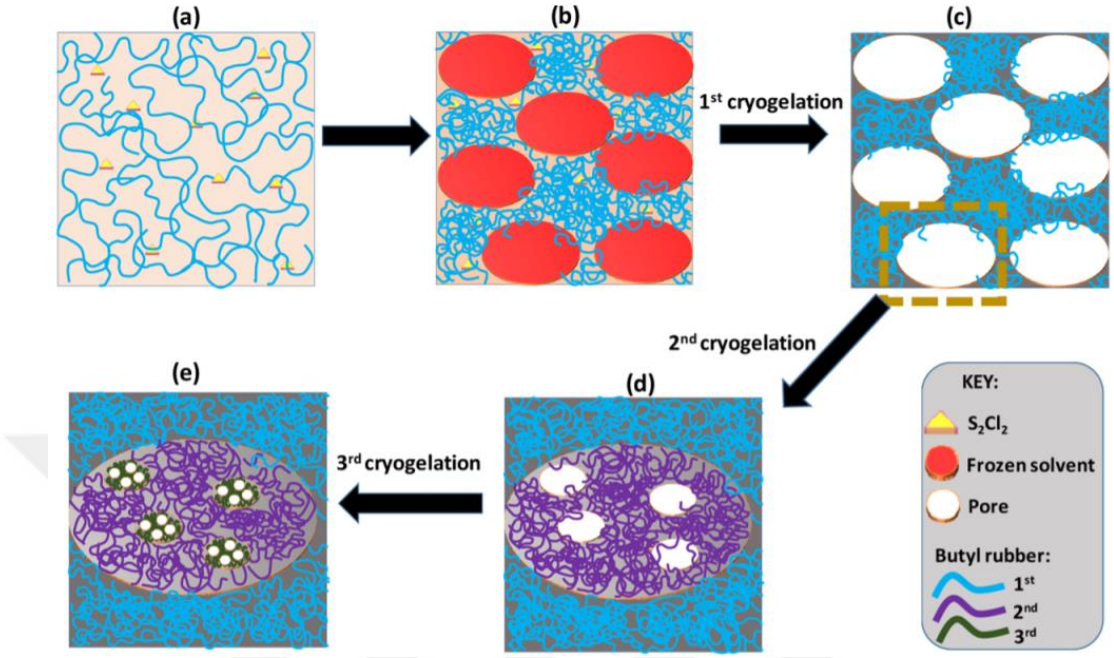


**Figure 4.1 :** Cartoon Showing Formation of Single- (a−c), Double- (d), and Triple-Network Rubbers (e).

We have shown that the vulcanization of several rubbers including IIR can be conducted in organic solutions using sulfur monochloride $S_2Cl_2$ as a cross-linker via cryogelation technique to produce macroporous rubbers [115,116]. Benzene with a freezing temperature of 5.5 °C is generally used as the solvent, and cryogelation reactions are usually conducted 20-25 °C below this temperature [115,117]. High toughness, squeezability, hydrophobicity, and fast responsivity of macroporous rubbers expand the potential applications of IIR such as absorbent materials for the removal of oil spill from aquatic environments [118,119]. In our previous work [115], we investigated the effects of various synthetic parameters including the temperature and the concentrations of the cross-linker $S_2Cl_2$ and butyl rubber on the morphology of the cryogels. The average width and length of the pores were found to be 40 ± 12 and 58 ± 17 μm, respectively, independent of the concentrations of rubber and $S_2Cl_2$ as well as on the cryogelation temperature. However, the efficiency of macroporous IIR rubbers as a passive sampler for monitoring PAHs in the aquatic environment requires a tunable porous structure. Moreover, the existence of both large and small pores in a sorbent material is important because of the opposite effect of the pore size

on the sorption rate and sorption capacity. Such a porous structure in rubber cryogels cannot be achieved using the one-step cryogelation reaction reported before.

We present here for the first time the fabrication of novel macroporous IIR rubbers with double-network (DN) and triple-network (TN) structures exhibiting a wide range of tunable pore structures and mechanical properties. The DN structure was generated by conducting the cryogelation reactions in the large pores of a single-network (SN) rubber, as illustrated in Figure 4.1d. Thus, filling the pores of the SN rubber with a benzene solution of IIR and $S_2Cl_2$ cross-linker followed by cryogelation leads to the formation of a second generation of pores within the large pores of the SN rubber. Repeating this step leads to the formation of a TN rubber containing a third generation of pores (Figure 4.1e). As will be seen below, macroporous SN, DN, and TN rubbers with a tunable pore structure can successfully be prepared by successive cryogelation reactions. We show that the mass ratio of the network components determines the morphology and mechanical properties of macroporous rubbers and their effectivity as passive samplers for monitoring PAHs in an aqueous environment.

## 4.1 Experimental Part

### 4.1.1 Materials

Butyl rubber (IIR, 1675N, Togliatti, Russia) containing 1.5 mol% isoprene units was dissolved in toluene to remove the impurities and then precipitated in an excess of methanol, followed by drying under vacuum to constant weight. Sulfur monochloride ($S_2Cl_2$, Sigma Aldrich), benzene (Merck), toluene, and methanol (both Tekkim, Turkey) were used without further purification. PDMS elastomer kSil GP60 as a reference passive sampler was purchased from Silicone Engineering Ltd. (Blackburn, UK). PAHs used in the sorption experiments, namely, naphthalene (Naph, Sigma Aldrich), fluoranthene (Fluo, Fluka), pyrene (Pyr, Fluka), and phenanthrene (Phen, Fluka), were used as received.

### 4.1.2 Preparation of macroporous rubbers

Macroporous SN, DN, and TN butyl rubbers (IIR) were prepared in benzene solutions of IIR using $S_2Cl_2$ as a cross-linker. $S_2Cl_2$ concentration and the cryogelation temperature were fixed at 6 v/w% (with respect to IIR) and -18 °C, respectively, which

were the optimum conditions for the cryogelation of several rubbers with a SN structure [115,119]. The SN rubber was prepared at an IIR concentration ($C_1$) of 5 w/v%. Briefly, IIR (5 g) was dissolved in benzene (100 mL) in a glass beaker at 23 ± 2 °C overnight to obtain a homogeneous solution. After addition of $S_2Cl_2$ (0.30 mL) and stirring for 2 min, the solution was transferred into 5 mL plastic syringes of 14 mm in diameter and Petri dishes of 10 cm in diameter and 13 mm in height. Finally, the syringes and sealed Petri dishes were immersed in a deep freezer at -18 °C, and the reactions were conducted for 24 h. In this way, macroporous SN rubber specimens in the form of cylinders of around 14 mm in diameter and rubber sheets of about 3 mm in thickness were obtained. Macroporous SN rubbers were then extracted in toluene and finally dried to constant mass, as described in the next section.

DN rubbers were synthesized by swelling dried SN rubber in benzene solution of IIR at various concentrations ($C_2$) between 2.5 and 10 w/v% containing a $S_2Cl_2$ cross-linker. Typically, dried SN rubber specimens in the form of cylinders of 1 cm in length and sheets of around 3 mm in thickness were immersed in 100 mL of benzene solution containing IIR (2.5 to 10 g) and $S_2Cl_2$ (6 v/w% with respect to IIR). After attaining swelling equilibrium which required 5-10 min, swollen rubber specimens in the form of cylinders and sheets were sealed in 10 mL plastic syringes and closed Petri dishes. They were then placed in a deep freezer at -18 °C, and cryogelation reactions were conducted for 24 h. TN rubbers were prepared as described above by immersing dried DN rubber prepared at $C_2$= 10 w/v % in benzene solution of IIR at a concentration ($C_3$) of 10 w/v % containing 6 v/w % $S_2Cl_2$. The mass ratio of the network components with respect to the first single network, $w_R$, was calculated as

$$w_R = w_{2/1} + C_3(q_{w,2} - 1)(1 + w_{2/1}) \tag{4.1}$$

where $w_{2/1}$ is the ratio of the second to the first network, that is, $w_{2/1} = (q_{w,1} - 1)C_2$, $q_{w,1}$ and $q_{w,2}$ are the equilibrium weight swelling ratios (swollen mass/dry mass) of the SN and DN rubbers, respectively, in benzene solution of IIR and $S_2Cl_2$. The rubber concentration $C_{IIR}$ just after cryogelation in benzene was 5.7 wt% for the SN rubber, whereas for DN and TN rubbers, $C_{IIR}$ was calculated using the equations

$$C_{IIR}wt\% = \frac{(1+w_{2/1})}{q_{w,1}} x100 \tag{4.2a}$$

$$C_{IIR}wt\% = \frac{1+(q_{w,2}-1)C_3}{q_{w,2}} x100 \tag{4.2b}$$

respectively. Synthesis conditions of macroporous SN, DN, and TN rubbers are compiled in Table 4.1.

**Table 4.1 :** Preparation condition of SN, DN, and TN Rubbers. Standard deviations are in parenthesis.

| Code | $C_1$ w/v% | $C_2$ w/v% | $C_3$ w/v% | $q_{w,1}$ | $q_{w,2}$ | $w_R$ | $C_{IIR}$ wt% |
|---|---|---|---|---|---|---|---|
| SN | 5 | 0 | 0 | 22 (3) | - | 0 | 5.7 |
| DN | 5 | 2.5 | 0 | 19 (1) | - | 0.45 (0.03) | 7.6 (0.3) |
| DN | 5 | 5 | 0 | 18 (1) | - | 0.85 (0.05) | 10.3 (0.3) |
| DN | 5 | 7.5 | 0 | 19 (1) | - | 1.35 (0.08) | 12.4 (0.4) |
| DN | 5 | 10 | 0 | 20 (2) | - | 1.9 (0.2) | 14.5 (1) |
| TN | 5 | 10 | 10 | 20 (2) | 10 (3) | 4.5 (0.4) | 19 (2) |

### 4.1.3 Characterization of macroporous rubbers

Swelling and gel fraction measurements were performed by immersing cross-linked rubber specimens of about 1 cm in length in an excess of toluene, a good solvent for IIR, at 23 ± 2 °C for at least 1 week to remove soluble species. To eliminate the solvent effect on the microstructure of the rubbers, toluene in the specimens was then replaced with the poor solvent methanol and finally dried to constant mass under vacuum. The gel fraction $W_g$ defined as the mass of toluene-insoluble IIR prepared from 1 g of linear IIR was calculated using the equation

$$W_g = \frac{m_{dry}}{m_0 c_{IIR}} \tag{4.3}$$

where $m_{dry}$ and $m_0$ are the masses of the rubber samples in dry state and after preparation, respectively. The equilibrium weight and volume swelling ratios of the rubbers in toluene, represented by $q_w$ and $q_v$, respectively, were calculated as

$$q_w = \frac{m_{swl}}{m_{dry}} \tag{4.4a}$$

$$q_v = \left(\frac{D_{swl}}{D_{dry}}\right)^3 \tag{4.4b}$$

where $m_{swl}$ and $D_{swl}$ are the mass and the diameter of swollen rubber specimens, respectively, and $D_{dry}$ is the diameter of the dry rubber specimen. The total volume of the pores $V_p$ in the rubbers was calculated from methanol uptake capacity because it is a poor solvent for IIR and hence preferentially enters the open pores. To determine $V_p$, rubber specimens in the dry state were placed in excess amount of methanol, and the

mass $m_M$ of the specimens was measured. $V_p$, the total pore volume per unit mass of the rubber, was estimated by

$$V_P = \frac{m_M - m_{dry}}{d_M m_{dry}} \quad (4.5)$$

where $d_M$ is methanol density (0.792 g.mL$^{-1}$).

The morphology of macroporous rubbers was investigated using scanning electron microscopy (SEM) and micro-computed tomography (μ-CT). SEM images of the samples were recorded on a Tescan GAIA 3 field emission scanning electron microscope after sputtercoating with gold palladium on a Leica ACE 600 high vacuum sputter coater. The average diameter *D* of the pores was calculated by analyzing at least 10 SEM images of various magnifications using ImageJ software (NIH, USA). μ-CT scanning was conducted on a μ-CT Skyscan 1272 (Bruker, Belgium) without a filter and using the following parameters: 15.3 μm pixel resolution, 55 kV voltage, 60 μA current, 180° rotation around vertical axes, 70 ms integration time. The details of the measurements and the treatment of data were reported before [120].

Mechanical measurements were conducted using a Zwick Roell instrument with a 500 N load cell. All the tests were carried out at 23 ± 2 °C and at a strain rate of 5 min$^{-1}$. The nominal stress $\sigma_{nom}$, the force per cross-sectional area of the undeformed specimen, and the fractional deformation $\varepsilon$ were recorded. Tensile tests were conducted on the rubber specimens in the form of sheets of about 10 mm in length and 2 mm in thickness. Young's modulus *E* of the rubber was calculated from the slope of $\sigma_{nom}$ - $\varepsilon$ curves between 5 and 15% elongation. Cylindrical rubber specimens of 14 mm in diameter and 3 mm in thickness were subjected to uniaxial compression tests, as detailed before [76]. To demonstrate the self-recoverability of the rubbers, successive compression cycles were conducted by first compressing the rubber specimens to a maximum strain of 80%, followed by unloading to zero strain at the same rate. After a waiting time of 1 min, these loading and unloading steps were repeated 9 times.

### 4.1.4 Sorption tests

Macroporous rubbers and PDMS as a reference material were used for the sorption experiments of naphthalene (Naph), phenanthrene (Phen), fluoranthene (Fluo), and pyrene (Pyr) from aqueous solutions at 23 ± 1 °C. The experiments were carried out by immersing rubber specimens, each 0.100 g, in 40 mL of aqueous PAH solutions

prepared in filtered clean seawater with a salinity of 22 ppt. The PAH concentrations used in the experiments were selected by considering the solubility limits of the PAH compounds. In the first phase of the experiments, the concentration of PAH in the solution was monitored up to 12 h to highlight the initial uptake rate of the passive samplers. In the second phase, cumulative PAH concentration in the passive samplers was monitored over 30 - 40 days by refreshing PAH solution every day. The PAH concentration in the solution was determined by taking subsamples at predetermined time intervals and measuring the concentrations against the standards using a fluorescence spectrophotometer (Perkin Elmer, LS-55).

## 4.2 Results and Discussion

### 4.2.1 Macroporous structure of a cross-linked butyl rubber

Macroporous cross-linked rubber with a SN structure was prepared from the benzene solution of 5 w/v% butyl rubber (IIR) at -18 °C in the presence of sulfur monochloride ($S_2Cl_2$) as a cross-linker [115]. The filling of the pores in the SN rubber with a second benzene solution of IIR at various concentrations and $S_2Cl_2$ followed by cryogelation at -18 °C resulted in DN rubbers. By increasing the IIR concentration in the second benzene solution from 2.5 to 10 w/v%, we were able to increase the weight ratio $w_R$ of the second-to-first network components in the DN rubber up to 1.9 (Table 4.1). As will be seen below, increasing the weight ratio $w_R$ significantly improves the mechanical properties of the rubbers. However, this ratio could not be further increased because the second benzene solution containing more than 10 wt% IIR was too viscous hindering its diffusion into the SN rubber. Therefore, we introduced the triple-networking strategy to further increase the weight ratio $w_R$ of the network components. Thus, the pore filling of the DN rubber formed at $w_R$ = 1.9 with a third benzene solution of 10 wt% IIR and $S_2Cl_2$ followed by cryogelation resulted in TN rubbers with a weight ratio $w_R$ of the network components of 4.5. The measurement of the gel fractions $W_g$ revealed that all rubbers exhibit a $W_g$ value of around unity, indicating that the linear IIR was completely incorporated into the rubber network, that is, the vulcanization of IIR at -18 °C was complete (Table 4.2).

Figure 4.2a shows the equilibrium weight $q_w$ (filled symbols) and volume swelling ratios $q_v$ (open symbols) of the rubbers in toluene, a good solvent for IIR, plotted as a

function of the ratio of the network components $w_R$. SN rubber with $w_R$ = 0 exhibits a large weight swelling ratio $q_w$ of 22 ± 3, whereas increasing $w_R$ by introducing the second and third network components into the SN decreases $q_w$ continuously and becomes 9 ± 1 at the highest $w_R$ ratio of 4.5. In contrast, the volume swelling degree $q_v$ is $w_R$ -independent and remains at 3.1 ± 0.2. Because volume swelling of a cross-linked porous rubber in a good solvent leads to the expansion of the polymer network because of the attractive polymer-solvent interactions, whereas its swelling ratio by weight additionally includes pore filling with the solvent, one may estimate the total open porosity $P$ from the difference between $q_w$ and $q_v$ by

$$P\ \% = (1 - \frac{q_v}{1+(q_w-1)d_2/d_1})x10^2 \quad (4.6)$$

where $d_1$ and $d_2$ are the densities of toluene (0.867 g.mL$^{-1}$) and IIR (0.92 g.mL$^{-1}$), respectively.

**Table 4.2 :** Gel fractions $W_g$ for SN, DN, and TN rubbers formed at various $w_R$. Standard deviations are in parenthesis.

| Code | $w_R$ | $W_g$ |
|---|---|---|
| SN | 0 | 1.0 (0.1) |
| DN | 0.45 (0.03) | 1.08 (0.02) |
| DN | 0.85 (0.05) | 1.03 (0.04) |
| DN | 1.35 (0.08) | 1.02 (0.01) |
| DN | 1.9 (0.2) | 1.02 (0.01) |
| TN | 4.5 (0.4) | 0.94 (0.04) |

Figure 4.2b shows the porosity $P$ calculated using eq 4.6, and the total pore volume $V_p$ calculated from the uptake of the poor solvent methanol plotted against the ratio of the network components $w_R$. The porosity and the total pore volume decrease from 85 to 70% and from 7.9 to 2.6 mL.g$^{-1}$, respectively, as $w_R$ is increased from 0 to 4.5. Thus, the higher the $w_R$ ratio, the lower is the porosity, indicating partial filling of the pores in SN and DN rubbers with the second and third network components, respectively. The results also reveal a significant effect of double- and triple-networking on the porosity of the rubbers.

To visualize the porous structure of the rubbers, SEM and μ-CT techniques were used where the former provides a greater magnification and more accurate measurement of the pore sizes than μ-CT. μ-CT measurements were conducted on rubber specimens in

the family tree starting with SN, going through DN with $w_R$ = 1.9 to the TN with $w_R$ = 4.5. Figure 4.2c shows typical two-dimensional (2D) and 3D μ-CT images of SN, DN, and TN rubbers formed at $w_R$ = 0, 1.9, and 4.5, respectively (scale bars = 1 mm). The SN rubber has, in addition to micrometer-sized pores, millimeter-sized very large pores (large black areas in the image), which decrease in size and finally disappear after its double- and triple-networking.

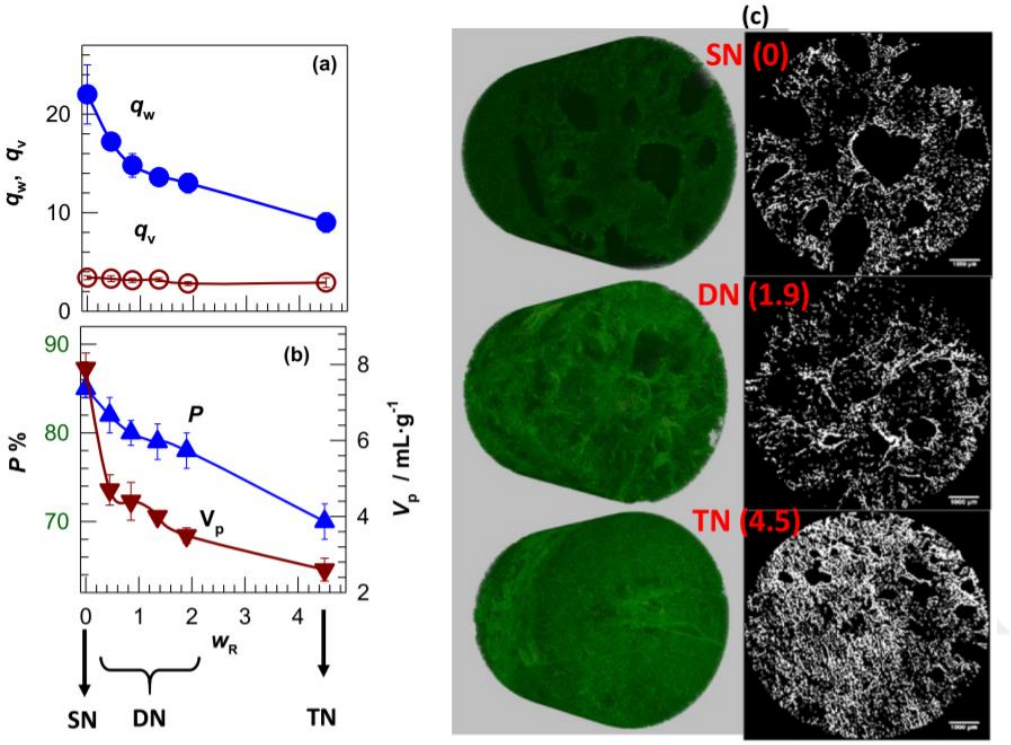


**Figure 4.2 :** (a,b) Equilibrium weight $q_w$ (filled circles) and volume swelling ratios $q_v$ (open circles), the total porosity $P$ (triangles up), and pore volume $V_p$ (triangles down) of macroporous rubbers plotted against $w_R$ ratio. (c) 3D (left) and 2D μ-CT images (right) of SN, DN, and TN rubbers formed at $w_R$ ratios shown in the parenthesis. Scale bars are 1 mm.

The size distributions of the pores in SN, DN, and TN rubbers given in Figure 4.3a support this finding; the volume fraction of millimeter-sized pores decreases after double- and triple networking and a new generation of pores appears at around 30 μm. For instance, the volume fractions of the pores between 13 and 45 μm are 0.2, 5, and 11% for SN, DN, and TN with $w_R$ = 0, 1.9, and 4.5, respectively. The total porosities estimated from μ-CT analysis are 95, 84, and 74% for SN, DN, and TN, respectively, and hence show a similar trend as estimated from the swelling ratios using eq 4.6 and pore volume measurements (Figure 4.2b). Moreover, μ-CT results also reveal that there are no closed pores in all rubbers, which is an important requirement for their

applications in absorption processes. The thicknesses of the pore walls are 30 ± 7, 39 ± 15, and 44 ± 16 μm for SN, DN, and TN rubbers, respectively, that is, it increases with increasing number of the network components.

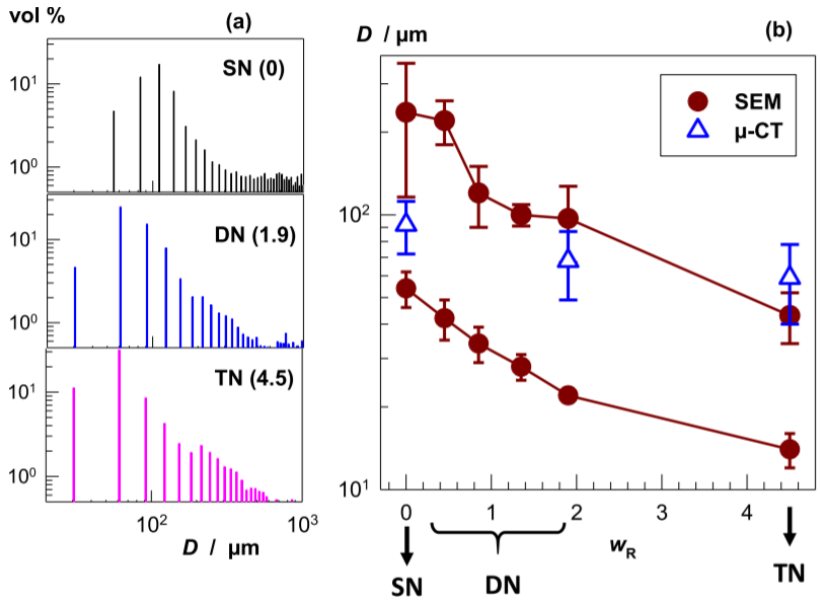


**Figure 4.3 :** (a) Pore size distributions estimated from μ-CT analysis of SN, DN, and TN rubbers with $w_R$ ratios shown in the parenthesis. (b) Average pore diameters $D$ of rubbers from μ-CT (open triangles) and SEM analysis (filled circles) plotted against $w_R$.

Figure 4.4 shows SEM images of SN, DN, and TN rubbers with various $w_R$ ratios as indicated. The structure consists of micrometer-sized irregular pores whose average size decreases while the pore walls become thicker as the $w_R$ ratio is increased. Filled circles in Figure 4.3b show the average pore diameters $D$ estimated by analyzing SEM images plotted against $w_R$ ratio. We observed two generations of pores in all rubbers, namely, large and small pores with diameters 40-240 and 14-54 μm, respectively. The average diameters of both large and small pores decrease, and they approach each other as $w_R$ is increased. For instance, in the family tree starting with SN through DN to the TN with $w_R$ = 0, 1.9, and 4.5, respectively, the average diameter $D$ of the large pores decreases from 236 ± 120 through 97 ± 30 to 43 ± 9 μm, revealing filling of the large pores in SN with the second and third network components and formation of more monodisperse pores. Small pores in the rubbers show a similar trend and $D$ first decreases from 54 ± 8 to 22 ± 1 μm and then to 14 ± 2 μm after double- and triple-networking, respectively.

We have to mention that the large polydispersity of the pores in SN rubber is due to the coexistence of two mechanisms for the formation of pores during cryogelation [57]. The first mechanism is the presence of solvent crystals acting as a template for the formation of micrometer-sized pores. The second is the macro-phase separation of IIR at low temperature at which benzene becomes a poor solvent for IIR, which leads to the formation of micrometer- to millimeter-sized pores [57]. The appearance of more regular pores in both DN and TN reflects the filling of large pores with the second and third network components. Open symbols in Figure 4.3b representing the $w_R$ ratio dependence of the pore diameters less than 150 μm estimated by CT gives a similar trend with the SEM results but slightly larger diameters. We have to mention that the μ-CT technique calculates the pore sizes from the number of pixels in the pores. Because the pixel resolution is 15 μm, μ-CT estimates the pore sizes at least 15 μm higher as compared to SEM, which is also reflected in higher total porosities.

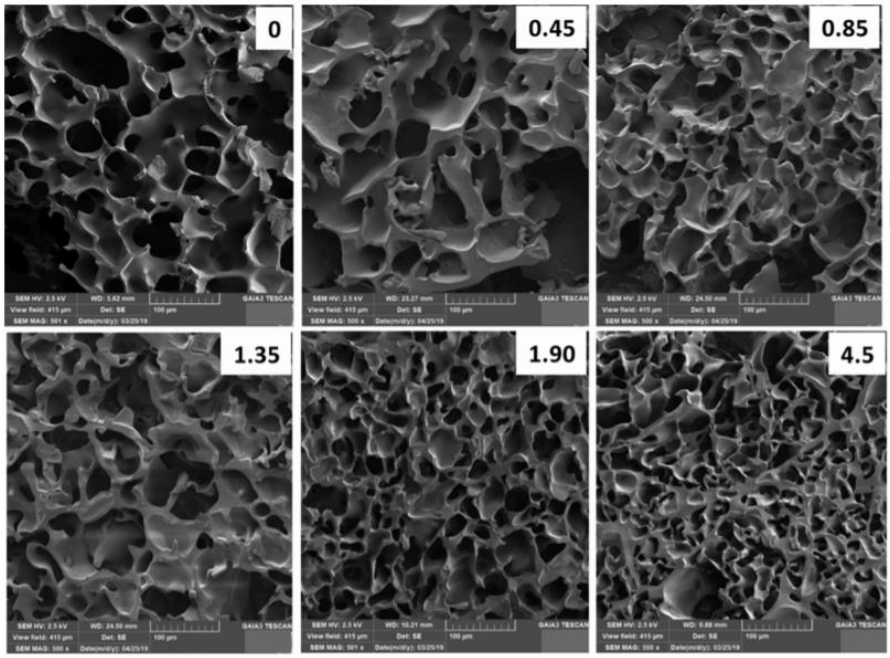


**Figure 4.4 :** SEM images of macroporous SN, DN, and TN rubbers formed at various $w_R$ ratios indicated. Scale bars are 100 μm.

### 4.2.2 Mechanical properties

The mechanical properties of the rubbers were determined by uniaxial elongation and compression tests at 23 ± 2 °C. The measurements revealed reversible deformation and high stretchability of all rubbers. For instance, the images in Figure 4.5a present a TN rubber specimen during stretching up to 300%. After stretching and unloading, the specimen recovers its initial length without any permanent deformation. Figure 4.5b,c

shows tensile and compressive stress−strain curves of the rubbers with various $w_R$, respectively. All rubbers sustain 300-500% elongation ratios and 50-190 kPa tensile stresses. Young's modulus $E$, the tensile $\sigma_{f,t}$, and compressive fracture stresses $\sigma_{f,c}$ of the rubbers are shown in Figure 4.6a as a function of the weight ratio $w_R$ of the network components. The mechanical performance of the rubbers significantly improves with increasing $w_R$ ratio of the network components. For instance, the modulus $E$ and compressive fracture stress $\sigma_{f,c}$ increase by 5 and 9 folds, respectively, as $w_R$ is increased from 0 to 4.5. TN rubbers prepared at the highest $w_R$ ratio have the highest modulus $E$ (0.11 ± 0.01 MPa) and can sustain 0.19 and 37 ± 6 MPa tensile and compressive stresses, respectively.

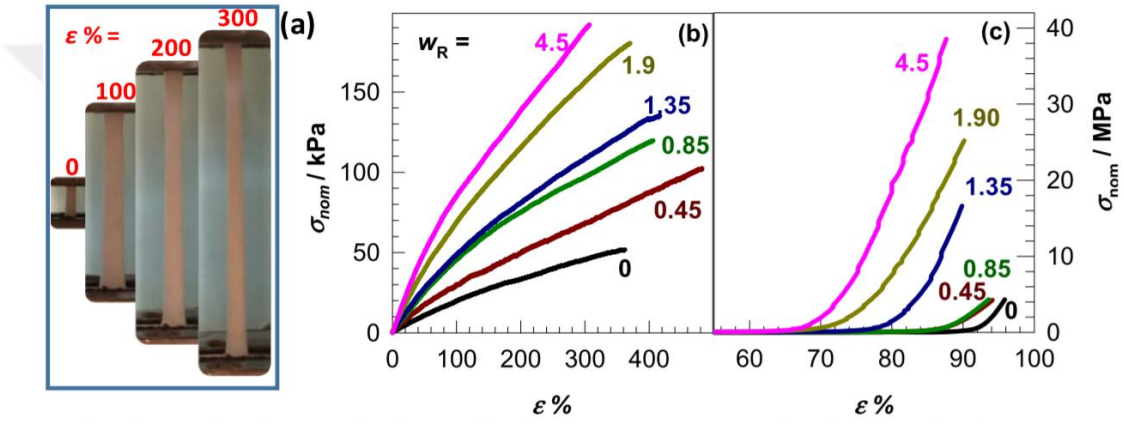


**Figure 4.5:** (a) Images of a TN rubber specimen during the elongation tests. (b,c) Typical tensile (b) and compressive nominal stress ($\sigma_{nom}$)−strain ($\varepsilon$) curves of the rubbers (c). The mass ratios $w_R$ of the network components are indicated.

To determine the fatigue resistance of the rubbers against deformation, cyclic compression tests at a constant strain rate of 5 $min^{-1}$ were performed by loading the samples up to 80% strain and then unloading. This loading and unloading cycle was repeated 9 times with a waiting time of 1 min between the cycles. The results are shown in Figure 4.6b for a TN rubber specimen where the loading and unloading curves are shown by the solid and dotted curves, respectively. Each loading or unloading curve exactly follows the previous one revealing reversibility of the cycles and self-recoverability of the rubber. This behavior is also illustrated in the inset to the figure, which is a zoom-in to the first and last cycles between 0 and 18% strains. Indeed, the hysteresis energy $U_{hys}$, that is, the area between the loading and unloading curves, is independent on the number of cycles and remains at 6.07 ± 0.05 $kJ.m^{-3}$. Because $U_{hys}$ corresponds to the energy dissipated due to the damage in the microstructure [121], this reveals recovery of the original microstructure after the waiting time of 1 min.

Thus, owing to the self-recovery ability of the rubbers, they have a high fatigue resistance against repeated deformations.

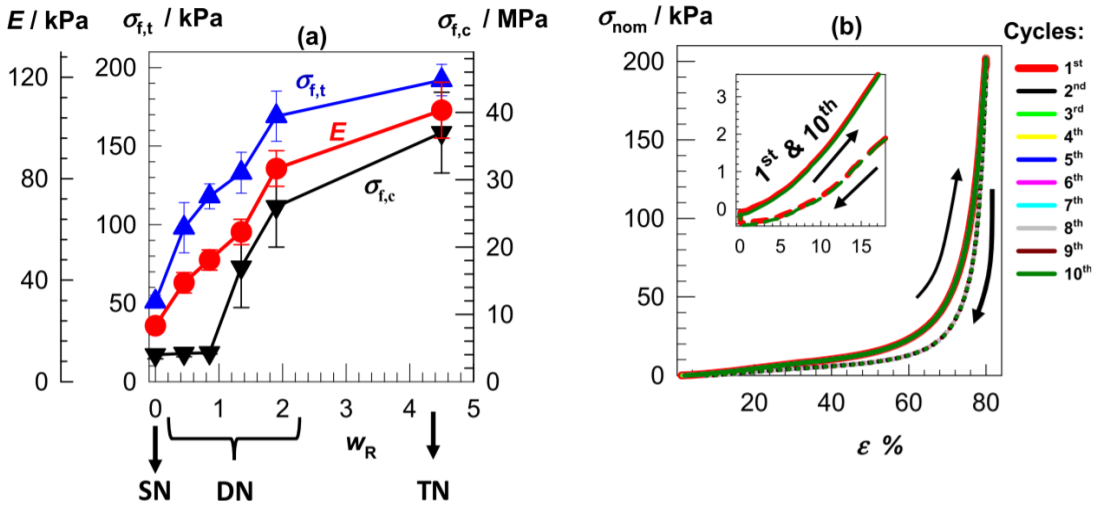


**Figure 4.6 :** (a) Modulus $E$, tensile $\sigma_{f,t}$, and compressive fracture stresses $\sigma_{f,c}$ of the rubbers shown as a function of the $w_R$ ratio. (b) Ten successive loading and unloading cycles conducted on a TN rubber specimen. The loading and unloading curves are shown by solid and dotted curves, respectively. The inset is a zoom-in to the first and last cycles between 0 and 18% strains.

### 4.2.3 Sorption of PAHs

SN, DN, and TN rubbers with $w_R$ ratios of 0, 1.9, and 4.5, respectively, with different porosities (85-70%), pore volumes (7.9-2.6 $mL.g^{-1}$), and pore sizes and size distributions were selected for the sorption experiments together with nonporous PDMS as the reference material.

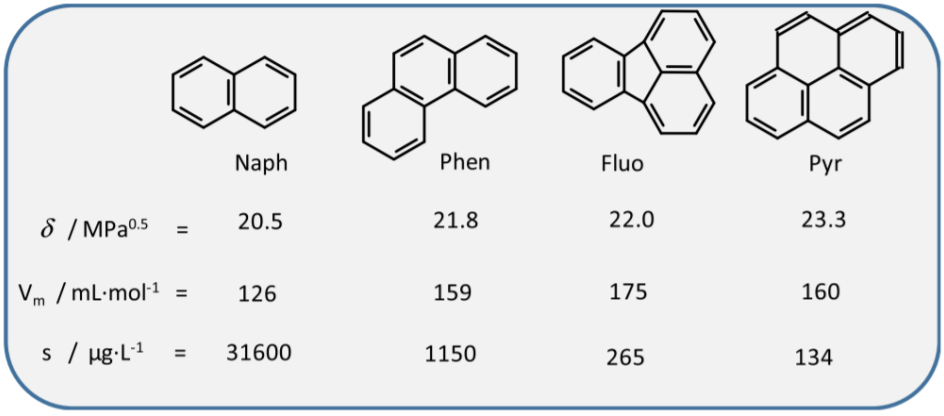


**Figure 4.7:** Structure, Solubility Parameter $\delta$, Molar Volume $V_m$, and Water Solubility $s$ at 25 °C of Naphthalene (Naph), Phenanthrene (Phen), Fluoranthene (Fluo), and Pyrene (Pyr).

Sorption experiments were carried out using four PAHs, namely, phenanthrene (Phen), naphthalene (Naph), pyrene (Pyr), and fluoranthene (Fluo), whose structures are shown in Figure 4.7 together with their solubility parameters $\delta$, molar volumes $V_m$, and water solubilities $s$ at 25 °C. The PAH compounds have two to four aromatic rings and exhibit solubility parameters between 20.5 and 23.3 $MPa^{0.5}$, which are closer to IIR than PDMS (16.8 vs 14.9 $MPa^{0.5}$), revealing that these PAHs would have stronger interactions with IIR than PDMS. Two sets of sorption experiments were conducted by placing the rubber specimens in aqueous solutions of PAHs in filtered seawater with a salinity of 22 ppt. In the first set, the concentration of PAH in the solution was monitored up to 12 h to highlight the initial uptake rate of the rubbers. In the second set, cumulative PAH concentration in the rubber specimens was monitored over 30-40 days by refreshing PAH solutions every day. Figure 4.8a shows the variations of the concentrations $C_t$ of Naph, Phen, Fluo, and Pyr as a function of the contact time $t$ during the first 12 h of sorption experiments.

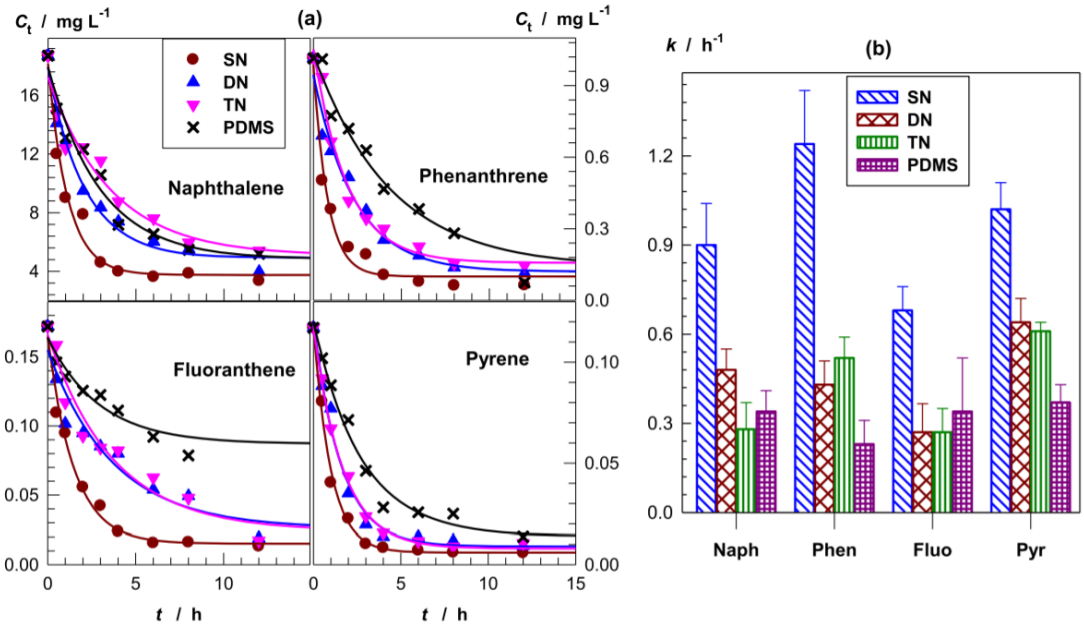


**Figure 4.8:** (a) Experimental data during the first 12 h of the sorption tests (symbols) and the results of curve fitting using eq 4.7 (curves). (b) Rate constant $k$ of the sorption process as a function of the types of rubbers and PAHs.

The SN rubber most rapidly absorbs all the PAHs studied from the solution and the total absorbed amount of each PAH is the highest as compared to other rubbers, which is attributed to its largest porosity and pore volume. If we assume that the decay of PAH concentration with time follows a first-order kinetics, the sorption process by the macroporous rubbers can be written as [122,123]

$$\frac{d_{qt}}{d_t} = k(q_e - q_t) \tag{4.7}$$

where $q_e$ and $q_t$ represent the PAH amounts absorbed at equilibrium and time $t$, respectively, and $k$ is the rate constant. Solution of eq 4.7 gives

$$C_t = C_0 - C_{eq}(1 - e^{-kt}) \tag{4.8}$$

where $C_0$, $C_t$, and $C_{eq}$ are PAH concentrations in the solution at time zero, time $t$, and equilibrium, respectively. The results of curve fitting using eq 4.7 for four different PAHs are shown in Figure 4.8a by the curves. A good agreement between the experimental and predicted values of eq 4.7 is seen from the figures. We have to mention that a second-order kinetics in the form of $d_{qt}/d_t = k'(q_e - q_t)^2$ results in a similar fit to the experimental data (Figure 4.9).

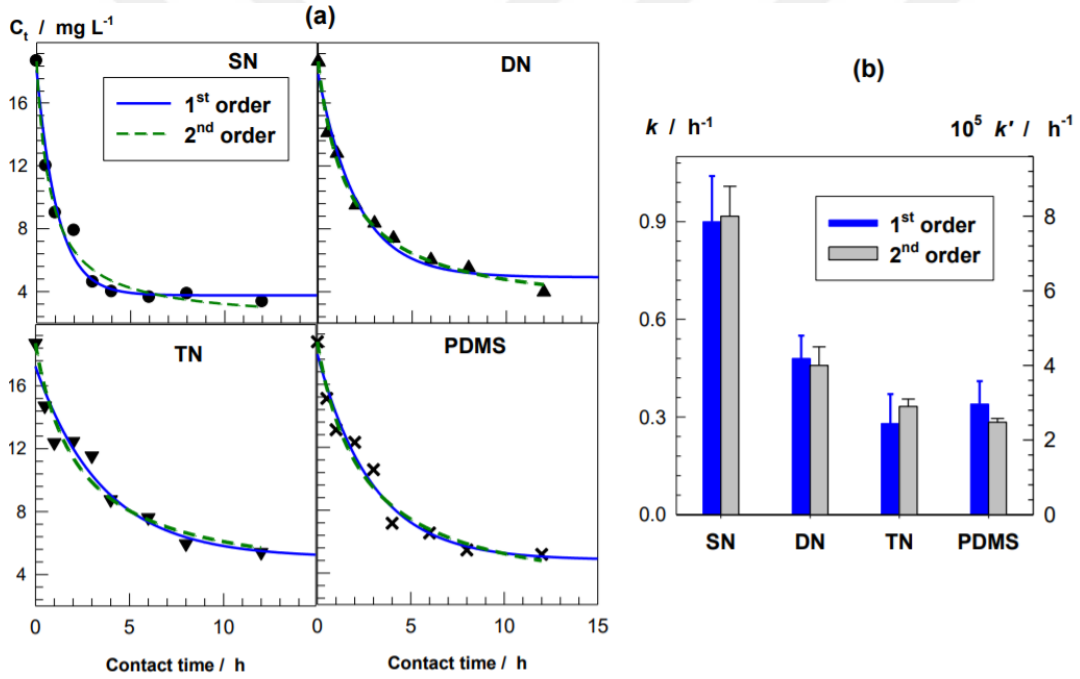


**Figure 4.9:** (a): Experimental data from naphthalene sorption tests from aqueous solutions during the first 12 h (symbols), and the results of curve fitting using the first (solid curves) and second order sorption kinetics (dashed curves). (b): The rate constant $k$ and $k'$ of the naphthalene sorption process estimated from 1st and 2nd order kinetics, respectively, as a function of the type of rubbers. For the second order kinetics, the equation $d_{qt}/d_t = k'(q_e - q_t)^2$ was used in the calculations which leads to $C_t = C_0 - t/(a+bt)$ where $a = (aq_e^2)^{-1}$ and $b = q_e^{-1}$.

The rate constants $k$ extracted from the first-order fits are compiled in Figure 4.8b for four PAHs and four rubbers. SN exhibits the highest rate constant $k$ for all PAHs. The average $k$ values for all PAHs are 1.0 ± 0.2, 0.46 ± 0.15, 0.42 ± 0.06, and 0.32 ± 0.06 for SN, DN, TN, and PDMS, respectively, that is, it decreases in the order SN > DN >

TN > PDMS. Thus, the larger the total volume of the pores, the faster is the rate of absorption of PAHs from aqueous solutions.

Results of longtime experiments up to 30-40 days are shown in Figure 4.10a-d where the absorbed amount of Naph, Phen, Fluo, and Pyr, respectively, by 1 g of rubber ($w_t$) is plotted against the contact time *t*.

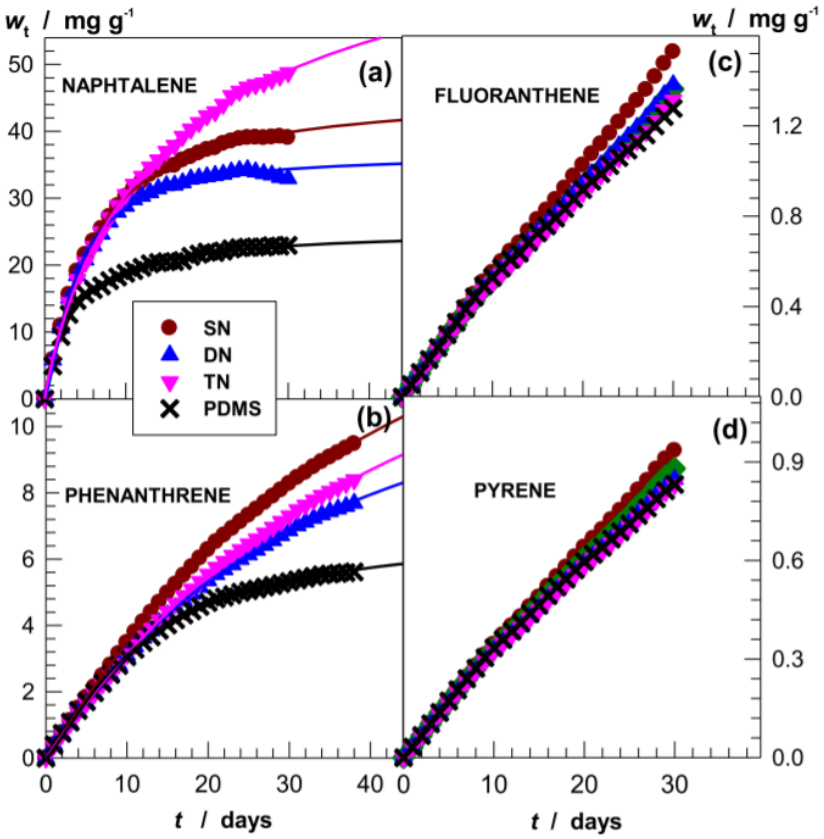


**Figure 4.10:** Absorbed amount of Naph (a), Phen (b), Fluo (c), and Pyr (d) by 1 g of rubber sorbent ($w_t$) plotted against the contact time *t*. Experimental data are represented by symbols, while the curves in (a,b) are the results of curve fitting using eq 4.9.

Because of very low water solubilities of Fluo and Pyr (Figure 4.7), their experimental $w_t$ versus time data were still in the initial linear regime after 30 days of monitoring so that their saturated concentrations cannot be estimated. Long-term data obtained from the solutions of Naph and Phen could be well fitted to the modified Hill equation [124-128]

$$w_t = w_{eq} \frac{t^n}{t^n + t_{1/2}{}^n} \tag{4.9}$$

where $w_{eq}$ is the absorbed amount of PAH at equilibrium, that is, at the final steady-state PAH concentration, $t_{1/2}$ is the half equilibrium time at which $w_t = w_{eq}/2$, and the

exponent *n* was found to be independent on the types of rubbers and PAHs and equals to 1.1 ± 0.2. The curves in Figure 4.10a,b showing the results of curve fitting reveal that eq 4.9 can be used to quantitatively characterize the sorption kinetics of PAHs. Such perfect modeling the shape of the time-dependent PAH concentration variations is of prime importance in predicting the long-term properties of passive samplers. To the best of our knowledge, eq 4.9 has not been used in such applications.

Figure 4.11 presents the amount of Naph and Phen absorbed at equilibrium $w_{eq}$ together with the half-equilibrium time $t_{1/2}$ as a function of the types of rubbers and PAHs. PDMS with a nonporous structure exhibits the lowest absorption capacity for both Naph and Phen. This highlights the importance of a macroporous structure for materials to be used as passive samplers. Moreover, the TN sorbent with the smallest pores and porosity among the macroporous rubbers absorbs the highest amount of Naph. Thus, although the initial sorption rate of TN for PAHs is slow, it is capable of absorbing a large amount of Naph from aqueous solutions. This interesting finding can be attributed to the opposite effect of the pore size on the sorption rate and sorption capacity. Although a large pore size and a high porosity of around 90% provide rapid sorption of PAHs at short times as observed by the SN rubber, at longer contact times, PAHs located in the large pores can easily diffuse out of the rubber phase because of their large water contents. This finding shows a significant effect of the pore morphology of passive samplers in their efficiency in short- and long-time field applications. We have to note that the lower absorption capacity of DN as compared to that of SN can be attributed to its smaller pore volume (3.5 vs 7.9 $mL.g^{-1}$) and lower volume fraction of its pores between 13 and 45 μm as compared to TN (5 vs 11%).

Figure 4.11 also shows that the half-equilibrium time $t_{1/2}$ of TN in Naph solution is 17 ± 1 days, which is 3- to 5-fold longer than the other sorbents. This means that the TN sorbent can be used for long-time monitoring of PAHs in aquatic systems. Moreover, when the sorption tests are conducted with Phen instead of Naph, the absorption capacity of SN approaches to that of TN (Figure 4.11). This behavior is attributed to 30-times lower water solubility of Phen as compared to that of Naph, which provides its accumulation in the hydrophobic sorbent phase instead of water (Figure 4.7). We have to note that the PAH compounds used in the absorption tests have solubility parameters $\delta$ between 20.5 and 23.3 $MPa^{0.5}$ as compared to $\delta$ = 16.8 $MPa^{0.5}$ reported for IIR [116]. Thus, rubber sorbents with $\delta$ values closer to PAHs than IIR such as cis-

polybutadiene and styrene–butadiene rubber with $\delta$ = 18.0 and 18.1 $MPa^{0.5}$, respectively [129], would have a higher sorption capacity for PAHs as compared to that for the IIR sorbent.

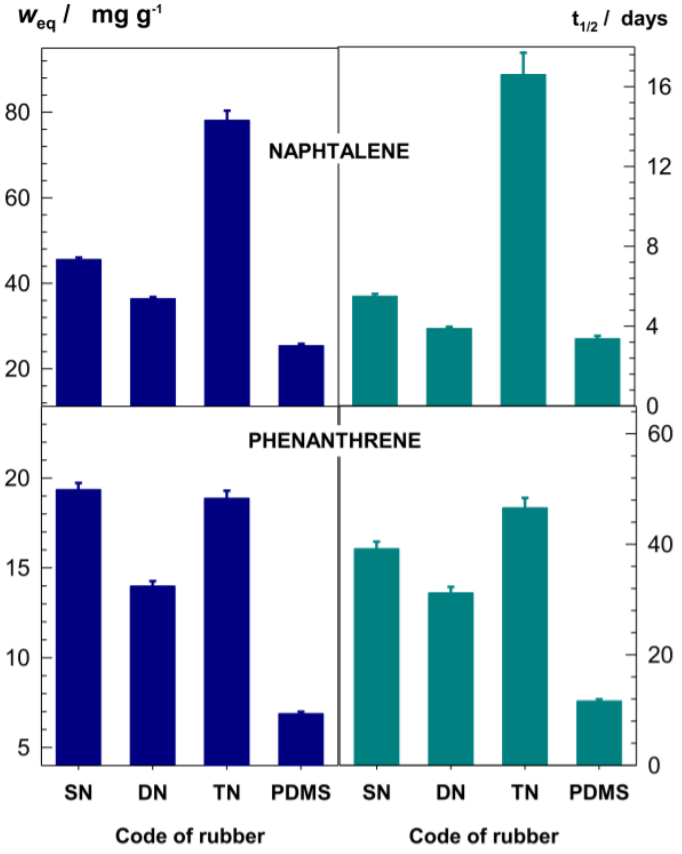


**Figure 4.11:** Sorbed amount of PAH at equilibrium $w_{eq}$ and the half equilibrium time $t_{1/2}$ as a function of the types of sorbents and PAHs.

### 4.3 Conclusions

Passive sampling is an efficient technique for monitoring the dissolved concentration of PAHs in aquatic systems. We presented here a series of novel macroporous rubber sorbents as single-phase passive samplers with tunable pore morphologies, extraordinary mechanical properties, and high sorption rates and capacities for PAHs. Sorbent materials based on SN, DN, and TN butyl rubber were prepared via cryogelation technique from butyl rubber solutions in benzene as the solvent at -18 °C using a $S_2Cl_2$ cross-linker. To obtain rubber sorbents with DN and TN structures, cryogelation reactions were conducted within the pores of SN and DN rubber networks, respectively. The porosity, average pore diameter, and mechanical properties including the modulus and fracture stress could be tuned by adjusting the weight ratio $w_R$ of the network components. Increasing $w_R$ ratio decreases both the

average pore diameter and the total porosity of the rubbers, whereas their mechanical properties significantly increase. Four PAH compounds, namely, Naph, Phen, Fluo, and Pyr, with two to four aromatic rings were used to highlight the relations between the properties of macroporous rubber sorbents and their absorption rates and capacities for the PAHs. It was shown that the nonporous PDMS rubber reported before as a passive sampler has the lowest absorption rate and absorption capacity as compared to macroporous rubber sorbents presented here. The SN rubber sorbent absorbs most rapidly PAHs which are attributed to its largest porosity and pore volume. Moreover, the TN sorbent has the highest sorption capacity because of its smaller pores and low porosity, preventing the escape of PAHs from the sorbent to the solution phase. The present experimental studies with PAHs highlight the potential use of SN and TN monophasic macroporous rubber sorbents in monitoring studies of surface waters. However, we should note that it is necessary to determine the sorbent-water partition coefficients and in situ sampling rates. The rubber sorbents should also be tested in the field to see the spectrum of the substances accumulated in and compared with those used widely as passive samplers. The deployment protocols of the rubber sorbents to the monitoring sites should also be clearly defined.

## 5. CONCLUSIONS

Cryogels are unique 3D polymeric materials possessing high mechanical strength and interconnected macroporous architecture. They can be easily fabricated by exposing a suitable reaction system to subzero temperatures, in which dissolved reactants are expelled from the frozen solvent and concentrated to form unfrozen microdomains. While gelation reactions occur in these liquid regions where the reactant concentrations are dramatically higher than that of the initial state, frozen solvent crystals act as a template forming micrometer-sized interconnected pores.

Within the scope of the thesis, silk fibroin (SF) hydro-cryogels and butyl rubber (IIR) organo-cryogels were fabricated from their aqueous and organic solutions, respectively. After isolation of the SF protein from *Bombyx Mori* silkworm cocoons, its aqueous solutions containing butanediol diglycidyl ether as chemical cross-linker and *N,N,N′,N′*-tetramethylethylenediamine as pH regulator, were exposed to unidirectional freezing – cryogelation for the preparation of the hydro-cryogels. Firstly, plastic reactors containing SF aqueous reaction solutions were directly immersed in liquid nitrogen at various immersion rates, and several SF cryogels possessing radially-aligned pore morphology were obtained. Those cryogel scaffolds exhibited Young's modulus in the range of MPa and they sustained up to 20 MPa compressive stresses. In addition to high mechanical strength, they also exhibited anisotropic mechanical properties due to the alignment of the pores, e.g., the Young's modulus ($E$) was $3.4 \pm 0.5$ MPa and $0.8 \pm 0.3$ MPa when measured along the directions parallel and vertical to the freezing direction, respectively. Then, to increase the anisotropy ratio, i.e. to generate the pore alignment as longitudinally rather than radially, a different experimental set-up consisting of a copper bottom plate and a cylindrical polytetrafluoroethylene (PTFE) mold were used to fabricate anisotropic SF cryogels. The copper bottom plate was immersed in a cold bath at -30 or -196 °C, whereas the cylindrical PTFE mold locating outside of the cold bath was filled with aqueous solutions of SF of various concentrations. Unidirectionally frozen SF solutions were then subjected to cryogelation at -18 °C. Obtained cryogel scaffolds by

this set up exhibited the highest modulus anisotropy so far reported to our knowledge, i.e. 21 ± 5, with Young's moduli $E$ = 2.3 ± 0.5 and 0.11 ± 0.03 MPa measured along parallel and perpendicular to the freezing direction, respectively. Moreover, independent on the fibroin concentration or direction of the measurements, 60% of the mechanical energy given to the cryogels are dissipated due to the friction between the fibroin pore walls, which is responsible for their squeezability and self-recoverability.

As a passive sampler sorbent material, IIR-based organo-cryogels with single (SN), double (DN) and triple (TN) network structures were synthesized by using benzene solutions of IIR containing $S_2Cl_2$ cross-linker. To obtain rubber sorbents with DN and TN structures, cryogelation reactions were conducted within the pores of SN and DN dry rubber cryogel networks, respectively. This successive cryogelations endowed that the rubber organo-cryogels have extraordinary mechanical toughness and adjustable pore distributions. It was also shown that these IIR-based organo-cryogels can be used as an efficient passive sampler for polycyclic aromatic hydrocarbons (PAHs). For instance, SN rubber sorbent absorbed most rapidly PAHs which are attributed to its largest porosity and pore volume. On the other hand, TN sorbent had the highest sorption capacity because of its smaller pores and low porosity, preventing the escape of PAHs from the sorbent to the solution phase at longer time scales.

## REFERENCES


[1] **Johnson, B. R., & Lam, S. K.** (2010). Self-organization, natural selection, and evolution: Cellular hardware and genetic software., *Bioscience*, *60*(11), 879-885.

[2] **Burla, F., Mulla, Y., Vos, B. E., Aufderhorst-Roberts, A., & Koenderink, G. H.** (2019). From mechanical resilience to active material properties in biopolymer networks. *Nat. Rev. Phys.*, *1*(4), 249-263.

[3] **Tseng, Y., Kole, T. P., Lee, J. S., Fedorov, E., Almo, S. C., Schafer, B. W., & Wirtz, D.** (2005). How actin crosslinking and bundling proteins cooperate to generate an enhanced cell mechanical response. *Biochem. Bioph Res Co.*, *334*(1), 183-192.

[4] **Fletcher, D. A., & Mullins, R. D.** (2010). Cell mechanics and the cytoskeleton. *Nature*, *463*(7280), 485-492.

[5] **Smith-Mungo, L. I., & Kagan, H. M.** (1998). Lysyl oxidase: properties, regulation and multiple functions in biology. *Matrix Biol.*, *16*(7), 387-398.

[6] **Kagan, H. M., & Li, W.** (2003). Lysyl oxidase: properties, specificity, and biological roles inside and outside of the cell. *J. Cell. Biochem.*, *88*(4), 660-672.

[7] **Abdel-Wahab, A. A., Alam, K., & Silberschmidt, V. V.** (2011). Analysis of anisotropic viscoelastoplastic properties of cortical bone tissues. *J. Mech. Behav. Biomed.*, *4*(5), 807-820.

[8] **Annaidh, A. N., Bruyère, K., Destrade, M., Gilchrist, M. D., & Otténio, M.** (2012). Characterization of the anisotropic mechanical properties of excised human skin. *J. Mech. Behav. Biomed.*, *5*(1), 139-148.

[9] **Lakhani, P., Dwivedi, K. K., & Kumar, N.** (2020). Directional dependent variation in mechanical properties of planar anisotropic porcine skin tissue. *J. Mech. Behav. Biomed.*, *104*, 103693.

[10] **Iyo, T., Maki, Y., Sasaki, N., & Nakata, M.** (2004). Anisotropic viscoelastic properties of cortical bone. *J. Biomech.37*(9), 1433-1437.

[11] **Kopeček, J., & Yang, J. (2007).** Hydrogels as smart biomaterials. *Polym. Int.*, *56*(9), 1078-1098.

[12] **Hoare, T. R., & Kohane, D. S.** (2008). Hydrogels in drug delivery: Progress and challenges. *Polymer*, *49*(8), 1993-2007.

[13] **Qu, J., Zhao, X., Liang, Y., Zhang, T., Ma, P. X., & Guo, B.** (2018). Antibacterial adhesive injectable hydrogels with rapid self-healing, extensibility and compressibility as wound dressing for joints skin wound healing. *Biomaterials*, *183*, 185-199.

[14] **Drury, J. L., & Mooney, D. J.** (2003). Hydrogels for tissue engineering: scaffold design variables and applications. *Biomaterials*, *24*(24), 4337-4351.

[15] **Creton, C.** (2017). 50th anniversary perspective: networks and gels: soft but dynamic and tough. *Macromolecules*, *50*(21), 8297-8316.

[16] **Webber, R. E., Creton, C., Brown, H. R., & Gong, J. P.** (2007). Large strain hysteresis and mullins effect of tough double-network hydrogels. *Macromolecules*, *40*(8), 2919-2927.

[17] **Gong, J. P., Katsuyama, Y., Kurokawa, T., & Osada, Y.** (2003). Double-network hydrogels with extremely high mechanical strength. *Adv. Mater.*, *15*(14), 1155-1158.

[18] **Ding, F., Zou, Y., Wu, S., & Zou, X.** (2020). Self-healing and tough hydrogels with conductive properties prepared through an interpenetrating polymer network strategy. *Polymer*, *206*, 122907.

[19] **Haraguchi, K., & Takehisa, T.** (2002). Nanocomposite hydrogels: A unique organic–inorganic network structure with extraordinary mechanical, optical, and swelling/de-swelling properties. *Adv. Mater.*, *14*(16), 1120-1124.

[20] **Okumura, Y., & Ito, K.** (2001). The polyrotaxane gel: A topological gel by figure-of-eight cross-links. *Adv. Mater.*, *13*(7), 485-487.

[21] **Memic, A., Colombani, T., Eggermont, L. J., Rezaeeyazdi, M., Steingold, J., Rogers, Z. J., ... & Bencherif, S. A.** (2019). Latest advances in cryogel technology for biomedical applications. *Adv. Ther.*, *2*(4), 1800114.

[22] **Muslumova, S., Yetiskin, B., & Okay, O.** (2019). Highly Stretchable and Rapid Self-Recoverable Cryogels Based on Butyl Rubber as Reusable Sorbent. *Gels*, *5*(1), 1.

[23] **Melke, J., Midha, S., Ghosh, S., Ito, K., & Hofmann, S.** (2016). Silk fibroin as biomaterial for bone tissue engineering. *Acta Biomater.*, *31*, 1-16.

[24] **Okay, O.** (2009). General properties of hydrogels. In *Hydrogel sensors and actuators* (pp. 1-14). Springer, Berlin, Heidelberg.

[25] **Ahn, A. C., & Kaptchuk, T. J.** (2011). Spatial anisotropy analyses of subcutaneous tissue layer: potential insights into its biomechanical characteristics. *J. Anat.*, *219*(4), 515-524.

[26] **Williams, L. N., Elder, S. H., Bouvard, J. L., & Horstemeyer, M. F.** (2008). The anisotropic compressive mechanical properties of the rabbit patellar tendon. *Biorheology*, *45*(5), 577-586.

[27] **Jurvelin, J. S., Buschmann, M. D., & Hunziker, E. B.** (2003). Mechanical anisotropy of the human knee articular cartilage in compression. *P. I. Mech. Eng. H.*, *217*(3), 215-219.

[28] **Nerurkar, N. L., Elliott, D. M., & Mauck, R. L.** (2010). Mechanical design criteria for intervertebral disc tissue engineering. *J. Biomec.*, *43*(6), 1017-1030.

[29] **Jayasuriya, A. C., Ghosh, S., Scheinbeim, J. I., Lubkin, V., Bennett, G., & Kramer, P.** (2003). A study of piezoelectric and mechanical anisotropies of the human cornea. *Biosens. Bioelectron.*, *18*(4), 381-387.

[30] **Zhang, H., & Cooper, A. I.** (2007). Aligned porous structures by directional freezing. *Adv. Mater.*, *19*(11), 1529-1533.

[31] **Zhang, H., Hussain, I., Brust, M., Butler, M. F., Rannard, S. P., & Cooper, A. I.** (2005). Aligned two-and three-dimensional structures by directional freezing of polymers and nanoparticles. *Nat. Mater.*, *4*(10), 787-793.

[32] **Millon, L. E., Mohammadi, H., & Wan, W. K.** (2006). Anisotropic polyvinyl alcohol hydrogel for cardiovascular applications. *J. Biomed. Mater. Res. B.*, *79*(2), 305-311.

[33] **Wan, W., Bannerman, A. D., Yang, L., & Mak, H.** (2014). Poly (vinyl alcohol) cryogels for biomedical applications. *Adv. Polym. Sci.*, 283-321.

[34] **Chatelin, S., Bernal, M., Deffieux, T., Papadacci, C., Flaud, P., Nahas, A., ... & Pernot, M.** (2014). Anisotropic polyvinyl alcohol hydrogel phantom for shear wave elastography in fibrous biological soft tissue: a multimodality characterization. *Phys. Med. Biol.*, *59*(22), 6923.

[35] **Voge, C. M., Kariolis, M., MacDonald, R. A., & Stegemann, J. P.** (2008). Directional conductivity in SWNT-collagen-fibrin composite biomaterials through strain-induced matrix alignment. *J. Biomed. Mater. Res. A.*, *86*(1), 269-277.

[36] **Osorio-Madrazo, A., Eder, M., Rueggeberg, M., Pandey, J. K., Harrington, M. J., Nishiyama, Y., ... & Burgert, I.** (2012). Reorientation of cellulose nanowhiskers in agarose hydrogels under tensile loading. *Biomacromolecules*, *13*(3), 850-856.

[37] **Swan, M. C., Bucknall, D. G., Goodacre, T. E. E., & Czernuszka, J. T.** (2011). Synthesis and properties of a novel anisotropic self-inflating hydrogel tissue expander. *Acta Biomater.*, *7*(3), 1126-1132.

[38] **Yang, W., Furukawa, H., & Gong, J. P.** (2008). Highly extensible double-network gels with self-assembling anisotropic structure. *Adv. Mater.*, *20*(23), 4499-4503.

[39] **Haque, M. A., Kamita, G., Kurokawa, T., Tsujii, K., & Gong, J. P.** (2010). Unidirectional alignment of lamellar bilayer in hydrogel: one-dimensional swelling, anisotropic modulus, and stress/strain tunable structural color. *Adv. Mater.*, *22*(45), 5110-5114.

[40] **Pei, X., Zan, T., Li, H., Chen, Y., Shi, L., & Zhang, Z.** (2015). Pure anisotropic hydrogel with an inherent chiral internal structure based on the chiral nematic liquid crystal phase of rodlike viruses. *ACS Macro Lett.*, *4*(11), 1215-1219.

[41] **Ahadian, S., Ramón-Azcón, J., Estili, M., Liang, X., Ostrovidov, S., Shiku, H., ... & Khademhosseini, A.** (2014). Hybrid hydrogels containing vertically aligned carbon nanotubes with anisotropic electrical conductivity for muscle myofiber fabrication. *Sci. Rep.*, *4*(1), 1-11.

[42] **Walker, K. J., & Madihally, S. V.** (2015). Anisotropic temperature sensitive chitosan-based injectable hydrogels mimicking cartilage matrix. *J. Biomed. Mater. Res. B.*, *103*(6), 1149-1160.

[43] **Hockaday, L. A., Kang, K. H., Colangelo, N. W., Cheung, P. Y. C., Duan, B., Malone, E., ... & Butcher, J. T.** (2012). Rapid 3D printing of anatomically accurate and mechanically heterogeneous aortic valve hydrogel scaffolds. *Biofabrication*, *4*(3), 035005.

[44] **Zhang, L., Zhao, J., Zhu, J., He, C., & Wang, H.** (2012). Anisotropic tough poly (vinyl alcohol) hydrogels. *Soft Matter*, *8*(40), 10439-10447.

[45] **Tong, H. M., Noda, I., & Gryte, C. C.** (1984). CPS 768 Formation of anisotropic ice-agar composites by directional freezing. *Colloid Polym. Sci.*, *262*(7), 589-595.

[46] **Yokoyama, F., Achife, E. C., Momoda, J., Shimamura, K., & Monobe, K.** (1990). Morphology of optically anisotropic agarose hydrogel prepared by directional freezing. *Colloid Polym. Sci.*, *268*(6), 552-558.

[47] **Meghri, N. W., Donius, A. E., Riblett, B. W., Martin, E. J., Clyne, A. M., & Wegst, U. G.** (2010). Directionally solidified biopolymer scaffolds: mechanical properties and endothelial cell responses. *Jom-J. Min. Met. Mat. S.*, *62*(7), 71-75.

[48] **Qi, X., Ye, J., & Wang, Y.** (2009). Alginate/poly (lactic-co-glycolic acid)/calcium phosphate cement scaffold with oriented pore structure for bone tissue engineering. *J. Biomed. Mater. Res. A.*, *89*(4), 980-987.

[49] **Francis, N. L., Hunger, P. M., Donius, A. E., Riblett, B. W., Zavaliangos, A., Wegst, U. G., & Wheatley, M. A.** (2013). An ice-templated, linearly aligned chitosan-alginate scaffold for neural tissue engineering. *J. Biomed. Mater. Res. A.*, *101*(12), 3493-3503.

[50] **Caliari, S. R., & Harley, B. A.** (2011). The effect of anisotropic collagen-GAG scaffolds and growth factor supplementation on tendon cell recruitment, alignment, and metabolic activity. *Biomaterials*, *32*(23), 5330-5340.

[51] **Wu, X., Liu, Y., Li, X., Wen, P., Zhang, Y., Long, Y., ... & Gao, J.** (2010). Preparation of aligned porous gelatin scaffolds by unidirectional freeze-drying method. *Acta Biomater.*, *6*(3), 1167-1177.

[52] **Guan, J., Porter, D., Tian, K., Shao, Z., & Chen, X.** (2010). Morphology and mechanical properties of soy protein scaffolds made by directional freezing. *J. Appl. Polym. Sci.*, *118*(3), 1658-1665.

[53] **Asuncion, M. C. T., Goh, J. C. H., & Toh, S. L.** (2016). Anisotropic silk fibroin/gelatin scaffolds from unidirectional freezing. *Mater. Sci. Eng. C.*, *67*, 646-656.

[54] **Zhang, Q., Zhao, Y., Yan, S., Yang, Y., Zhao, H., Li, M., ... & Kaplan, D. L.** (2012). Preparation of uniaxial multichannel silk fibroin scaffolds for guiding primary neurons. *Acta Biomater.*, *8*(7), 2628-2638.

[55] **Okay, O., & Lozinsky, V. I.** (2014). Synthesis and structure–property relationships of cryogels. *Adv. Polym. Sci.*, 103-157.

[56] **Lozinsky, V. I., & Okay, O.** (2014). Basic principles of cryotropic gelation. *Adv. Polym Sci.*, 49-101.

[57] **Dogu, S., & Okay, O.** (2008). Tough organogels based on polyisobutylene with aligned porous structures. *Polymer*, *49*(21), 4626-4634.

[58] **Chen, M., Zhu, J., Qi, G., He, C., & Wang, H.** (2012). Anisotropic hydrogels fabricated with directional freezing and radiation-induced polymerization and crosslinking method. *Mater. Lett.*, *89*, 104-107.

[59] **Wu, J., Zhao, Q., Sun, J., & Zhou, Q.** (2012). Preparation of poly (ethylene glycol) aligned porous cryogels using a unidirectional freezing technique. *Soft Matter*, *8*(13), 3620-3626.

[60] **Barrow, M., Eltmimi, A., Ahmed, A., Myers, P., & Zhang, H.** (2012). Frozen polymerization for aligned porous structures with enhanced mechanical stability, conductivity, and as stationary phase for HPLC. *J. Mater. Chem.*, *22*(23), 11615-11620.

[61] **Zhao, D., Zhu, J., Zhu, Z., Song, G., & Wang, H.** (2014). Anisotropic hierarchical porous hydrogels with unique water loss/absorption and mechanical properties. *RSC Adv.*, *4*(57), 30308-30314.

[62] **Arrua, R. D., & Hilder, E. F.** (2015). Highly ordered monolithic structures by directional freezing and UV-initiated cryopolymerisation. Evaluation as stationary phases in high performance liquid chromatography. *RSC Adv.*, *5*(87), 71131-71138.

[63] **Chau, M., De France, K. J., Kopera, B., Machado, V. R., Rosenfeldt, S., Reyes, L., ... & Kumacheva, E.** (2016). Composite hydrogels with tunable anisotropic morphologies and mechanical properties. *Chem. Mater.*, *28*(10), 3406-3415.

[64] **Vepari, C., & Kaplan, D. L.** (2007). Silk as a biomaterial. *Prog. Polym. Sci.*, *32*(8-9), 991-1007.
[65] **Vollrath, F., & Porter, D.** (2009). Silks as ancient models for modern polymers. *Polymer*, *50*(24), 5623-5632.
[66] **Hardy, J. G., Römer, L. M., & Scheibel, T. R.** (2008). Polymeric materials based on silk proteins. *Polymer*, *49*(20), 4309-4327.
[67] **Kim, U. J., Park, J., Li, C., Jin, H. J., Valluzzi, R., & Kaplan, D. L.** (2004). Structure and properties of silk hydrogels. *Biomacromolecules*, *5*(3), 786-792.
[68] **Matsumoto, A., Chen, J., Collette, A. L., Kim, U. J., Altman, G. H., Cebe, P., & Kaplan, D. L.** (2006). Mechanisms of silk fibroin sol− gel transitions. *J. Phys. Chem. B.*, *110*(43), 21630-21638.
[69] **Jin, H. J., & Kaplan, D. L.** (2003). Mechanism of silk processing in insects and spiders. *Nature*, *424*(6952), 1057-1061.
[70] **Dicko, C., Kenney, J. M., Knight, D., & Vollrath, F.** (2004). Transition to a β-sheet-rich structure in spidroin in vitro: the effects of pH and cations. *Biochemistry*, *43*(44), 14080-14087.
[71] **Karakutuk, I., Ak, F., & Okay, O.** (2012). Diepoxide-triggered conformational transition of silk fibroin: formation of hydrogels. *Biomacromolecules*, *13*(4), 1122-1128.
[72] **Yucel, T., Cebe, P., & Kaplan, D. L.** (2009). Vortex-induced injectable silk fibroin hydrogels. *Biophys. J.*, *97*(7), 2044-2050.
[73] **Servoli, E., Maniglio, D., Motta, A., & Migliaresi, C.** (2008). Folding and assembly of fibroin driven by an AC electric field: effects on film properties. *Macromol. Biosci.*, *8*(9), 827-835.
[74] **Chen, X., Knight, D. P., Shao, Z., & Vollrath, F.** (2002). Conformation transition in silk protein films monitored by time-resolved Fourier transform infrared spectroscopy: effect of potassium ions on Nephila spidroin films. *Biochemistry*, *41*(50), 14944-14950.
[75] **Mo, C., Holland, C., Porter, D., Shao, Z., & Vollrath, F.** (2009). Concentration state dependence of the rheological and structural properties of reconstituted silk. *Biomacromolecules*, *10*(10), 2724-2728.
[76] **Argun, A., Can, V., Altun, U., & Okay, O.** (2014). Nonionic double and triple network hydrogels of high mechanical strength. *Macromolecules*, *47*(18), 6430-6440.
[77] **Hu, X., Kaplan, D., & Cebe, P.** (2007). Effect of water on the thermal properties of silk fibroin. *Thermochim. Acta.*, *461*(1-2), 137-144.
[78] **Ak, F., Oztoprak, Z., Karakutuk, I., & Okay, O.** (2013). Macroporous silk fibroin cryogels. *Biomacromolecules*, *14*(3), 719-727.
[79] **Okay, O.** (2000). Macroporous copolymer networks. *Prog. Polym. Sci.*, *25*(6), 711-779.
[80] **Park, S. J., Lee, K. Y., Ha, W. S., & Park, S. Y.** (1999). Structural changes and their effect on mechanical properties of silk fibroin/chitosan blends. *J. Appl. Polym. Sci.*, *74*(11), 2571-2575.
[81] **Butler, M. F.** (2001). Instability formation and directional dendritic growth of ice studied by optical interferometry. *Cryst. Growth Des.*, *1*(3), 213-223.
[82] **Calvert, P.** (2009). Hydrogels for soft machines. *Adv. Mater.*, *21*(7), 743-756.
[83] **Sano, K., Ishida, Y., & Aida, T.** (2018). Synthesis of anisotropic hydrogels and their applications. *Angew. Chem. Int. Edit.*, *57*(10), 2532-2543.

[84] **Elliott, D. M., & Setton, L. A.** (2001). Anisotropic and inhomogeneous tensile behavior of the human anulus fibrosus: experimental measurement and material model predictions. *J. Biomech. Eng.*, *123*(3), 256-263.

[85] **Argun, A., Gulyuz, U., & Okay, O.** (2018). Interfacing soft and hard materials with triple-shape-memory and self-healing functions. *Macromolecules*, *51*(7), 2437-2446.

[86] **Keisuke, K., Keisuke, U., Hiroyasu, M., Yoichi, T., Kiyotaka, S., & Shikinaka, K. S. K.** (2014). Flow-orientation of internal structure and anisotropic properties on hydrogels consisted of imogolite hollow nanofibers. *Sen-i Gakkaishi*, *70*(7), 137-144.

[87] **Tanaka, Y., Kubota, A., Matsusaki, M., Duncan, T., Hatakeyama, Y., Fukuyama, K., ... & Nishida, K.** (2011). Anisotropic mechanical properties of collagen hydrogels induced by uniaxial-flow for ocular applications. *J. Biomat. Sci. Polym. E.*, *22*(11), 1427-1442.

[88] **Paz, A. C., Soleas, J., Poon, J. C., Trieu, D., Waddell, T. K., & McGuigan, A. P.** (2014). Challenges and opportunities for tissue-engineering polarized epithelium. *Tissue Eng. Part B-Reviews.*, *20*(1), 56-72.

[89] **Oliveira, A. L., Sun, L., Kim, H. J., Hu, X., Rice, W., Kluge, J., ... & Kaplan, D. L.** (2012). Aligned silk-based 3-D architectures for contact guidance in tissue engineering. *Acta Biomater.*, *8*(4), 1530-1542.

[90] **Yetiskin, B., & Okay, O.** (2017). High-strength silk fibroin scaffolds with anisotropic mechanical properties. *Polymer*, *112*, 61-70.

[91] **Yetiskin, B., Akinci, C., & Okay, O.** (2017). Cryogelation within cryogels: Silk fibroin scaffolds with single-, double-and triple-network structures. *Polymer*, *128*, 47-56.

[92] **Nisal, A., Sayyad, R., Dhavale, P., Khude, B., Deshpande, R., Mapare, V., ... & Venugopalan, P.** (2018). Silk fibroin micro-particle scaffolds with superior compression modulus and slow bioresorption for effective bone regeneration. *Sci. Rep.*, *8*(1), 1-10.

[93] **Li, B., & Aspden, R. M.** (1997). Composition and mechanical properties of cancellous bone from the femoral head of patients with osteoporosis or osteoarthritis. *J. Bone Miner. Res.*, *12*(4), 641-651.

[94] **Kong, X., & Qiao, Y.** (2005). Improvement of recoverability of a nanoporous energy absorption system by using chemical admixture. *Appl. Phys. Lett.*, *86*(15), 151919.

[95] **Persson, B. N.** (2013). *Sliding friction: physical principles and applications*. Springer Science & Business Media.

[96] **Gong, J. P., Kurokawa, T., Narita, T., Kagata, G., Osada, Y., Nishimura, G., & Kinjo, M.** (2001). Synthesis of hydrogels with extremely low surface friction. *J. Am. Chem. Soc.*, *123*(23), 5582-5583.

[97] EU Technical Guidance Document 19. Common Implementation Strategy for the Water Framework Directive (2000/60/EC). Guidance on Surface Water Chemical Monitoring under the Water Framework Directive. Technical Report, 2009; Vol. 025, pp 10−37.

[98] EU-Directive 2013/39/EU of the European Parliament and of the Council Amending Directives 2000/60/EC and 2008/105/EC as Regards Priority Substances in the Field of Water Policy. Off. J. Eur. Union 2013, L226, 1−17.

[99] **Gonzalez-Rey, M., Tapie, N., Le Menach, K., Dévier, M. H., Budzinski, H., & Bebianno, M. J.** (2015). Occurrence of pharmaceutical compounds and pesticides in aquatic systems. *Mar. Pollut. Bull.*, *96*(1-2), 384-400.

[100] **Miège, C., Mazzella, N., Allan, I., Dulio, V., Smedes, F., Tixier, C., ... & Vrana, B.** (2015). Position paper on passive sampling techniques for the monitoring of contaminants in the aquatic environment–achievements to date and perspectives. *Trends Environ. Anal. Chem.*, *8*, 20-26.

[101] **Poulier, G., Lissalde, S., Charriau, A., Buzier, R., Delmas, F., Gery, K., ... & Mazzella, N.** (2014). Can POCIS be used in Water Framework Directive (2000/60/EC) monitoring networks? A study focusing on pesticides in a French agricultural watershed. *Sci. Total Environ.*, *497*, 282-292.

[102] **Vrana, B., Allan, I. J., Greenwood, R., Mills, G. A., Dominiak, E., Svensson, K., ... & Morrison, G**. (2005). Passive sampling techniques for monitoring pollutants in water. *TrAC-Trend Anal. Chem.*, *24*(10), 845-868.

[103] **Huckins, J. N., Petty, J. D., & Booij, K.** (2006). *Monitors of organic chemicals in the environment: semipermeable membrane devices*. Springer Science & Business Media.

[104] **Rusina, T. P., Smedes, F., Klanova, J., Booij, K., & Holoubek, I.** (2007). Polymer selection for passive sampling: A comparison of critical properties. *Chemosphere*, *68*(7), 1344-1351.

[105] **Mattiasson, B., Kumar, A., Galeaev, I. Y.,** (2010). Macroporous Polymers: Production Properties and Biotechnological/Biomedical Applications; CRC Press; pp 1−513.

[106] **Han, J., Du, G., Gao, W., & Bai, H.** (2019). An anisotropically high thermal conductive boron nitride/epoxy composite based on nacre-mimetic 3D network. *Adv. Funct. Mater.*, *29*(13), 1900412.

[107] **Chen, D., Zhang, Y., Ni, C., Ma, C., Yin, J., Bai, H., ... & Zhao, Q.** (2019). Drilling by light: ice-templated photo-patterning enabled by a dynamically crosslinked hydrogel. *Mater. Horiz.*, *6*(5), 1013-1019.

[108] **Leonhardt, E. E., Kang, N., Hamad, M. A., Wooley, K. L., & Elsabahy, M.** (2019). Absorbable hemostatic hydrogels comprising composites of sacrificial templates and honeycomb-like nanofibrous mats of chitosan. *Nat. Commun.*, *10*(1), 1-9.

[109] **Lozinsky, V. I.** (2002). Cryogels on the basis of natural and synthetic polymers: preparation, properties and application. *Russ. Chem. Rev.*, *71*(6), 489-511.

[110] **Yang, M., Wu, J., Bai, H., Xie, T., Zhao, Q., & Wong, T. W.** (2016). Controlling three-dimensional ice template via two-dimensional surface wetting. *AIChE J.*, *62*(12), 4186-4192.

[111] **Lozinsky, V. I., Vainerman, E. S., Titova, E. F., Belavtseva, E. M., & Rogozhin, S. V.** (1984). Study of cryostructurization of polymer systems. *Colloid Polym. Sci.*, *262*(10), 769-774.

[112] **Ozmen, M. M., Fu, Q., Kim, J., & Qiao, G. G.** (2015). A rapid and facile preparation of novel macroporous silicone-based cryogels via photo-induced thiol–ene click chemistry. *Chem. Commun.*, *51*(98), 17479-17482.

[113] **Wong, T. W., Wu, J., Yang, M., Kadir, M. R. A., Wahit, M. U., & Zhao, Q.** (2017). Multifunctional shape-memory foams with highly tunable properties via organo-phase cryo-polymerization. *J. Mater. Chem. A.*, *5*(20), 9793-9800.

[114] **Akiba, M. A., & Hashim, A. S.** (1997). Vulcanization and crosslinking in elastomers. *Prog. Polym. Sci.*, *22*(3), 475-521.

[115] **Ceylan, D.; Okay, O.** Macroporous Polyisobutylene Gels: A Novel Tough Organogel with Superfast Responsivity. *Macromolecules*, 2007, 40, 8742−8749.

[116] **Okay, O., Durmaz, S., & Erman, B.** (2000). Solution cross-linked poly (isobutylene) gels: Synthesis and swelling behavior. *Macromolecules*, *33*(13), 4822-4827.

[117] **Hu, Y., Liu, X., Zou, J., Gu, T., Chai, W., & Li, H.** (2013). Graphite/isobutylene-isoprene rubber highly porous cryogels as new sorbents for oil spills and organic liquids. *ACS Appl. Mater. Inter.*, *5*(16), 7737-7742.

[118] **Ceylan, D., Dogu, S., Karacik, B., Yakan, S. D., Okay, O. S., & Okay, O.** (2009). Evaluation of butyl rubber as sorbent material for the removal of oil and polycyclic aromatic hydrocarbons from seawater. *Environ. Sci. Technol.*, *43*(10), 3846-3852.

[119] **Karakutuk, I., & Okay, O.** (2010). Macroporous rubber gels as reusable sorbents for the removal of oil from surface waters. *React. Funct. Polym.*, *70*(9), 585-595.

[120] **Su, E., & Okay, O.** (2019). Cryogenic formation-structure-property relationships of poly (2-acrylamido-2-methyl-1-propanesulfonic acid) cryogels. *Polymer*, *178*, 121603.

[121] **Tuncaboylu, D. C., Sahin, M., Argun, A., Oppermann, W., & Okay, O.** (2012). Dynamics and large strain behavior of self-healing hydrogels with and without surfactants. *Macromolecules*, *45*(4), 1991-2000.

[122] **Tütem, E., Apak, R., & Ünal, Ç. F.** (1998). Adsorptive removal of chlorophenols from water by bituminous shale. *Water Res.*, *32*(8), 2315-2324.

[123] **Sarkar, M., Acharya, P. K., & Bhattacharya, B.** (2003). Modeling the adsorption kinetics of some priority organic pollutants in water from diffusion and activation energy parameters. *J. Colloid Interf. Sci.*, *266*(1), 28-32.

[124] **Hill, A. V.** (1913). The combinations of haemoglobin with oxygen and with carbon monoxide. I. *Biochem. J.*, *7*(5), 471.

[125] **Adibnia, V., & Hill, R. J.** (2016). Universal aspects of hydrogel gelation kinetics, percolation and viscoelasticity from PA-hydrogel rheology. *J. Rheol.*, *60*(4), 541-548.

[126] **Calvet, D., Wong, J. Y., & Giasson, S.** (2004). Rheological monitoring of polyacrylamide gelation: Importance of cross-link density and temperature. *Macromolecules*, *37*(20), 7762-7771.

[127] **Giraldo, J., Vivas, N. M., Vila, E., & Badia, A.** (2002). Assessing the (a) symmetry of concentration-effect curves: empirical versus mechanistic models. *Pharmacol. Therapeut.*, *95*(1), 21-45.

[128] **Tavsanli, B., & Okay, O.** (2019). Mechanically robust and stretchable silk/hyaluronic acid hydrogels. *Carbohyd. Polym.*, *208*, 413-420.

[129] **Barton, A. F. M.** (1983). Handbook of Solubility Parameters and Other Cohesion Parameters CRC Press. *Inc., Boca Raton, FL*.

**CURRICULUM VITAE**

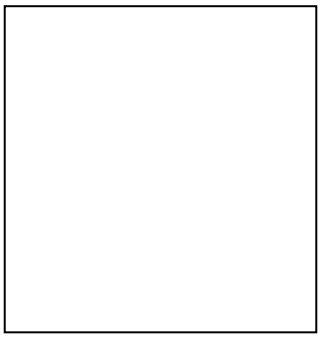

**Name Surname** **:** Berkant YETİŞKİN

**EDUCATION** **:**

- **B.Sc.** **:** 2013, Çanakkale Onsekiz Mart University, Faculty of Arts and Sciences, Department of Chemistry
- **M.Sc.** **:** 2016, Istanbul Technical University, Graduate School of Science, Engineering and Technology, Chemistry Programme
- **Ph.D.** **:** 2021, Istanbul Technical University, Graduate School, Chemistry Programme

**PROFESSIONAL EXPERIENCE:**

- Research Project Asistant as MSc and PhD Fellow in TUBITAK Projects (No. 114Z312, 117Y099, 218M502)

**PUBLICATIONS, PRESENTATIONS AND PATENTS ON THE THESIS:**

- **Yetiskin, B.,** Tureyen, O. E., Yilmaz, A., Yakan, S. D., Okay, O. S., & Okay, O. (2021). Fabrication of Rubber Based Sorbents with Adjustable Pore Morphology via Cryogenic Vulcanization and Their Usage in Sampling of Organic Pollutants from Water Medium. 33th National Chemistry Congress. 7-9 October 2021, Online.
- **Yetiskin, B.,** Tureyen, O. E., Yilmaz, A., Yakan, S. D., Okay, O. S., & Okay, O. (2019). Single-, double-, and triple-network macroporous rubbers as a passive sampler. *ACS Appl. Mater. Inter.*, *11*(31), 28317-28326.
- **Yetiskin, B.,** & Okay, O. (2019). High-strength and self-recoverable silk fibroin cryogels with anisotropic swelling and mechanical properties. *Int. J. Biol. Macromol.*, *122*, 1279-1289.
- **Yetiskin, B.,** & Okay, O. (2017). High-strength silk fibroin scaffolds with anisotropic mechanical properties. *Polymer*, *112*, 61-70.
- **Yetiskin B.,** & Okay O., (2019). Anisotropic Silk Fibroin Tissue Scaffolds with Flow-Dependent Viscoelasticity. 24th International Biomedical Science and Technology Symposium. 17-20 October 2019, Cesme/Turkey.

- **Yetiskin B.,** & Okay O., (2017). Silk Fibroin Scaffolds with Anisotropic Mechanical Properties. 3rd International Porous and Powder Materials Symposium and Exhibition. 12-15 September 2017, Kusadasi/Turkey.

**OTHER PUBLICATIONS, PRESENTATIONS AND PATENTS:**

- Tureyen, O. E., Yilmaz, A., Yakan, S. D., **Yetiskin, B.,** Okay, O., & Okay, O. S. (2021). Performance of butyl rubber–based macroporous sorbents as passive samplers. *Environ. Sci. Pollut. R.*, *28*(4), 3766-3773.
- Oral, C. B., **Yetiskin, B.,** & Okay, O. (2020). Stretchable silk fibroin hydrogels. *Int. J. Biol. Macromol*, *161*, 1371-1380.
- Ari, B., **Yetiskin, B.,** Okay, O., & Sahiner, N. (2020). Preparation of dextran cryogels for separation processes of binary dye and pesticide mixtures from aqueous solutions. *Polym. Eng. Sci.*, *60*(8), 1890-1901.
- Akca, O., **Yetiskin, B.,** & Okay, O. (2020). Hydrophobically modified nanocomposite hydrogels with self-healing ability. *J. Appl. Polym. Sci.*, *137*(28), 48853.
- Suner, S. S., Demirci, S., **Yetiskin, B.,** Fakhrullin, R., Naumenko, E., Okay, O., ... & Sahiner, N. (2019). Cryogel composites based on hyaluronic acid and halloysite nanotubes as scaffold for tissue engineering. *Int. J. Biol. Macromol*, *130*, 627-635.
- Muslumova, S., **Yetiskin, B.,** & Okay, O. (2019). Highly Stretchable and Rapid Self-Recoverable Cryogels Based on Butyl Rubber as Reusable Sorbent. *Gels*, *5*(1), 1.
- **Yetiskin, B.,** Akinci, C., & Okay, O. (2017). Cryogelation within cryogels: Silk fibroin scaffolds with single-, double-and triple-network structures. *Polymer*, *128*, 47-56.
- **Yetiskin B.,** & Okay O., (2015). Mechanically Durable Silk Fibroin Cryogels. 27th National Chemistry Congress. 23-28 August 2015, Canakkale/Turkey.
- **Yetiskin B.,** & Okay O., (2015). Macroporous Double-Network Silk Fibroin Cryogels. International Biomedical Engineering Congress. 12-14 March 2015, Nicosia/North Cyprus.